

**UNIVERSITY OF NOTTINGHAM NINGBO CHINA  
DEPARTMENT OF MECHANICAL, MATERIALS AND  
MANUFACTURING ENGINEERING**

**Investigation on the Isolation and Detection of  
Circulating Tumor Cells Based on  
Microfluidics and Surface-Enhanced Raman Scattering Method**

**Xiawei Xu**

**16 November 2022**

A thesis submitted for the Degree of Doctor of Engineering in Mechanical,  
Materials and Manufacturing Engineering at the University of Nottingham,  
2022.

## **Abstract**

Cancer is a leading cause of death and is an important barrier to increase life expectancy in every country of the world. Besides, two thirds of cancer death occurred in less developed countries because of delayed diagnosis and less accessible treatment. The delayed diagnosis would lead to increased death and disability from cancer. Therefore, it is essential to develop a technology for cancer detection with universality and less cost. The common imaging technologies, such as Magnetic Resonance Imaging (MRI), Computed Tomography (CT) and Positron Emission Tomography (PET), can be used for cancer early screening. After early screening, people who have symptoms and signs consistent with cancer, require further identification of cancer by pathological diagnoses. The traditional invasive biopsy would cause psychological burden to patients and is limited by sample collection in deep tumor and sampling bias. It also has risk of tumor metastasis. In recent decades, liquid biopsy technique has developed quickly and attracted more and more attention. Compared to invasive biopsy, liquid biopsy is noninvasive, cheaper, simple for sample collection with minimum risk. The sensitivity and specificity of liquid biopsy technique has also been improved remarkably due to the continuous innovation in molecular biology technology. Liquid biopsy generally includes the detection of circulating tumor cells (CTCs), circulating tumor-derived exosomes and circulating tumor nucleic acids. Circulating tumor cells are tumor cells that shed from solid tumor and circulate in the blood. Circulating tumor-derived exosomes are vesicles that secret from tumor cells containing some ribonucleic acids (RNA) and protein. Circulating tumor nucleic acids are nucleic acids shedding from tumor cells or released by apoptotic cells. Compared to circulating tumor-derived exosomes and circulating tumor nucleic acids, circulating tumor cells are integrated cells carrying more complete information about tumor. Circulating tumor cell (CTC) detection as a burgeoning detection strategy can identify the tumor lesion in the

early stage, and facilitate the understanding of tumorigenesis, tumor progression, metastasis, and drug-resistance. As so far, many technologies for CTC detection have been developed. Generally, CTC detection can be divided into two stages: first is isolation and enrichment of CTCs and second is downstream analysis of CTCs. There are three main challenges existing in CTC detection: small number of CTCs, complex blood background, and diversified typing of CTCs. To overcome these difficulties, microfluidic method has been applied to improve CTC isolation combined with Raman fingerprint spectra and surface-enhanced Raman scattering (SERS) method to distinguish CTCs from other blood components. Current microfluidic method cannot separate CTCs completely from blood, which requires further downstream analysis to distinguish CTCs from remaining blood cells. Besides, SERS method might be interfered by complex blood components, which would reduce detection sensitivity of SERS method. Therefore, blood samples require pretreatment to reduce the interference of blood cells for SERS detection and improve repeatability and reliability of detection results. In this thesis, SPION-PEI@Au based SERS biological probe and B-TiO<sub>2</sub> based SERS biological probe were prepared for direct detection of CTCs in the blood. To improve the detection sensitivity and accuracy, microfluidic method was combined for blood pretreatment before SERS detection. The specific research contents mainly include the following three parts:

1. Superparamagnetic iron oxide nanoparticles with poly(ethyleneimine) coated with gold nanoparticles (SPION-PEI@Au) were synthesized according to the previous work of the research group. In this work, SPION-PEI@Au based SERS biological probe was applied on CTC detection of clinical blood samples. The SPION@Au-MBA-rBSA-FA SERS biological probe consisted of four parts: SPION-PEI@Au composite nanoparticles as SERS substrate, 4-mercaptobenzoic acid (MBA) as Raman reporter, reduced bovine serum albumin and folic acid (rBSA-FA) to recognize

folate receptor (FR) on cancer cell membrane. In this work, 32 clinical blood samples from cancer tumor and 3 clinical blood samples from healthy people were detected directly by SPION@Au-MBA-rBSA-FA SERS biological probe.

2. Black TiO<sub>2</sub> (B-TiO<sub>2</sub>) nanoparticles were used as SERS substrate. B-TiO<sub>2</sub> has advantages of low cost, high spectral stability and reproducibility, strong anti-interference ability, and selective SERS enhancement to target molecules. The synthesized B-TiO<sub>2</sub> showed good SERS enhancement effect and the LOD of the AR molecule on B-TiO<sub>2</sub> can reach to  $5 \times 10^{-8}$  M. The B-TiO<sub>2</sub>-AR-PEG-FA biological probe consisted of four layers. The innermost layer was B-TiO<sub>2</sub> nanoparticles with crystal core and amorphous shell structure. The second layer was alizarin red (AR) molecule which was responsible for providing Raman spectral signal. The third layer was a thin NH<sub>2</sub>-PEG2000-COOH layer which was used to improve the dispersion of biological probe and to provide binding sites of folic acid (FA) and thus to increase FA grafting rate. The outermost layer was FA molecule. FA was used to specifically recognize cancer cells by folate receptor (FR) on cancer cell membrane. The research results showed that this B-TiO<sub>2</sub> based SRES biological probe has good specificity and detection accuracy with obvious Raman signal. It can distinguish positive FR-expressing cancer cells (MCF-7) from lower FR-expressing cells (A549 and Raw264.7).
3. Because of complex blood components, the sensitivity and stability of SERS biological probe would be attenuated without proper blood pretreatment. To improve the performance of SERS biological probe, microfluidic method was added to isolate CTCs before SERS detection. In this strategy, the relatively low specificity and isolation purity of microfilter could be solved by integrating with highly sensitive and highly specific SERS spectra detection, while the microfilter could reduce the interference

of blood background to SERS detection. Besides, SERS-fluorescence dual-modal in situ imaging method proved that this strategy has high specificity with detection limit of 2 cancer cells per milliliter in rabbit blood. Besides, the operation process was simple and high-speed, with detection time less than 1.5 hours. This strategy has also been applied to CTC detection of clinical blood samples and has detected CTCs from blood successfully.

These results illustrated that in addition to noble metal nanoparticles, semiconductor nanoparticles can also be used for SERS detection with good SERS enhancement effect. Although SERS method has good sensitivity in CTC detection, the performance of SERS method would be affected by complex components of blood and improper blood treatment. Microfluidic method was combined to remove the interference of blood cells and to improve the repeatability and reliability of SERS detection. The combination of microfluidic method and SERS detection method could complement their own shortcomings and thus to improve the detection efficiency. This thesis demonstrated that the combination of microfluidic method and SERS detection method could open new paths for liquid biopsy.

|  |              |
|--|--------------|
| <b>Table of Contents</b>                                     |              |
| <b>Abstract</b>  | <b>i</b>     |
| <b>Table of Contents</b>                                     | <b>vi</b>    |
| <b>Acknowledgment</b>  | <b>ix</b>    |
| <b>List of Publications</b>                                  | <b>xi</b>    |
| <b>List of Figures</b>                                       | <b>xiv</b>   |
| <b>List of Tables</b>  | <b>xvii</b>  |
| <b>List of Abbreviations</b>                                 | <b>xviii</b> |
| <b>Chapter 1 Introduction</b>                                | <b>1</b>     |
| 1.1 Circulating tumor cells                                  | 3            |
| 1.2.1 Biological properties of CTCs                          | 4            |
| 1.2.2 Physical properties of CTCs                            | 6            |
| 1.3 Clinical application of CTCs                             | 10           |
| 1.3.1 CTCs and early diagnosis                               | 11           |
| 1.3.2 CTCs and prognosis evaluation                          | 12           |
| 1.3.3 CTCs and therapeutic efficacy                          | 12           |
| 1.4 CTC detection: isolation and downstream analysis of CTCs | 13           |
| 1.4.1 Isolation technology of CTCs                           | 14           |
| 1.4.2 Downstream analysis of CTCs                            | 15           |
| 1.5 Microfluidics for CTC detection                          | 17           |
| 1.5.1 Label-dependent technologies                           | 17           |
| 1.5.2 Label-independent technologies                         | 22           |
| 1.5.3 Multistep technologies for CTC isolation               | 28           |
| 1.6 SERS detection method                                    | 31           |
| 1.6.1 Metal-based SERS detection method                      | 32           |

|   |           |
|---|-----------|
| 1.6.2 Semiconductor-based SERS detection method   | 34        |
| 1.6.3 Application of SERS detection method in biosensing  | 35        |
| 1.7 Gold-iron oxide composite nanoparticles   | 40        |
| 1.7.1 Structure and synthesis of gold-iron oxide composite nanoparticles                          | 41        |
| 1.7.2 Applications of gold-iron oxide composite nanoparticles in cell sorting and separation      | 43        |
| 1.8 Black titanium dioxide  | 46        |
| 1.9 Research gap  | 48        |
| 1.10 Outline of the thesis  | 49        |
| <b>Chapter 2 Methodologies</b>  | <b>53</b> |
| 2.1 Introduction  | 53        |
| 2.2 Synthesis of SPION-PEI@AuNPs-based SERS biological probe and application on CTC detection     | 54        |
| 2.2.1 Materials and equipment   | 54        |
| 2.2.2 Synthesis of SPION-PEI@AuNPs-based SERS biological probe                                    | 55        |
| 2.2.3 Cell culture  | 58        |
| 2.2.4 Specificity of SPION-PEI@AuNPs-based SERS biological probe in Cells                         | 58        |
| 2.2.5 Sensitivity and separation of SPION-PEI@AuNPs-Based SERS biological probe in blood          | 59        |
| 2.2.6 Application in clinical tumor blood detection   | 60        |
| 2.3 Synthesis of B-TiO <sub>2</sub> -based SERS biological probe and application on CTC detection | 61        |
| 2.3.1 Materials and equipment   | 61        |
| 2.3.2 Synthesis of B-TiO <sub>2</sub> -based SERS biological probe                                | 62        |
| 2.3.3 Cell culture  | 64        |

|   |           |
|---|-----------|
| 2.3.4 FR expression screening of MCF-7, A549 and Raw264.7 cell lines  | 64        |
| 2.3.5 FA modification of SERS biological probe  | 65        |
| 2.3.6 Specificity and sensitivity of B-TiO <sub>2</sub> -based SERS biological probe in the mixed cells                 | 65        |
| 2.4 Combination method of microfilter and B-TiO <sub>2</sub> -based SERS biological probe on CTC detection              | 67        |
| 2.4.1 Materials and equipment   | 67        |
| 2.4.2 Cell culture  | 68        |
| 2.4.3 Simulation of optimum capture flow rate in microfilter  | 68        |
| 2.4.4 Sensitivity, specificity, and capture assay of microfilter combined SERS spectral detection method in mixed cells | 73        |
| 2.4.5 Sensitivity, specificity, and capture assay of microfilter combined SERS spectral detection method in blood       | 74        |
| 2.4.6 Application in clinical tumor blood detection   | 75        |
| 2.5 Conclusion  | 75        |
| <b>Chapter 3 Synthesis of SPION-PEI@AuNPs-based SERS biological probe and application on CTC detection</b>              | <b>77</b> |
| 3.1 Introduction  | 77        |
| 3.2 Characterization of SPION-PEI@AuNPs-based SERS biological probe   | 79        |
| 3.3 Specificity of SPION-PEI@AuNPs-based SERS biological probe in cells   | 83        |
| 3.4 Sensitivity and separation of SPION-PEI@AuNPs-based SERS biological probe in blood                                  | 85        |
| 3.5 Application of SPION-PEI@AuNPs-based SERS biological probe in the clinical blood samples                            | 86        |

|   |            |
|---|------------|
| 3.6 Chapter conclusion  | 89         |
| <b>Chapter 4 Synthesis of B-TiO<sub>2</sub>-based SERS biological probe and application on CTC detection</b>          | <b>90</b>  |
| 4.1 Introduction  | 90         |
| 4.2 Characterization of B-TiO <sub>2</sub> -Based SERS biological probe   | 91         |
| 4.3 FR expression screening of MCF-7, A549 and Raw264.7 cell lines  | 99         |
| 4.4 Specificity and stability of B-TiO <sub>2</sub> -based SERS biological probe in the mixed cells                   | 100        |
| 4.5 Chapter conclusion  | 105        |
| <b>Chapter 5 Combination method of microfilter and B-TiO<sub>2</sub>-based SERS biological probe on CTC detection</b> | <b>107</b> |
| 5.1 Introduction  | 107        |
| 5.2 Simulation of optimum capture flow rate in microfilter  | 109        |
| 5.3 Sensitivity, specificity, and capture assay of microfilter combined SERS spectral detection method in blood       | 113        |
| 5.4 Application in clinical tumor blood detection   | 115        |
| 5.5 Chapter conclusion  | 118        |
| <b>Chapter 6 Conclusion and future perspective</b>  | <b>120</b> |
| 6.1 Conclusion  | 120        |
| 6.2 Future perspective  | 121        |
| <b>References</b>   | <b>126</b> |
| <b>Appendix</b>   | <b>141</b> |

## **Acknowledgement**

First, I would like to thank my parents. They always support my decisions unconditionally. They never evaluate me with worldly eyes. They are the most enlightened parents.

This thesis was finished under the guidance of Prof. Aiguo Wu, Associate Prof. Yong Ren, and Dr Jie Lin. It is my great honor to become a joint postgraduate of Ningbo Nottingham University/Ningbo Institute of Materials Technology and Engineering, Chinese Academy of Sciences, to carry out research projects in Ningbo Institute of Materials and Cixi Institute of BioMedical Engineering, and to complete the doctoral dissertation. During 4 years of PhD program studying, I have grown a lot. At the beginning, I applied PhD program from Associate Prof. Yong Ren. He introduced me to Prof. Aiguo Wu. Although my master's degree is intelligent building technology and management, which is highly different from current major, Prof. Aiguo Wu accepted me with great tolerance. I really appreciate they could give me a choice to develop a new project in the field of mechanical engineering and bio-nanomaterials. When I have problems in research, they guided me to solve problems and encouraged me to keep going. Prof. Aiguo Wu often shared literatures to me and provides novel ideas to me. His serious and rigorous working attitude also inspired me a lot. Associate Prof. Yong Ren often provided me with technical support and training. He respects students and would discuss with students with their new ideas. Dr Jie Lin is like a senior brother. He often checked up my experiment progress and proved thoughts and methods to solve my experimental problems. In addition to research, they were also very concerned about my life. They often reminded me to have a rest and keep health. With their care, I could carry out my work smoothly.

Next, I would like to appreciate the students and the teachers in our research

group and in experiment test platform. Although Meng He and Yanpin Xu were my junior sister, they taught me a lot with the use of experimental equipment and pulled me to finish experiment. Teacher Wenzhi Ren made a lot of efforts to ensure the safety of the experiment. There were other students and teachers who help me a lot. Without their help, my work could not be carried smoothly.

I also want to thank my friend Rui Hu. He is always by my side witnessing my happiness and sadness.

Finally, I would like to express my heartfelt thanks to my classmates, friends, teachers, and relatives who have given me care and help in life and study. Thank them for giving me the confidence and strength to make progress.

## List of publication

1. **Xu Xiawei**, Lin Jin\*, Guo Yanhong, Wu Xiaoxia, Zhang Xiangzhi, Xu Yanping, Zhang Dinghu, Xie Yujiao, Wang Jing, Yao Chengyang, Yao Junlie, Xing Jie, Cao Yi, Li Yanying, Ren Wenzhi, Chen Tianxiang, Ren Yong \*, Wu Aiguo \*. An efficient circulating tumor cell detection strategy via high capture efficiency in microfilter and superior SERS sensitivity of black TiO<sub>2</sub> nanoparticles. *Biosensors and Bioelectronics* **2022**, 210, 114305.
2. **Xu Xiawei**, Jiang Zhenqi, Wang Jing, Ren Yong\*, Wu Aiguo\*. Microfluidic applications on circulating tumor cell isolation and biomimicking of cancer metastasis. *Electrophoresis* **2020**, 41, 933-951.
3. Zhang Xiangzhi<sup>#</sup>, **Xu Xiawei**<sup>#</sup>, Ren Yong\*, Yan Yuying\*, Wu Aiguo\*. Numerical simulation of circulating tumor cell separation in dielectrophoresis based Y-Y shaped microfluidic device. *Separation and Purification Technology* **2021**, 255, 1383-5866.
4. Zhang Xiangzhi<sup>#</sup>, **Xu Xiawei**<sup>#</sup>, Wang Jing, Wang Chengbo, Yan Yuying\*, Wu Aiguo\*, Ren Yong\*. Public-Health-Driven Microfluidic Technologies: From Separation to Detection. *Micromachines* **2021**, 12, 391.
5. He Meng, Lin Jin\*, Akakuru Ozioma, **Xu Xiawei**, Li Yanying, Cao Yi, Xu Yanping, Wu Aiguo\*. Octahedral silver oxide nanoparticles enabling remarkable SERS activity for detecting circulating tumor cells. *Science China-Life Sciences* **2021**, 65, 561-571.
6. Yao Junlie, Zheng Fang, Yao Chenyang, **Xu Xiawei**, Akakuru Ozioma, Chen, Tianxiang, Yang Fang\*, Wu Aiguo\*. Rational design of nanomedicine for photothermal-chemodynamic bimodal cancer therapy. *Wiley Interdisciplinary Reviews: Nanomedicine and Nanobiotechnology* **2021**, 13, e1682.
7. Xu Yanping, Lin Jie, Wu Xiaoxia, **Xu Xiawei**, Zhang Dinghu, Xie Yujiao, Pan Ting, He Yiwei, Wu Aiguo\*, Shao Guoliang\*. TiO<sub>2</sub>-Based Bioprobe

- Enabling Excellent SERS Activity in Detection of Diverse Circulating Tumor Cells. *Journal of Materials Chemistry B*. **2022**, 10, 3808-3816.
8. Zhang Yuenan, Zhang Yujie\*, Akakuru Ozioma, **Xu Xiawei**, Wu Aiguo\*. Research progress and mechanism of nanomaterials-mediated in-situ remediation of cadmium-contaminated soil: A critical review. *Journal of Environmental Sciences* **2021**, 104, 351-364.
  9. Yao Junlie, Peng Hao, Qiu Yue, Li Shunxiang, **Xu Xiawei**, Wu Aiguo\*, Yang Fang\*. Nanoplatfrom-mediated calcium overload for cancer therapy. *Journal of Materials Chemistry B*. **2022**, 10, 1508-1519.
  10. Xu Yanping, Zhang Dinghu, Lin Jie, Wu Xiaoxia, **Xu Xiawei**, Akakuru Ozioma, Zhang Hao, Zhang Zhewei, Xie Yujiao, Wu Aiguo\*, Shao Guoliang\*. Ultrahigh SERS Activity of TiO<sub>2</sub>@Ag Nanostructure leveraged for Accurately Detecting CTCs in peripheral blood. *Biomaterials Science* **2022**, 10, 1812-1820.
  11. Yao Junlie, Yang Fang\*, Zheng Fang, Yao Chenyang, Xing Jie, **Xu Xiawei**, Wu Aiguo\*. Boosting Chemodynamic Therapy via a Synergy of Hypothermal Ablation and Oxidation Resistance Reduction. *ACS Applied Materials & Interfaces* **2021**, 13, 54770-54782.
  12. Yao Junlie, Zheng Fang, Yang Fang\*, Yao Chenyang, Xing Jie, Li Zihou, Sun Sijia, Chen Jia, **Xu Xiawei**, Cao Yi, Hampp Norbert, Wu Aiguo\*. Intelligent tumor microenvironment responsive nanotheranostic agent for T<sub>1</sub>/T<sub>2</sub> dual-modal magnetic resonance imaging-guided and self-augmented photothermal therapy. *Biomaterials Science* **2021**, 9, 7591-7602.

## Patents

1. Jie Lin, **Xiawei Xu**, Aiguo Wu, Meng He. Application of mixed crystalline semiconductor nanoparticles as SERS for Raman spectroscopy. CN114113028A.
2. Jie Lin, Aiguo Wu, Tianxiang Chen, Xuehua Ma, Meng He, **Xiawei Xu**. A composite material and its preparation method and applications. CN114113029A.
3. Jie Lin, Aiguo Wu, **Xiawei Xu**, Tianxiang Chen, Meng He. A device of circulating tumor cell isolation with its applications. CN111733072A.
4. Jie Lin, Meng He, Aiguo Wu, **Xiawei Xu**. A composite nano material with its preparation method and applications. CN111504973A。
5. Jie Lin, **Xiawei Xu**, Aiguo Wu, Yong Ren. A method for detecting circulating tumor cells. 202111164472.7.

## List of Figures

|                   |   |    |
|-------------------|---|----|
| <b>Figure 1.1</b> | The schematic of metastatic process   | 4  |
| <b>Figure 1.2</b> | Label-dependent microfluidic methods for CTC isolation                              | 22 |
| <b>Figure 1.3</b> | Label-independent microfluidic methods for CTC isolation                            | 28 |
| <b>Figure 1.4</b> | Multi-step methods for CTC isolation  | 31 |
| <b>Figure 1.5</b> | Application of SERS detection in biosensing   | 40 |
| <b>Figure 1.6</b> | Schematic representation of gold-iron oxide composite nanoparticles                 | 43 |
| <b>Figure 2.1</b> | The photos of equipment   | 55 |
| <b>Figure 2.2</b> | Chemistry synthesis process of SPION-PEI@AuNPs based SERS biological probe          | 58 |
| <b>Figure 2.3</b> | The photos of equipment   | 62 |
| <b>Figure 2.4</b> | Chemistry synthesis process of B-TiO <sub>2</sub> based SERS biological probe       | 63 |
| <b>Figure 2.5</b> | Optical image of microfilter  | 69 |
| <b>Figure 2.6</b> | The schematic of a WBC flowing through a hole of the microfilter                    | 73 |
| <b>Figure 3.1</b> | Design of magnetic SERS biological probe and separation mechanism                   | 79 |
| <b>Figure 3.2</b> | TEM images of parts of SPION-PEI@AuNPs based SERS biological probe                  | 81 |
| <b>Figure 3.3</b> | Zeta potential distribution of parts of SPION-PEI@AuNPs based SERS biological probe | 82 |
| <b>Figure 3.4</b> | SERS spectral of parts of SPION-PEI@AuNPs based SERS biological probe               | 82 |
| <b>Figure 3.5</b> | Optical images of MCF-7 and A549 under Raman instrument                             | 84 |
| <b>Figure 3.6</b> | SERS imaging and Raman spectral of MCF-7 and A549                                   | 85 |
| <b>Figure 3.7</b> | Optical image and Raman spectral of separated MCF-7 cells                           | 86 |

|                    |   |     |
|--------------------|---|-----|
| <b>Figure 3.8</b>  | SERS detection results of blood samples from healthy people                   | 87  |
| <b>Figure 3.9</b>  | SERS detection results of tumor blood samples                                 | 88  |
| <b>Figure 4.1</b>  | Optical photo of P25 and B-TiO <sub>2</sub>                                   | 93  |
| <b>Figure 4.2</b>  | TEM image and HRTEM image of B-TiO <sub>2</sub>                               | 93  |
| <b>Figure 4.3</b>  | FFT image of B-TiO <sub>2</sub>   | 93  |
| <b>Figure 4.4</b>  | X-ray diffraction of P25 and B-TiO <sub>2</sub> NPs                           | 94  |
| <b>Figure 4.5</b>  | Raman characterization of P25 and B-TiO <sub>2</sub>                          | 94  |
| <b>Figure 4.6</b>  | SERS spectra of B-TiO <sub>2</sub> -AR and P25-AR                             | 94  |
| <b>Figure 4.7</b>  | SERS spectra of AR, B-TiO <sub>2</sub> and B-TiO <sub>2</sub> -AR NPs         | 97  |
| <b>Figure 4.8</b>  | Measurement of AR conjugation   | 97  |
| <b>Figure 4.9</b>  | TEM image of B-TiO <sub>2</sub> -AR-PEG                                       | 98  |
| <b>Figure 4.10</b> | Measurement of FA conjugation   | 98  |
| <b>Figure 4.11</b> | Fluorescent images of FA modified and non-FA modified SERS biological probe   | 99  |
| <b>Figure 4.12</b> | SERS spectra B-TiO <sub>2</sub> -AR-PEG-FA and B-TiO <sub>2</sub> -AR         | 99  |
| <b>Figure 4.13</b> | FR expression of MCF-7, A549 and Raw264.7                                     | 100 |
| <b>Figure 4.14</b> | Optical images of MCF-7 and A549 under Raman instrument                       | 101 |
| <b>Figure 4.15</b> | Fluorescent images of A549 and MCF-7 incubated with SERS biological probe     | 102 |
| <b>Figure 4.16</b> | Optical image and SERS mapping image of MCF-7 and A549                        | 103 |
| <b>Figure 4.17</b> | SERS spectral of SERS bio-probe with MCF-7 and A549                           | 104 |
| <b>Figure 4.18</b> | Fluorescent images of MCF-7 and Raw264.7 incubated with SERS biological probe | 105 |

|                   |   |     |
|-------------------|---|-----|
| <b>Figure 5.1</b> | Scheme of CTC detection process   | 109 |
| <b>Figure 5.2</b> | The effects of different blood flow rates on WBCs flowing through the pore of the microfilter   | 111 |
| <b>Figure 5.3</b> | The variations in cell volume and maximum contact pressure of a WBC flowing through a micropore | 113 |
| <b>Figure 5.4</b> | The variations in cell volume and maximum contact pressure of a CTC flowing through a micropore | 113 |
| <b>Figure 5.5</b> | Schematic illustration detection results of CTC detection steps                                 | 115 |
| <b>Figure 5.6</b> | Schematic illustration of CTC detection based on microfilter and SERS spectra                   | 117 |
| <b>Figure 5.7</b> | Optical image and SERS spectral of captured cells from healthy people                           | 118 |

## List of Tables

|                         |  |     |
|-------------------------|--|-----|
| <b>Table 1.1</b>        | Biomarkers related with CTCs in different types of cancer                        | 6   |
| <b>Table 1.2</b>        | SERS performance of previously published SERS-active semiconductor nanomaterials | 35  |
| <b>Table 2.1</b>        | Geometry of microchannel   | 71  |
| <b>Table 2.2</b>        | Physical parameters of leukocytes and blood                                      | 71  |
| <b>Appendix Table 1</b> | Performance of label-dependent microfluidic methods for CTC isolation            | 142 |
| <b>Appendix Table 2</b> | Performance of label-independent microfluidic methods for CTC isolation          | 143 |
| <b>Appendix Table 3</b> | Performance of multi-step methods for CTC isolation                              | 144 |

## List of Abbreviations

|                          |                                       |
|--------------------------|---------------------------------------|
| <b>3D</b>                | Three-Dimensional                     |
| <b>AFM</b>               | Atomic Force Microscope               |
| <b>Ag</b>                | Silver                                |
| <b>AgFON</b>             | Silver Film Over Nanosphere           |
| <b>ALD</b>               | Atomic Layer Deposition               |
| <b>AR</b>                | Alizarin Red                          |
| <b>Au</b>                | Gold                                  |
| <b>B-TiO<sub>2</sub></b> | Black Titanium Dioxide                |
| <b>CE</b>                | Chemical Enhancement                  |
| <b>CK</b>                | Cytokeratin                           |
| <b>Cu</b>                | Copper                                |
| <b>COPD</b>              | Chronic Obstructive Pulmonary Disease |
| <b>CT</b>                | Computed Tomography                   |
| <b>CTC</b>               | Circulating Tumor Cell                |
| <b>CNVs</b>              | Copy Number Variations                |
| <b>DEP</b>               | Dielectrophoresis                     |
| <b>DFF</b>               | Dean Flow Fractionation               |
| <b>DLD</b>               | Deterministic Lateral Displacement    |
| <b>EE</b>                | Electromagnetic Enhancement           |
| <b>EF</b>                | Enhancement Factor                    |
| <b>EMT</b>               | Epithelial-Mesenchymal Transition     |
| <b>EpCAM</b>             | Epithelial Cell Adhesion Molecule     |
| <b>FA</b>                | Folic Acid                            |
| <b>FDA</b>               | Food And Drug Administration          |

|              |   |
|--------------|---|
| <b>FISH</b>  | Fluorescence In Situ Hybridization            |
| <b>FMSA</b>  | Flexible Micro Spring Array                   |
| <b>FR</b>    | Folate Receptor                               |
| <b>GeIMA</b> | Methacrylated Gelatin                         |
| <b>GSSG</b>  | Oxidized Glutathione                          |
| <b>HB</b>    | Herringbone                                   |
| <b>hMAM</b>  | Human Mammaglobin                             |
| <b>IF</b>    | Immunofluorescence                            |
| <b>IHC</b>   | Immunohistochemistry                          |
| <b>LOD</b>   | Limit Of Detection                            |
| <b>LSPRs</b> | Localized Surface Plasmon Resonances          |
| <b>MET</b>   | Mesenchymal-Epithelial Transition             |
| <b>MRI</b>   | Magnetic Resonance Imaging                    |
| <b>NAADP</b> | Nicotinic Acid Adenine Dinucleotide Phosphate |
| <b>N/C</b>   | Nucleus To Cytokeratin Ratio                  |
| <b>NIR</b>   | Near Infrared                                 |
| <b>NPs</b>   | Nanoparticles                                 |
| <b>OS</b>    | Overall Survival                              |
| <b>PBMC</b>  | Peripheral Blood Mononuclear Cell             |
| <b>PDMS</b>  | Polydimethylsiloxane                          |
| <b>PET</b>   | Positron Emission Tomography                  |
| <b>PFS</b>   | Progress-Free Survival                        |
| <b>PICT</b>  | Photoinduced Charge Transfer                  |
| <b>SERS</b>  | Surface-Enhanced Raman Scattering             |
| <b>SNVs</b>  | Single-Nucleotide Variations                  |

**SPION** Superparamagnetic Iron Oxide Nanoparticles

**WBC** White Blood Cells

## **Chapter 1 Introduction**

Cancer is a leading cause of death worldwide with increasing incidence and death cases. In 2021, an estimated 19.29 million new cancer cases occurred and almost 9.96 million cancer cases caused death[1]. There has been consistent growth in global cancer burden, which imposes enormous stress of health, emotion and finance on individual, family, community, and health systems. High proportion of the cancer patients in developing countries including China, are not able to access timely or high-quality treatment and diagnosis. The delay in cancer diagnosis and treatment would increase cancer disability and mortality. There is consistent evidence showing that the early diagnosis with timely treatment could reduce cancer mortality[2-5]. Therefore, early diagnosis and treatment are critical important during comprehensive cancer control. If the tumorigenesis and tumor metastasis can be detected earlier by some reliable detection technologies, the tumors can be strangled in the early stage, thereby improving the treatment and prognosis of cancer. However, early clinical symptoms of tumors are normally atypical, thus, the early diagnosis and treatment of cancer diseases is a worldwide challenging problem. The traditional clinical and imaging diagnostic methods, such as Magnetic Resonance Imaging (MRI), Computed Tomography (CT) and Positron Emission Tomography (PET), are difficult to find early tumor tissue and unable to realize effective diagnosis of early tumors. The inconvenient collection of samples caused the stagnant study of solid tumor. In the background of

precision medicine, liquid biopsy technology, with advantages of convenient, minimally invasive, and able to observe tumorigenesis dynamically, has developed rapidly and attracted increasing attention nowadays. Benefit from the continuous innovation of molecular biology technology, the sensitivity and the specificity of liquid biopsy have been improved significantly. Considerable evidence has emerged that cancer cells and related issues would release biomarkers such as circulating tumor cells (CTCs), DNA, RNA, and exosomes into circulating blood. The amount and the type of these biomarkers are closely related to tumor tumorigenesis. Circulating tumor cells are tumor cells shedding from solid tumor and circulating in the blood, which has been used as a biomarker in the detection of peripheral blood of cancer[6]. The comparison between conventional invasive biopsy and CTC detection shows that CTC detection has many advantages apart from high specificity. For examples, samples could be collected in a gentled way, so that better patient compliance can be achieved. More importantly, CTC detection is not limited by tumor heterogeneity, because CTCs could shed from primary tumor as well as metastatic tumor. Therefore, they are carrying more complete information about tumor development. Many tumor challenges, such as accurate auxiliary diagnosis, real-time monitoring, therapeutic evaluation, and prognosis judgment of tumors are expected to be achieved[7]. In addition, CTCs carry a wealth of information about tumorigenesis, tumor progression, metastasis, and drug resistance that can help understand and control tumor diseases. However,

CTC detection is limited by its heterogeneity and extremely small number of CTCs (1-10 CTCs per milliliter) in the blood. Therefore, it is necessary to develop more effective CTC isolation and detection methods.

In this chapter, research background and literature review of circulating tumor cell have been reviewed. Based on the literature review, the limitations of current technology would be summarized and considered for research design. Finally, outlines of this thesis focused on the research of SERS and microfluidics-based CTC detection method.

## **1.2 Circulating tumor cells**

Circulating tumor cells are tumor cells shedding from the solid tumor, intravasating into blood and lymphatic vessels, and translocating to distant tissues via circulation[8]. Figure 1.1 showed the origin of CTCs. During the process of tumor development, CTCs would enter circulation system spontaneously or under the influence of external factors, carrying a large amount of information about tumorigenesis, tumor progression, metastasis, and drug resistance[9]. The survived CTCs would cause tumor metastasis by shedding, invasion, intravasation, circulation, extravasation, and formation of secondary tumor[10]. Current studies show that cancer metastasis causes approximately 90% death of cancer. The detected CTCs in peripheral blood presage the possibility of tumor metastasis. Therefore, CTCs have been

considered as effective biopsy method and able to realize accurate auxiliary diagnosis, real-time monitoring, therapeutic evaluation, and prognosis judgment of tumors[7].

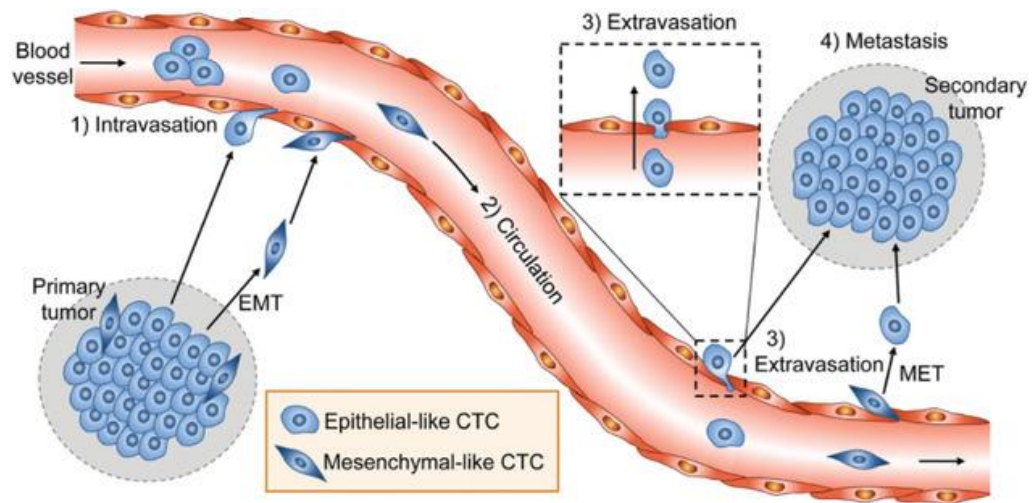


Figure 1.1: The schematic of metastatic process including (1) CTC invasion into blood vessels from primary tumor; (2) circulation of CTCs in blood vessel; (3) extravasation after CTC adhesion to blood vessel walls; (4) metastasis and formation of secondary tumor[11].

### 1.2.1 Biological properties of CTCs

The biological characteristics of CTCs are commonly affected by protein expression, gene mutation, single-nucleotide variations (SNVs), or copy number variations (CNVs) of CTCs. The analysis of the biological characteristics of CTCs can clarify the relationship between CTCs and tumor progression, guide precise anticancer therapy, distinguishing CTCs from other cells and evaluate the targeted drug therapy. The half-life period of CTCs

shedding from solid tumor of cancer patients is 1-2.4 h in the circulation system, related to the immune reactions of CTCs involved in the circulation system[12]. CTCs derived from epithelial tumors have the characteristics of epithelial-mesenchymal transition (EMT) and mesenchymal-epithelial transition (MET)[13]. In the EMT process, the surface markers of epithelial cells would be downregulated while the markers of mesothelial cells would be upregulated. Thus, tumor cells would be promoted to break away from intercellular adhesion and acquire variability and invasiveness. In the contrast, the MET process enables CTCs from EMT process to reverse and restore the epithelial phenotype, regain the ability of adhesion, and form metastases[14]. Because CTCs were shed from solid tumor, they have the properties of epithelial cell and mesenchymal cell and can express Epithelial Cell Adhesion Molecule (EpCAM) antigen on their surface, which can be used to distinguish CTCs from blood cells. However, isolation methods only based on EpCAM may limit the detection specificity of CTCs from other types of cancers, so organ-specific cell surface markers or stem cell markers have been used to enrich CTCs. For example, in addition to the commonly used EpCAM, the other biomarkers, such as CK19, HER2, ER, PR, and MUC1, are also used in breast cancer diagnosis[15]; EGR, and PTEN are used for prostate cancer diagnosis[16]; and EpCAM, ASGPR1, N cadherin, Vimentin, Gpc3, and AFP are used for hepatocellular carcinoma diagnosis[17]. The related biomarkers of CTCs have been summarized in Table 1.1.

Table 1.1: Biomarkers related with CTCs in different types of cancer

| <b>Biomarkers</b>   | <b>Related Cancer Type</b>                               |
|---|--|
| <b>EpCAM:</b> Epithelial Cell Adhesion Molecule                               | Breast Cancer, Prostate Cancer, Hepatocellular Carcinoma |
| <b>CK19:</b> Cytokeratin-19   | Breast Cancer  |
| <b>HER2:</b> Human Epidermal Growth Factor Receptor-2                         | Breast Cancer  |
| <b>ER:</b> Estrogen Receptor  | Breast Cancer  |
| <b>PR:</b> Progesterone Receptor  | Breast Cancer  |
| <b>MUC1:</b> Mucin-1  | Breast Cancer  |
| <b>EGR:</b> Early Growth Response Factor                                      | Prostate Cancer  |
| <b>PTEN:</b> Gene of Phosphate and Tension Homology Deleted on Chromosome Ten | Prostate Cancer  |
| <b>ASGPR1:</b> Asialoglycoprotein Receptor-1                                  | Hepatocellular Carcinoma                                 |
| <b>N cadherin:</b> N Cadherin   | Hepatocellular Carcinoma                                 |
| <b>Vimentin</b>   | Hepatocellular Carcinoma                                 |
| <b>Gpc3:</b> Glypican-3   | Hepatocellular Carcinoma                                 |
| <b>AFP:</b> Alpha Fetoprotein   | Hepatocellular Carcinoma                                 |

### 1.2.2 Physical properties of CTCs

Due to the abnormal metabolism and metabolic disorder of tumor cells after entering circulation system, the change of composition of intracellular substances, gene expression and modification, protein synthesis and aggregation of some polar particulate matters lead to changes of CTCs' physical properties, which are different from normal cells and normal tissue cells.

### **Size and density**

There have been many studies measuring the size of tumor cell and blood cell normally by optical microscopy and flow cytometry. Erythrocytes have a diameter of 7-8.5  $\mu\text{m}$  with volume of  $100.6 \pm 4 \mu\text{m}^3$  and leukocytes are 5-13  $\mu\text{m}$  in diameter, including granulocytes with diameter of 7.3-13.2  $\mu\text{m}$ , lymphocytes with diameter of 5.2-10.5  $\mu\text{m}$ , and monocytes with diameter of 9.7-10.5  $\mu\text{m}$ [18]. In general, the average diameter of leukocytes is less than 10  $\mu\text{m}$  with wide size distribution. The average diameter of cancer cell lines used to validate various CTC isolation techniques ranged from 15 to 25  $\mu\text{m}$ , which was significantly larger than that of WBCs. However, cells from cancer cell lines may be larger than CTCs from cancer patients with same cancer type. For examples, CTCs of breast cancer have the average diameter of 13  $\mu\text{m}$  while the diameter of breast cancer cell lines is 15-17  $\mu\text{m}$ ; CTCs of prostate cancer have the average diameter of 6.16-9.78  $\mu\text{m}$ , which is much smaller than the diameter of prostate cancer cell lines, 10.84-15.92  $\mu\text{m}$ [19]. The size difference between CTCs and WBCs is less clear than the difference between cancer cell lines and WBCs. The size distribution of CTCs and WBCs is partly overlapped[20]. Besides, CTCs from different melanoma cancer patients have different size distribution. The maximum size of CTCs from two patients is larger than 12  $\mu\text{m}$  while some of CTCs from one patient are smaller than 10  $\mu\text{m}$ [21]. Therefore, it is limited to only use cancer cell lines treated blood sample for

validation of isolation technology. More realistic samples with variable size distribution of cancer cell lines should be carried out for validation.

CTCs can also be isolated from blood cells by density gradient centrifugation system depending on the density difference of different cells[22]. Erythrocytes and granulocytes have the density higher than separation medium and will precipitate at the bottom of the pipe after centrifugation, while monocytes and lymphocyte have the density smaller than separation medium and will float in the upper layer of separation medium or suspended in medium. CTCs are mainly deposited in the monocyte enrichment layer. After using Ficoll-Paque medium with a density of 1.077 g/mL, CTCs might be detected in the Peripheral Blood Mononuclear Cell (PBMC) layer. However, the density of CTCs is not accurately defined and probably is not uniform. Research shows that some CTCs from prostate and pancreatic cancer appeared much heavier and could not be separated with separation medium with density of 1.077 g/mL[23]. Therefore, the isolation methods based on density should be improved.

### **Morphology and stiffness**

The cell morphology of CTCs and WBCs is different. Some studies have shown that CTCs have lower roundness than WBCs[24]. Most CTCs from breast, colorectal, and prostate cancer have the roundness of  $1.5\pm 0.6$ ,  $1.5\pm 1.4$ ,

and  $1.5 \pm 0.8$ , respectively, while the roundness of WBCs is  $1.8 \pm 1.2$ . Apart from cell morphology, the deformability difference between tumor cells and blood cells can also be used for isolation. When cells are encountering forces or restrictions, they will deform to pass through the pores which are even much smaller than cells[25-27]. The cell deformability can be defined by Elastic properties, such as stiffness and Young's modulus, which can be investigated by Atomic Force Microscope (AFM)[28], micropipette aspiration[29], laser optical trapping[30], and microfluidic device[31]. The stiffness of cells is represented by Young's modulus, which can be used to determine cell deformability. Previous studies show that the stiffness of tumor cells ranges from 200 to 2000 Pa with that of neutrophils from  $156 \pm 87$  Pa[32]. However, Lee et al. reported that the stiffness of neutrophils is  $1548 \pm 871$  Pa in center region,  $686 \pm 801$  Pa at the leading edges, and  $494 \pm 537$  Pa at trailing edge, which is similar with the stiffness distribution of tumor cells[33]. Besides, the stiffness of nucleus is higher than that of cytoplasm. Nucleus to cyto keratin ratio (N/C) is defined as the ratio of nuclear area to cytoplasmic area[19]. The N/C ratio of CTCs is higher than 0.8 while the N/C ratio of WBCs is much smaller than 0.8[32]. CTCs from breast, colorectal, and prostate cancer have N/C ratio of  $0.8 \pm 2.8$ ,  $1.0 \pm 3.5$ , and  $1.0 \pm 2.1$ , respectively[24]. Therefore, CTCs are concerned to be stiffer than WBCs. In additions, many researchers have studied the relationship between cancer metastatic potential and stiffness and found that CTCs with higher stiffness have lower metastatic potential[34].

## **Electrical properties**

The cell capacitance can reflect the area of plasma membrane resulting from cell transport phenomena and metabolism[35]. Therefore, some researchers use total capacitance to analyze the morphology and physiological states of cells, which has been used to quantify heterogeneity of breast cancer cell lines[36]. Different cell types have significant differences in the membrane capacitance, which has been applied on dielectrophoresis (DEP) method to separate different cell types. Cancer cells have different cell capacitance because of their abnormal transport phenomena and metabolism as well. Besides, under the stimulation of external environment, CTCs induce cell gene expression and the change of membrane skeleton structure and adhesion, which affects the surface charge of cell membrane to resist the shear force of blood fluid. It is reported that breast cancer cells have smaller mean association constant of hydrogen ions, which means that CTCs have more negative charges[37]. The difference in electric properties combined with size difference between CTCs and blood cells can facilitate CTC isolation.

### **1.3 Clinical application of CTCs**

In recent years, clinical trials have demonstrated that CTCs have important value for tumor early diagnosis, prognosis evaluation, therapeutic efficacy, tumor stage and monitoring of tumor recurrence or metastasis.

### **1.3.1 CTCs and early diagnosis**

The theory of CTC detection applied in tumor early diagnosis was based on the research results of animal model[38]. Researchers used mice models to study breast cancer, finding that CTCs could be appeared at early stage of primary tumor formation. In the mice models of pancreatic cancer, CTCs was found in the blood circulation before the formation of solid tumor.

However, there are two key issues remaining in the application of CTC detection in tumor early diagnosis. First, the clinical research found that benign disease patients also have the presentence possibility of CTCs. For examples, Tanaka et al. found that 12% of benign lung disease patients could be detected with CTCs[39]; Pantel et al. have also detected CTCs in the 11% of benign colon diseases patients[40]. Second, the number of CTCs in the blood at the early tumor stage is extremely low. In one milliliter of blood, there are 1-10 CTCs with  $10^6$  white blood cells and  $10^9$  red blood cells[41]. Besides, due to the rarity of CTCs, no relevance has been found between the number of detected CTCs and tumor volume, tumor classification. Therefore, it is important to develop more sensitive methods for CTC detection.

Although there are several difficulties in CTC detection applied in early tumor diagnosis, it has still been proved that CTC detection is a potential method in

term of early tumor diagnosis. Ilie et al. have detected CTCs in patients with Chronic Obstructive Pulmonary Disease (COPD). Besides, in the follow-up detection within 1-4 years, patients with detected CTCs have been diagnosed with early stage of lung cancer by CT and pathologic biopsy[42]. Therefore, CTC detection has important scientific significance and application value for early diagnosis of tumor.

### **1.3.2 CTCs and prognosis evaluation**

The number of CTCs at different stages of tumor are different which could be considered as an analysis basic of prognosis evaluation. Cristofanilli et al. have verified the hypothesis that the level of circulating tumor cells can predict survival in metastatic breast cancer[43]. In this research, they found that the Progress-Free Survival (PFS) and the Overall Survival (OS) of patients correlated with the number of detected CTCs in circulation. Patients with more than 5 detected CTCs per 7.5 ml peripheral blood have obviously shorter survival and worse prognosis. In the following clinical studies, the corresponding relationship between CTC number and prognosis or treatment evaluation has also been proved to be applicable to prostate cancer, colorectal cancer, and other cancer patients[44, 45].

### **1.3.3 CTCs and therapeutic efficacy**

Nowadays, growing number of tumor clinical research have considered CTCs

as an important value in therapeutic efficacy[46]. As mentioned above, Cristofanilli et al. also applied CTC counting to the monitoring of metastatic breast cancer. In 2006, Budd et al. tested 138 metastatic breast cancer patients with imaging detection and CTC counting before and a median of 10 weeks after the initiation of therapy[47]. They find that patients with more than 5 CTCs in 7.5 mL blood were associated with shorter PFS and OS. Besides, by comparing the use of CTCs to radiology for prediction of OS, they found that assessment of CTCs was an earlier, more reproducible indication of disease status than current imaging methods. CTCs may be a superior surrogate end point, as they are highly reproducible and correlate better with overall survival than do changes determined by traditional radiology.

#### **1.4 CTC detection: isolation and downstream analysis of CTCs**

90% of malignant tumor was derived from the epithelial cells where the epithelial tissue cells have extremely different gene expression and biological characteristics compared to other tissue cells, such as blood cells. Therefore, most of CTC detection methods have been developed depending on the difference between epithelial tissue cells and blood cells. However, after decades of development, CTC detection is still challenged because of the extremely small number of CTCs in blood and the differences in size, morphology, molecular marker, gene expression and mutation of CTCs caused by the heterogeneity of CTCs[48, 49]. In general, the CTC detection has two

stages: isolation of CTCs (capture and enrichment), and downstream analysis of CTCs (detection and release)[50].

#### **1.4.1 Isolation technology of CTCs**

CTC isolation methods have been divided into two major categories based on biological characteristics and physical characteristics. The former is mainly based on CTCs' biological characteristics that are different from normal blood cells such as expression to epithelial cell adhesion molecule (EpCAM), which has been classified as label-dependent methods. The latter is mainly based on physical differences between CTCs and blood cells such as size, density, deformability, and electric properties, which has been classified as label-independent methods. The label-dependent methods could also be classified into positive isolation and negative isolation. Positive isolation of CTCs is commonly achieved by EpCAM which is a kind of cell surface marker expressed in CTCs. In negative isolation, WBCs are depleted by antibody against CD45 or other leukocyte antigens. The label-dependent isolation has high specificity but is limited by low surface protein expression level and inherent heterogeneity of tumor cells. In contrast, the label-independent isolation does not depend on cell surface marker expression level. Compared to label-dependent isolation, label-independent isolation can be accomplished in a low cost, simple and fast way. However, it suffers from low specificity because of overlap in size, density, and stiffness between CTCs and WBCs. The

CellSearch system was one of CTC detection technologies based on biological characteristics of CTCs and was the first CTC detection product approved by U.S. Food and Drug Administration (FDA). It could be used for CTC detection and enumeration for metastasis breast, colorectal, and prostate cancer. However, it was limited by its complicated detection process, low purity ( $< 0.5\%$ ) and sensitivity (high false positive and false negative rates)[50]. Therefore, it is urgently needed to develop novel approaches to improve the CTC detection technology, which demands better understanding of biological and physical properties of CTCs. Microfluidics has rapidly developed recently and has become a promising way to tackle the challenges, which has been overviewed in Section 1.5.

#### **1.4.2 Downstream analysis of CTCs**

After isolation, there need to be some analysis methods to identify the isolated cells and distinguish CTCs from background cells. Besides, apart from CTC counting for preliminary clinical decision, molecular profiling of clinically relevant CTCs subpopulations is important for the study of tumorigenesis, tumor progression, metastasis, and drug resistance. The recent technological for molecular characterization of CTCs are based on cellular morphology, cellular immunology and cellular molecular.

Compared to the normal blood cells, CTCs have abnormalities of structure,

function, and metabolism, which is the basics of CTC morphologic change[51]. CTCs have some common morphologic features, such as large, irregular, and hyperchromatic nuclei with prominent nucleoli. Besides, the cytoplasm of CTCs is changed due to secretion, condensation, and keratinization. Therefore, cell dyeing can be used to identify CTCs through cellular morphology.

CTCs are shed from solid tumor retaining the properties of epithelial cells and mesenchymal cells. Therefore, they can express gene of epithelial cells and mesenchymal cells, such as Cytokeratin (CK), Vimentin, E-cadherin, and N-cadherin. Besides, the specific tumor can express tissue specific gene, for example, human mammaglobin (hMAM) for breast cancer. CTCs can be identified by immunofluorescence (IF) staining or immunohistochemistry (IHC). The commonly used genes have been mentioned in Section 1.2.1. Fluorescence in situ hybridization (FISH) can also be used to analyze CTCs through fluorescence microscopy to localize fluorescent probes binding specific DNA sequence to parts of the chromosome[52]. In recent years, Surface-Enhanced Raman Scattering (SERS) spectroscopy has been developed in application of CTC analysis. It has been widely applied as optical imaging and detection tool due to the strong signal intensity, excellent photostability, biocompatibility, and especially the multiplexing ability[53]. Through appropriate analysis methods, CTCs can be detected more effectively.

## **1.5 Microfluidics for CTC detection**

Microfluidics is characterized by dramatic reduction in sample and reagent consumption, low fabrication cost, simultaneous analysis of hundreds of samples in short time, and high integration of multiplexing functions such as sample pretreatment, transportation, mixing, reaction, separation, and detection on the same microdevice. It can realize the whole process of sample pretreatment and analysis online[54]. Besides, microfluidic platform featured with chambers, channels, and other nanostructures, such as pillars, tube, rod, and wires, can be used for cell separation because of their biomimetic surface conditions. Because these characteristics are suitable to CTC isolation and analysis as well, many microfluidic devices have been developed for CTC isolation[55]. The microfluidic methods have also been classified into label-dependent methods and label-independent methods.

### **1.5.1 Label-dependent technologies**

Label-dependent technologies, also called affinity-based technologies, depend highly on the expression difference of cell surface markers between CTCs and normal blood cells. Most label-dependent technologies are positive enrichment, that is, capturing CTCs by EpCAM. In addition to positive enrichment, negative CTCs enrichment uses leukocyte-specific surface markers, such as CD45 and CD66b, to deplete leukocytes. Figure 1.2 shows some typical label-dependent microfluidic methods for CTC isolation, and the performance is

summarized in Appendix Table 1.

### **Immunocapture**

Immunocapture is the most traditional method among label-dependent technologies for CTC isolation. The surface of microfluidic features or channels can be coated with ligands or capture molecules which can combine with the surface markers of CTCs, as shown in Figure 1.2A[56]. When blood flows through the chip, CTCs will be captured and stay in the channel while other blood cells are taken away. In immunocapture method, varieties of structures are designed to improve the performance of CTC isolation. Micropost array can create turbulent flow to increase the contact chance of CTCs with ligand on the channel. Nagrath et al. developed a microfluidic platform fabricated with EpCAM coated microposts, which has successfully isolate CTCs from the blood[57]. Chaotic mixing is also used to increase the contact area between CTCs and channel surface. For example, the structure of grooved herringbone (HB) pattern is commonly utilized[20]. Immunocapture methods also use nanomaterials and nanostructures with high surface area-to-volume ratio to increase surface coated with antibody, and thereby to improve the capture efficiency. Tseng et al. introduced a NanoVelcro microfluidic device employing silicone nanopillars[58], silicone nanowires[59], and nanofibers coated with antibodies[60].

### **Hydrogel-based capture**

Hydrogel is a kind of polymer material with three-dimensional (3D) network structure formed by chemical or physical crosslinking. It can swell in water instead of dissolving. Compared with other materials, hydrogel has obvious advantages, such as high-water content, soft properties, high permeability, and good biocompatibility and so on, which make it widely used in CTC separation[61-63]. Using the intelligent response of hydrogel to light and heat, researchers fabricated a capture substrate for CTC capture and release. As shown in Figure 1.2B, a near infrared (NIR) light-responsive substrate was designed to capture CTCs by immunocapture and release CTCs by a kind of thermos-responsive hydrogel. This method allows single CTC capture and recovery of captured CTCs[64]. Luan et al. developed a hybrid photonic barcode functionalized with folic acid (FA) to capture and release of CTCs with methacrylated gelatin (GelMA) gel combined with FA molecules. The soft property of GelMA gel allows better cell viability after CTC isolation[49].

### **Immunomagnetic capture**

The immunomagnetic method use magnetic nanoparticles coated with antibodies, aptamers, or peptides, which can capture CTCs and isolate CTCs from blood cell by a magnetic field. The CellSearch system is based on immunomagnetic method. The method can be classified into positive isolation focusing on capture of CTCs and negative isolation focusing on capture of

leukocytes or erythrocyte. In some positive isolation methods, the captured CTCs will be adsorbed in the microchannel, making it difficult for downstream analysis of CTCs. Therefore, Saliba et al. developed a microfluidic device with antibody functionalized superparamagnetic beads which can self-assemble with magnetic traps in the microchannel. The capture efficacy is higher than 94%[65]. However, the self-assembled magnetic columns used in these methods are often unstable due to the large hydrodynamic drag force, which results in low throughput. Figure 1.2C shows a magnetic force gradient-based microfluidic chip which can separate CTCs depending on their expression level of EpCAM. This device can isolate CTCs from 3 mL blood within 1 hour[66]. Among negative isolation methods, magnetic nanobeads coated with anti-CD45 antibodies have been commonly used for separating WBCs from CTCs, thereby enriching CTCs[67]. Although the recovery rate of this negative method is higher than that of positive method, the purity of isolated CTCs is relatively low; therefore, further isolation is required.

### **Immunofluorescence**

Fluorescence in situ hybridization (FISH) is a method that uses specific DNA sequences tagged with fluorophores to detect chromosome or gene status in the nucleus[68]. Conventional FISH technique is time consuming, labor intensive, and expensive[69]. It usually takes 2 or 3 days to complete analysis and the reagent required for assay is expensive such as fluorescently labeled DNA

probes. Therefore, microfluidics-based FISH device has been developed to test CTCs, which can highly reduce time and cost compared to the conventional FISH. After CTCs isolated from blood by microfluidic chip, FISH is used to carry out single-cell molecular diagnosis[70]. Zhao et al. introduced an automatic CTC counting method based on microfluidics and line confocal microscopy. As shown in Figure 1.2D, blood sample was directly labeled with a variety of antibodies combined with different fluorophores and pumped into microchannels linked with line-confocal microscope. Based on the fluorescence signal, CTCs can be counted automatically. Besides, 1 mL blood sample can be analyzed within 30 min due to the high flow rate[71]. The label-dependent technologies can achieve high specific and purity due to specific expression of CTCs. However, label-dependent technologies face the challenges of high cost of antibodies, low flow velocity, and small sample volume.

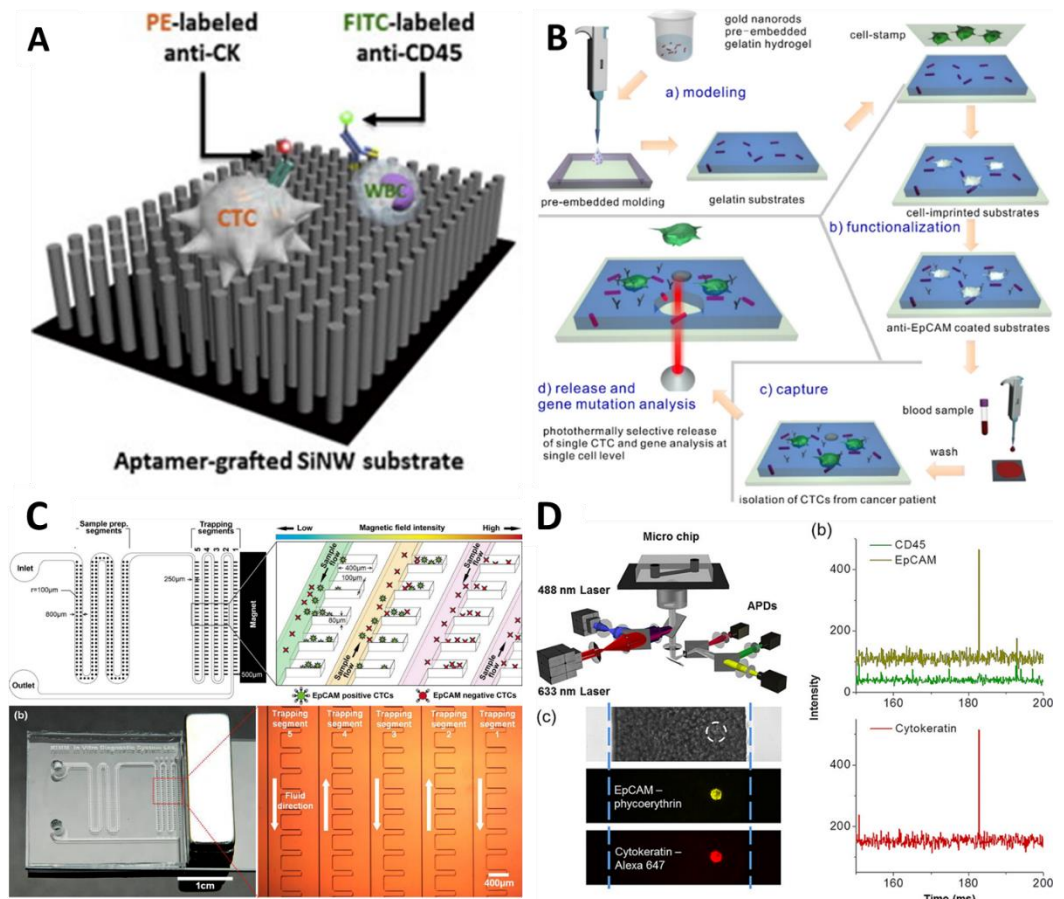


Figure 1.2: Examples of label-dependent microfluidic methods for CTC isolation. (A) Immunocapture isolation method with aptamer grafted SiNW substrate[56]; (B) Hydrogel-based capture isolation method with NIR-responsive cell-imprinted gelatin[64]; (C) Magnetic force gradient based microfluidic chip[66]; (D) Immunofluorescence isolation method based on microfluidics and line confocal microscopy[71].

### 1.5.2 Label-independent technologies

Label-independent technologies isolate CTCs from peripheral blood based on the difference of physical properties between CTCs and blood cells. Label-independent method has advantages of isolating CTCs from blood without any

expression of tumor-specific surface markers and maintaining CTCs activity. Figure 1.3 demonstrates some of label-independent microfluidic methods for CTC isolation, and the performance is summarized in Appendix Table 2. Based on the physical differences of size, density, stiffness, morphology and electrical properties, CTCs can be isolated by microfiltering, hydrodynamics, DEP, and acoustophoresis methods.

### **Mechanical filtering**

Mechanical filtering isolation methods use the difference of size and deformability between CTCs and blood cells to isolate CTCs from blood. Almost CTCs have larger cell size and higher stiffness than blood cells. The microfilter commonly consists of pores, cavities, or geometric obstructions fabricated with certain arrangement[72]. When blood flows through the microfilter, the smaller RBCs, WBCs, and platelets will pass the filter while the bigger CTCs are captured. However, CTCs captured by microfilter may be damaged due to high flow rate and filtration pressure. Harouaka et al. designed a new flexible micro spring array (FMSA) device to minimize the damage of cell and maintain cell activity, as well as to increase throughput[73]. The capture efficiency of this device can reach to 90%. However, mechanical filtering isolation method is limited by clogging and adsorption because of the accumulation of cells on the filter, which will cause higher fluid driving forces, damage the captured CTCs, and reduce the isolation performance.

## **Hydrodynamics method**

The hydrodynamics method is mainly depending on the size difference and the different movement response to the hydrodynamic force. There are three main types: Deterministic lateral displacement (DLD), Dean Flow fractionation (DFF), and Microvortex.

DLD is based on the characteristic that CTCs are larger than normal blood cells and is designed with DLD array of which the critical radius is between CTCs and blood cells. CTCs, which are larger than critical radius, will move to one side after collision with arrays, while blood cells which are smaller than critical radius will keep the original path flowing through the array. Louterback et al. designed a DLD array device that can separate CTCs with the flow rate of 10 mL/min and achieve a capture efficiency higher than 85% without influence on cell viability[74]. DLD method may also suffer from clogging when detecting clinical samples that may be sticky and contain lots of debris.

DFF also uses the size difference between CTCs and blood cells. When fluid flows in a spiral channel, the velocity distribution of fluid is parabolic, with the greatest velocity in the middle of the channel leading to the greatest centrifugal force, thus, flowing to the outer edge of the channel. The fluid near the channel wall has the smallest velocity and the smallest centrifugal force, so it will be

pushed by middle fluid. To maintain equilibrium, the Dean flow is formed in the direction perpendicular to the flow of the fluid[75]. Affected by lift force and Dean drag force, larger cells will move to the inner wall and smaller cells will move to outer wall, thereby to separate CTCs from blood cells as shown in Figure 1.3A[76]. A label-free spiral microfluidic device was developed which can separate CTCs from blood with more than 85% recovery rate and 99.99% WBC depletion[77].

Microvortex is caused by inertial force with suddenly expansion-contraction construction. As shown in Figure 1.3B, when cells flow through the expansion-contraction construction, cells larger than critical size will be trapped into vortices. Based on this principle, Renier et al. used microfluidic vortex chip to isolate CTCs from patients with advanced prostate cancer and isolate CTCs with the purity of 1.74-37.59%[78]. However, some microfluidic vortex chip may cause bubbles inside channel. The microfluidic vortex chip can remove large number of WBCs even there is overlapped part between CTCs and normal blood cells[79].

### **Electrokinetics method**

The DEP method utilizes the translational motion of neutral particles in an asymmetric electric field due to dielectric polarization. The DEP force depends on the size and the cell membrane capacitance and suspended media (dielectric

constant and conductivity), electric field strength and frequency, and the viscosity of suspended media. The size and cell membrane capacitance of CTCs are different from blood cells. Therefore, compared with other conventional separation methods, DEP method has advantages of higher selectivity, easier control, and higher separation efficiency. Chiu et al. developed an optically DEP method combined with microscopic fluorescent imaging[80]. The purity of isolated CTCs can reach to 100%. Alazzam et al. described the design and microfabrication of CTC isolation microfluidic chip based on DEP. As shown in Figure 1.3C, the device consists of a group of planar interdigitated transducer electrodes. It can precisely detect and count CTCs in the blood[81]. However, DEP method is difficult in manipulation because it requires high voltage and complicate process of resuspending cellular components in an isotonic medium with low conductivity.

### **Acoustophoresis method**

Acoustophoresis is a method used to separate cells based on cellular volume and density[82]. Because cells experience acoustic force with different magnitude depending on size, density, and deformation of cells. Acoustic force will translate cells to the zero periodic pressure variations or maxima pressure node to reach a balance point. Li et al. developed an acoustic-based microfluidic device using tilted-angle standing surface acoustic waves, which can successfully separate CTCs from blood cells with high throughput and

recovery rate higher than 83%[83]. Augustsson et al. separated prostate cancer cell lines from WBCs with recovery rate ranging from 93.6 to 97.9% and purity ranging from 79.6 to 99.7% using acoustophoresis method[84]. This research also found that cell viability is almost well kept when using acoustophoresis method. Wu et al. reported a platform integrating acoustics and microfluidics to separate CTCs from blood with cell structure, biological and functional integrity remaining. As shown in Figure 1.3D, CTCs are separated in the PDMS-glass hybrid channel resonator under hydrodynamic and surface acoustic wave force[85]. However, acoustophoresis method may also cause clogging with large volume blood and high acoustic pressure which can lyse cells.

Label-independent methods have advantages of high throughput, low cost, further cell molecular characterization and cell culture. However, overlapping in CTC and WBC sizes reduces the specificity of CTC isolation. The structure of filtering microchip may cause pores clogging. To solve these limitations, multistep technologies have been considered to improve CTC isolation method.

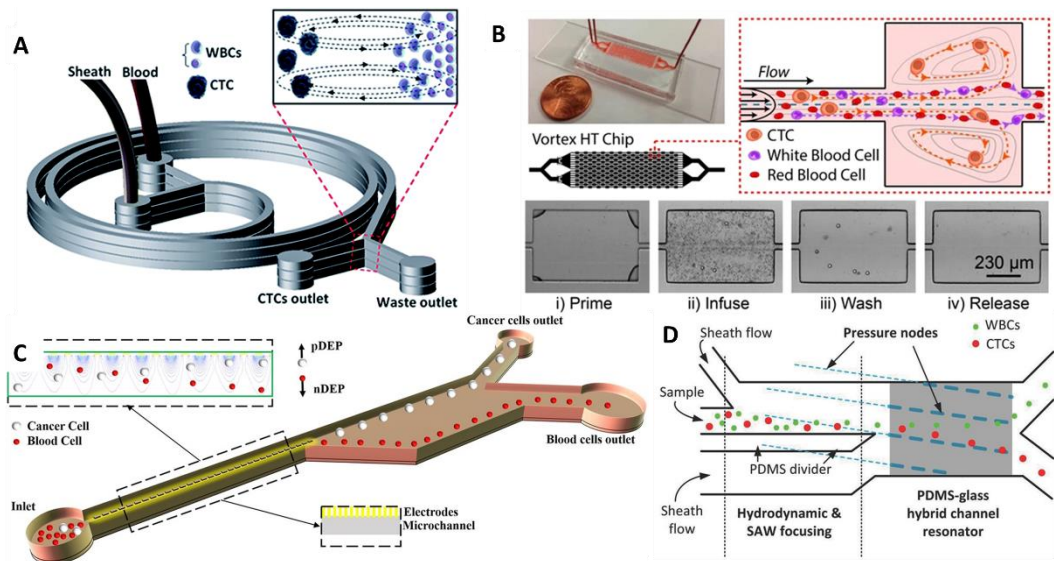


Figure 1.3: Examples of label-independent microfluidic methods for CTC isolation. (A) DLD CTC isolation with spiral microfluidic chip[76]; (B) Microfluidic Vortex HT chip[78]; (C) DEP CTC isolation[81]; (D) Acoustic CTC isolation[85].

### 1.5.3 Multistep technologies for CTC isolation

Due to the heterogeneity of CTCs, the physical and biological properties of CTCs are variable. It is not enough only to use one property to separate CTCs from blood. Therefore, multistep technologies for CTC isolation have been developed to improve the CTC capture efficiency, targeting two or more properties of CTCs. Figure 1.4 shows some of multistep technologies for CTC isolation and the performance is summarized in Appendix Table 3. A CTC isolation device was developed based on filter microstructure and size-based hydrodynamic method[86]. As shown in Figure 1.4A, CTCs are pre-separated by hydrodynamic force and further isolated by oscillatory flow. Song et al.

combined immunocapture with DLD and enhanced capture efficiency more than 300% and achieved cell viability of 96%[87]. As shown in Figure 1.4B and D, DLD was used to separate CTCs from blood cells and biomarkers coated micropillars were used to capture CTCs. Multivalent aptamer having higher binding efficiency with antigen was used as shown in Figure 1.4D while EpCAM was used as shown in Figure 1.4B. Besides, CTC-iChip was developed using DLD, DFF, and immunomagnetic methods for isolating CTCs [80]. In this design, DLD was used to separate nucleated cells from blood and delete red blood cells, and then inertial force was used to position all the cells in a line and magnetophoresis was used to remove nontarget cells. This device can capture more than 97% CTCs from blood with speed of 8 mL per hour. Ahmed et al. introduced a new device, combining DLD and immunocapture methods, in which pillars were immune-coated[88]. It has over 92% capture efficiency and 82% purity and CTCs were detected from non-metastasis colorectal patients by this method. Jack et al. developed an ultra-specific microfluidic technology based on DFF and immunomagnetic to improve the purity and throughput of CTC isolation[89]. In this design, the blood sample was presorted by inertial force to reduce unwanted cells. CTCs were subsequently labeled by EpCAM-functionalized magnetic beads and then separated by magnetophoresis. Figure 1.4C shows a dual-immunopatterned microfluidic device with double layers coated by anti-EpCAM antibody and anti-63B6 antibody respectively[90]. This device overcame the limitation of

low EpCAM expression level of CTCs and achieved 94.47% capture efficiency.

Although the combined methods have better performance for CTC isolation, they require complex design of microfluidic devices, the integration level between different parts of methods is low, the operation is more complicated, and fabrication cost is higher. These shortcomings limit downstream analysis of CTCs and the commercial development of CTC isolation by microfluidics. Therefore, it is necessary to develop a microfluidic device with simple operation, high integration and high performance for isolation and downstream analysis of CTCs.

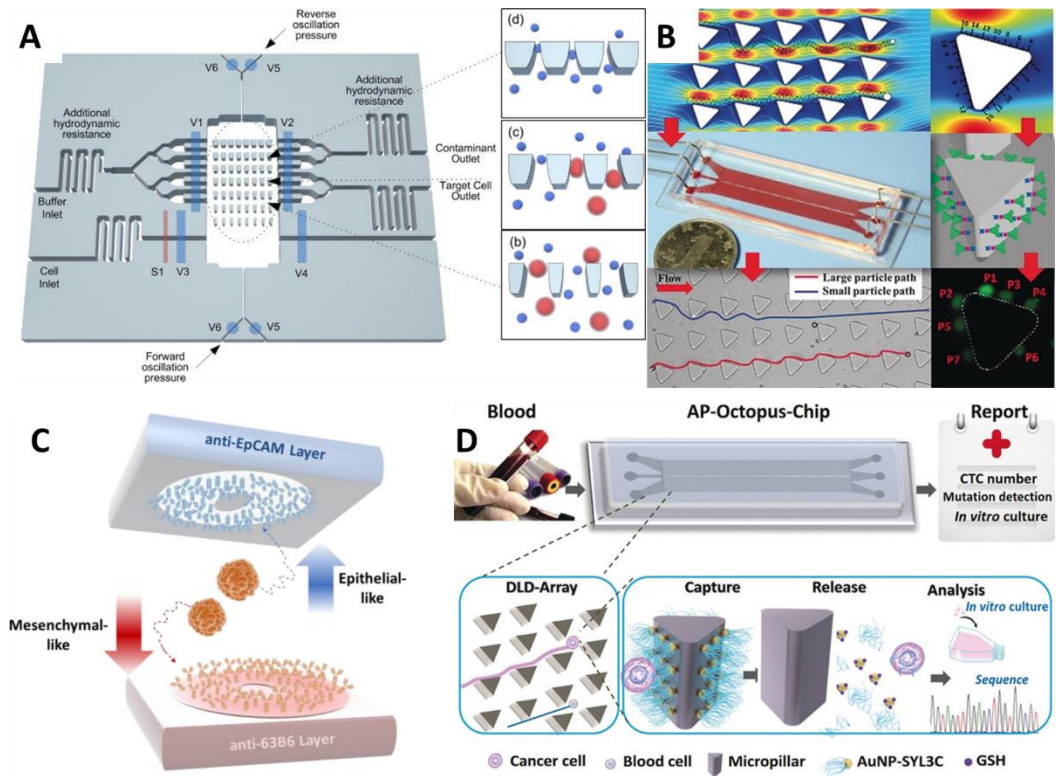


Figure 1.4: Examples of multi-step methods for CTC isolation. (A) CTC isolation by microfluidic ratchets and hydrodynamic concentrator[86]. (B) Size-dictated immunocapture chip combined immunocapture and DLD methods[88]; (C) Immunocapture method using two types of antibody, anti-EpCAM antibody, and anti-63B6 antibody[90]; (D) AP-Octopus-Chip based on the DLD and immunocapture method[87];

## 1.6 SERS detection method

Surface-enhanced Raman scattering (SERS) spectroscopy has been widely applied as optical imaging and detection tool due to the strong signal intensity, excellent photostability, biocompatibility, and especially the multiplexing ability[53]. The SERS phenomenon was first found by Fleischmann in 1974[91]. It was found that rough metal surface can greatly enhance SERS

spectral with enhancement multiple of  $10^3$ - $10^4$ , which is called SERS effect. The discovery of SERS promoted the development of Raman spectral. At present, the total SERS enhancement is considered as the product of the electromagnetic enhancement (EE) and chemical enhancement (CE) mechanisms[92]. The electromagnetic enhancement mechanism is generally received as the dominant contributor to SERS enhancement[93]. The electromagnetic enhancement results from the amplification of the light by excitation of localized surface plasmon resonances (LSPRs). This light concentration occurs preferentially in the gaps, crevices, or sharp features of plasmonic materials, which are traditionally noble and coinage metals with nanoscale features, for examples, silver (Ag), gold (Au), and copper (Cu). The electromagnetic enhancement for SERS is affected by the structure of the supporting plasmonic material, which can reach factors of  $10^{10}$ - $10^{11}$ [94]. The chemical enhancement mechanism primarily involves charge transfer mechanisms, where the excitation wavelength is resonant with the metal-molecule charge transfer electronic state. Theoretically, the chemical enhancement factors can reach  $10^3$ . Some studies found that the magnitudes of enhancement through charge transfer transitions are highly molecule specific[95, 96].

### **1.6.1 Metal-based SERS detection method**

Since the electromagnetic enhancement mechanism is the main contributor to

the Raman signal enhancement, noble metal nanoparticles with plasmonic features have extensively been exploited as SERS platforms mainly due to their simplicity of fabrication[97]. The classic SERS substrates of gold (Au), silver (Ag), or copper (Cu), were widely used in SERS enhancement. Au and Ag are the most widely used as SERS substrate because of their stable properties, while Cu is more reactive. Researchers are striving to optimize substrate structure and configuration to maximize enhancement factors by identify new plasmonic materials and vary shapes and structure of nanoparticles[98, 99]. Various methods have been developed for fabrication of different shapes including nanostars[100, 101], nanoflowers[102, 103], nanorods[104, 105], nanotriangles[106, 107], nanocubes[108, 109], and nanocages[110, 111]. Materials with higher roughness and sharpness could achieve better SERS enhancement. Besides, the dense and enhanced plasmonic hot spots in sharp edges and nanogaps drastically increase the surrounding electrical field, enabling even a single molecule level detection[112]. Based on this phenomenon, advanced SERS substrates have been developed by modifying Au and Ag nanoparticles with coatings resulting in structures such as Au particles-coated nanospheres and SiO<sub>2</sub>-encapsulated Au particles[113]. In general, the SERS enhancement factor of noble-metal nanomaterials can reach 10<sup>12</sup>[114].

### 1.6.2 Semiconductor-based SERS detection method

Since 1950s, semiconductor have been widely applied in microelectronics. The application on SERS activity of semiconductor materials has been further developed, including ZnO nanocrystals[115], ZnO superstructures[116], TiO<sub>2</sub> nanospheres[117], Cu<sub>2</sub>O superparticles[118], W<sub>18</sub>O<sub>49</sub> nanowires[119], Rh<sub>3</sub>S<sub>6</sub> microbowls[120], MoO<sub>2</sub> NPs[121], SnO<sub>2</sub> NPs[122], Nb<sub>2</sub>O<sub>5</sub> NPs[123], Ta<sub>2</sub>O<sub>5</sub> nanorods[124], black TiO<sub>2</sub> nanowires[125] and so on. The enhancement mechanism of the semiconductor SERS effect is mainly attributed to electromagnetic (EM) enhancement and charge-transfer (CT) enhancement[126]. Compared to metal nanomaterials, semiconductor materials have advantages of high spectral stability and reproducibility, strong anti-interference ability, and selective SERS enhancement of target molecules[127]. However, the enhancement factor of semiconductor substrates is relatively low ( $10^3$ - $10^5$ )[128]. To overcome this bottleneck, new enhancement mechanism and novel nanomaterials have been developed, such as crystalline semiconductor-molecule systems, amorphous semiconductor-molecule systems, and crystal-amorphous core-shell semiconductor-molecule systems. Metal oxides are the most used in crystalline semiconductor-molecule systems. For example, Cu<sub>2</sub>O superstructure has been developed for SERS enhancement based on the synergistic effect of chemical enhancement and electromagnetic enhancement, with  $10^{-9}$  M and an EF of  $10^5$ [118]. People found that amorphous structures could enhance semiconductor-molecule interactions and thereby facilitating

interfacial charge-transfer processes, resulting in improved sensitivity of semiconductor-based SERS[129]. The amorphous 2D TiO<sub>2</sub> nanosheets were developed with an ultrahigh EF of  $1.86 \times 10^6$ [130]. By integrating the advantages of both crystalline and amorphous structures, Lin et al. designed a kind of TiO<sub>2</sub> NPs with crystal-amorphous core-shell structure which have remarkable SERS activity in visible and near-infrared regions with an EF of  $4.3 \times 10^5$  [131]. Table 1.2 summarized the previously published results of SERS-active semiconductor nanomaterials.

Table 1.2: SERS performance of previously published SERS-active semiconductor nanomaterials

| Semiconductor                       | Probe Molecule | Enhancement Factor | Limit Of Detection   | Ref.  |
|-------------------------------------|----------------|--------------------|----------------------|-------|
| Cu <sub>2</sub> O<br>Superstructure | R6G            | $8 \times 10^5$    | $6 \times 10^{-9}$ M | [118] |
| Diamond                             | MB             | $3.2 \times 10^5$  | $10^{-7}$            | [132] |
| Zno Nanosheets                      | 4-MBA          | $10^3$ - $10^4$    | $1 \times 10^{-6}$ M | [133] |
| SiO <sub>2</sub> Spheres            | CV             | $10^4$             | -                    | [134] |
| Ag <sub>2</sub> s NPs               | 4-MPY          | $10^2$ - $10^3$    | -                    | [135] |
| TiO <sub>2</sub> Nanosheets         | 4-MBA          | $1.86 \times 10^6$ | -                    | [130] |
| TiO <sub>2</sub> NPs                | 4-NBT          | $4.3 \times 10^5$  | $10^{-6}$ M          | [131] |
| TiO <sub>2</sub> Nanowire           | R6G            | $1.2 \times 10^6$  | $1 \times 10^{-7}$ M | [125] |

### 1.6.3 Application of SERS detection method in biosensing

With the rapid development of novel SERS materials and continuous

improvement of enhancement mechanisms, SERS detection method has been widely applied in biosensing which can be used to detect small molecule, DNA/aptamer, protein/enzyme/peptide/antibody, cellular and in vivo systems.

### **SERS detection of small molecule**

There are several recent research applying SERS for biologically relevant small molecule detection, including the detection of small molecules such as antioxidants (glutathione and glucose), and small molecule markers such as biowarfare agents (anthrax). Zhang et al. designed a silver film over nanosphere (AgFON) substrates for the study of bacillus subtilis spores[136]. As shown in Figure 1.5A, the AgFON substrate can achieve a LOD of  $\sim 2.6 \times 10^3$  spores which is lower than the anthrax infectious dose of  $10^4$  spores, within 11 min procedure. Furthermore, they used atomic layer deposition (ALD) to deposit a sub-1-nm alumina layer on AgFON substrates, which can maintain and stabilize the SERS activity of the underlying silver while present the surface chemistry of the alumina overlayer[137]. In this optimized method, the LOD of bacillus spores reduced to  $\sim 1.4 \times 10^3$  within 10s. Compared to original AgFON substrates, the ALD modified AgFON substrates have twice the sensitivity and 6 times shorter data collection time and 7 times temporal stability. SERS method can also be used to detect glutathione due to the C-S stretching band at  $660 \text{ cm}^{-1}$  shift. Ozaki et al. used Ag to enhance the Raman spectral of glutathione and achieved a glutathione detection range of 100-800

nM with LOD of 50 nM[138]. SERS method can also be used for the detection of many other small molecule, such as oxidized glutathione (GSSG)[139], nicotinic acid adenine dinucleotide phosphate (NAADP)[140], glucose[141], lactate[142], lipids[143] and so on.

### **SERS detection of DNA and aptamer**

SERS detection method can also be employed in DNA and aptamer due to its low LODs and good reproducibility. The common SERS detection method of DNA is to functionalize Au or Ag noble metal NPs with reporter molecule and a single stranded piece of DNA. When the single stranded piece of DNA is hybridized with complementary strand of DNA, the SERS signal of the reporter molecule can be observed[144-146]. Natan et al. reviewed the studies of using multiple SERS tags for the labeling or detection of DNA associated with disease[147]. This review has discussed the different schemes of Au and Ag NPs used as SERS substrate for biomolecule measurement. For example, Barhoumi et al. reported a SERS method for single and double-stranded thiolated DNA oligomer detection by binding DNA oligomers to Au nanoshell-based SERS substrates, as showed in Figure 1.5B[148]. They found that the SERS spectral of DNA oligonucleotides are extremely similar and affected by the Stokes modes of adenine. Besides, they introduced a correlation function analysis which can be used to assess reproducibility and quantify the highly complex changes corresponding to modifications in molecular conformation of

the adsorbate molecules.

### **SERS detection of protein**

SERS detection is also feasible to detect more complicated and larger molecules, such as protein, enzyme, peptide, antibody[149]. Wei et al. used Au nanoshell substrates to study the SERS spectral of three cysteine-containing aromatic peptides, phenylalanine-cysteine, tyrosine-cysteine, and tryptophan-cysteine, with excellent reproducibility[150]. They also obtained the relative Raman and SERS cross-sections of the characteristic Stokes modes of the three aromatic amino acids, which can be used to reproduce the Raman spectral of penetratin. Apart from protein identification, the measurements of protein concentration by SERS method have also been studied. For example, Han et al. developed a novel SERS-based method to probe protein concentrations in a solution by collecting the SERS signal of Coomassie Brilliant Blue dye adsorbed non-specifically to silver colloids to monitor the total protein concentration[151]. In this study, the detection range of protein concentration is  $10^{-5}$ - $10^{-9}$  g/ml with 200 times lower LOD of 1 ng/ml, as showed in Figure 1.5C. This study shows great potential of SERS detection in proteins.

### **Cellular and in vivo SERS detection**

In recent years, applications of SERS detection in cells, tissue and in vivo detection have been widely developed. Stuart et al. first introduced the in vivo

application of SERS which is to measure the glucose concentration of the interstitial fluid. As showed in Figure 1.5D, They functionalized AgFON surfaces with a two-component self-assembled monolayer and subcutaneously implanted it in a rat so that the glucose concentration can be measured by spectroscopically addressing the sensor through an optical window[152]. SERS has also been developed for cancer marker detection in a live cell. Qian et al. reported in vivo tumor targeting and detection based on pegylated gold nanoparticles and SERS[153]. After injecting NPs into the tail vein, SERS spectral obtained from tumor by using targeted nanoparticles can be obviously distinguished from using non-targeted nanoparticles. With a 785 nm laser, SERS tags were over 200 times brighter than NIR-emitting quantum dots. Besides, they could measure SERS spectra at targeted tumor sites up to 2 cm below the skin.

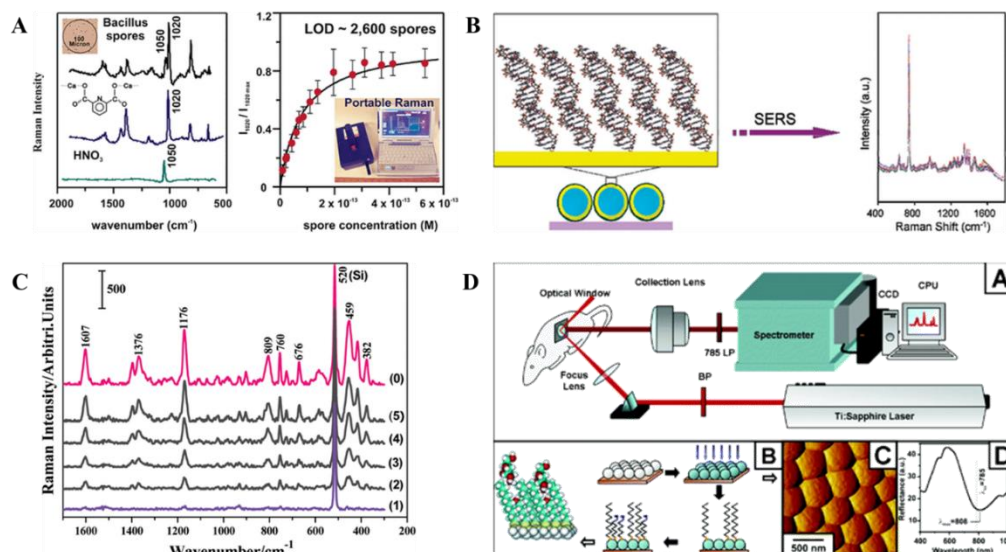


Figure 1.5: Application of SERS detection in biosensing. (A) SERS detection of *Bacillus subtilis* spores on AgFON substrates; (B) SERS detection of single and double-stranded thiolated DNA oligomers; (C) Concentration-dependent SERS spectra of CBBG from  $10^{-5}$ - $10^{-9}$  g/ml (0-5); (D) Schematic of in vivo glucose measurement by SERS.

## 1.7 Gold-iron oxide composite nanoparticles

Composite nanoparticles are composed of different functional components, which have attracted more and more interests of scientists. Composite nanoparticles have great potential applications in the areas of electronics, photonics, catalysis, biotechnology, and nanotechnology[154-157]. Above-mentioned materials generally have core/shell structure or a binary nanostructure. The successful applications of composite nanoparticles were highly depending on nanostructure, components, stability and dispersion of materials under different conditions. Therefore, researchers were focusing on

fabrication of different composite nanoparticles to develop advanced multi-functional materials.

Magnetic composite nanoparticles with specific structure were widely studied in the areas of magnetic fluids, catalysis, data storage, bio-separation, and environmental treatment. To achieve these applications, there were numbers of methods for synthesis of magnetic composites with different components being developed[158-160]. Iron oxide ( $\text{Fe}_3\text{O}_4$  or  $\gamma\text{-Fe}_2\text{O}_3$ ) nanomaterials have typical structure of cubic inverse spinel. Its inherent magnetic feature, nano size, and surface effect could profit to construct magnetic hybrid nanocomposites, which could highly respond to external magnetic field. They could be applied in the capture of targeted substrates, recyclable nanocatalysis, magnetic-photonic purposes, and magnetic resonance imaging[161-163]. Gold nanoparticles were generally used in optical imaging, hyperthermia, and the detection of DNA and proteins[164-167]. By adjusting proximities and shapes of AuNPs, the plasmonic resonance peak of Au could be shifted to the NIR region[168]. Besides, it has been studied that the gold shell layer could provide a strong plasmonic resonant optical response to the nanoparticle. Therefore, the magnetic composites of  $\text{Fe}_x\text{O}_y$  and AuNPs are promising to be with advantages and properties from both individual  $\text{Fe}_x\text{O}_y$  and AuNPs.

### **1.7.1 Structure and synthesis of gold-iron oxide composite nanoparticles**

The structure of gold-iron oxide composite nanoparticles was generally divided into two types: monodispersed composites and aggregate composites. The monodispersed composites attracted more attentions from scientists because of their better reproducibility and reliable characterizations. In the type of monodispersed composites, there were core/satellite structures, core/shell structures, multi-layer composite structures, nano-dumbbells and nanoflowers as shown in Figure 1.6. The core/satellite structures were generally formed by a single core linked with numerous smaller nanoparticles through covalent bonds or supramolecular interaction. The most common example of core/satellite structure was  $\text{Fe}_3\text{O}_4@\text{Au}$ . The  $\text{Fe}_3\text{O}_4$  cores (50-300 nm) were synthesized by solvothermal reactions and the AuNPs (2-20 nm) were synthesized by Au ion reduction reaction. As shown in Figure 2.6A, The  $\text{Fe}_3\text{O}_4$  cores were covered by a  $\text{SiO}_2$  shell (3-50 nm thickness) by sol-gel reaction and functionalized with ammonium groups so that  $\text{Fe}_3\text{O}_4@\text{SiO}_2$  NPs could be positively charged. After that, the negatively charged AuNPs could be attached onto positively charged  $\text{Fe}_3\text{O}_4@ \text{SiO}_2$  NPs by electrostatic interactions, forming  $\text{Fe}_3\text{O}_4@\text{SiO}_2@\text{Au}$  core/shell/satellite structure nanocomposites.

Gold-iron oxide composite nanoparticles could be functionalized with antibodies so that they could be used to target specific cancer cells. There were three common ways for functionalization: direct attachment or ligand place exchange of proteins or antibodies through Au-S interactions based on cysteine

residual thiol groups[169-171]; coupling reactions by formation of amide of antibodies or respective proteins[172, 173]; supramolecular interactions of biotinylated antibodies with streptavidin-functionalized nanocomposites[174]. Compared to single nanoparticles, the composite nanoparticles have higher surface which could load more ligands and thus improve performance.

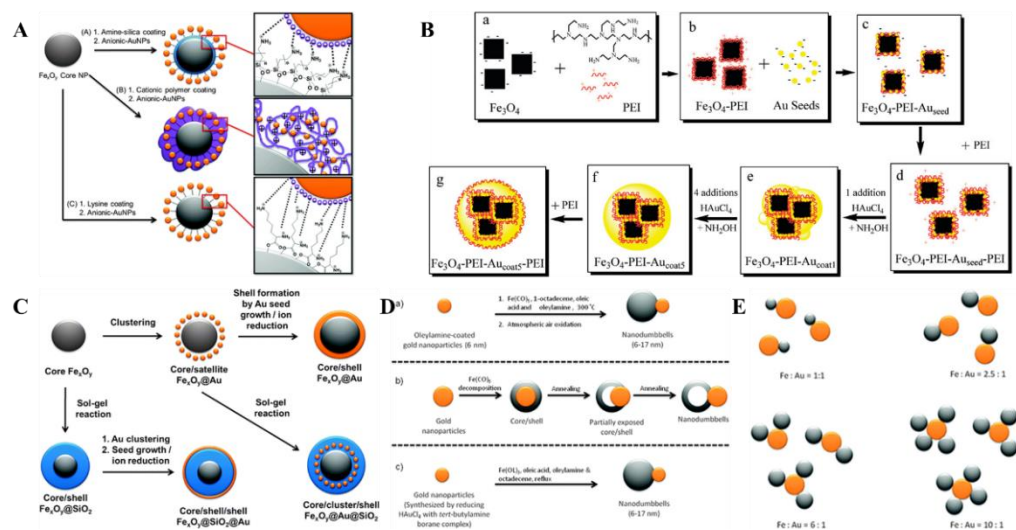


Figure 1.6: Schematic representation of gold-iron oxide composite nanoparticles. A)  $\text{Fe}_x\text{O}_y@Au$  core/satellite structures[175], B)  $\text{Fe}_x\text{O}_y@Au$  core/shell structures[176], C) multi-layer  $\text{Fe}_x\text{O}_y@Au$  composites[175], D) Au- $\text{Fe}_x\text{O}_y$  dumbbell nanocomposites[175], E) gradual change from Au- $\text{Fe}_x\text{O}_y$  nano-dumbbells to nanoflowers[175].

### 1.7.2 Applications of gold-iron oxide composite nanoparticles in cell sorting and separation

Gold-iron oxide composite nanoparticles have a wide range of applications including magnetic resonance imaging[177], computed tomography[178],

fluorescent optical imaging[179, 180], magnetic-induced hyperthermia[181], photo-induced hyperthermia[174, 182], drug delivery[179], DNA sensor[183], immunosensor[184, 185], enzyme-based sensor[186], cell sorting[187], and catalysis[188-190]. Among these applications, Magnetic separation and enrichment has become the most commonly used methods for biomarker-purification, separation and cell sorting. Nash et al. designed a thermally responsive copolymer for coating  $\text{Fe}_3\text{O}_4$  nanoparticles and model biomarker modified Au nanoparticles[191]. The polymer directed the formation of the Au- $\text{Fe}_3\text{O}_4$  aggregates that could be separated efficiently with a magnet. This method could be used for pulling down the biomarker from the human plasma in rapid diagnostic strategies. Wang and Irudayaraj designed two hybrid  $\text{Fe}_3\text{O}_4$ -Aurod- $\text{Fe}_3\text{O}_4$  nanodumbbells and  $\text{Fe}_3\text{O}_4$ -Aurod necklace-like structures with tunable optical and magnetic properties[187]. The  $\text{Fe}_3\text{O}_4$ -Aurod necklace's surface could be conjugated with antibodies relevant to multiple pathogens. This probe could be used for optical detection of specific pathogens. Moreover, due to the magnetization and NIR absorption possessed by this nanocomposite, the target bacteria (*E. coli* and *S. typhimurium*) could be separated by the antibody conjugated  $\text{Fe}_3\text{O}_4$ -Aurod necklace under magnetic field, and after absorbing sufficient energy from the NIR laser, the nanocomposite was phototoxic to the specific target pathogen in the mixture.

Liu et al. employed  $\text{Fe}_3\text{O}_4$ @Au core/shell nanocomposites for the application

of purifying CD4<sup>+</sup> lymphocytes from the spleen of mice[192]. Streptavidin-FITC was conjugated onto the surface of Fe<sub>3</sub>O<sub>4</sub>@Au core/shell nanocomposites. For the strong noncovalent binding between streptavidin and biotin, these modified nanocomposites could bind to the biotinlabeled anti-CD4<sup>+</sup> antibody, which could also specifically bind to CD4<sup>+</sup> lymphocytes. It was noted that Fe<sub>3</sub>O<sub>4</sub>@Au core/shell nanocomposites could successfully pull down CD4<sup>+</sup> T lymphocytes from the whole splenocytes by magnetic separation.

Yu et al. reported the synthesis of poly (diallyldimethylammonium chloride)-coated Fe<sub>3</sub>O<sub>4</sub> (PDDA-Fe<sub>3</sub>O<sub>4</sub>) nanoparticles by the coprecipitation method[193]. Negatively charged citrate-capped Au nanoparticles could be effectively self-assembled onto the surface of cationic PDDA-Fe<sub>3</sub>O<sub>4</sub>nanoparticles. The Au-Fe<sub>3</sub>O<sub>4</sub>-PDDA aggregated nanocomposites revealed the capability of selectively enriching cysteine-containing peptides (cytochrome c) through the formation of Au-S bonds. The noncysteine-containing peptides could not be extracted by the same nanocomposites.

In recent decades, aromatic boronic acid derivatives have been employed in the construction of receptors for saccharides. Boronic acids form covalent bonds with cis-diol structures, which are present in most sugar moieties, to generate five- or six-membered cyclic esters in nonaqueous or basic aqueous media.

## 1.8 Black titanium dioxide

TiO<sub>2</sub> is known as the quintessential prototype photocatalyst. However, an obvious drawback of the different pure TiO<sub>2</sub> phases is a wide bandgap of 3-3.4 eV that limits the absorption of solar energy to only a few percent in the UV region. Since photocatalytic absorption is localized at the surface, surface modification appears as the direct route for both engineering the band gap and enhancing the photoactivity[194, 195]. The ideal surface modification would alter the surface of single crystal TiO<sub>2</sub> such that it absorbs the entire spectrum of solar irradiation from the infrared to the UV. Intuitively, the most efficient light-harvesting photocatalyst appears black to naked eye. Black TiO<sub>2</sub> first reported by Chen et al. in 2011 is a nanomaterial that was created by surface modification and distinguished by its black color[196]. This type of black TiO<sub>2</sub> is produced by H<sub>2</sub> reduction of white crystalline TiO<sub>2</sub>, exhibiting a narrow band gap and enhanced photoactivity attributed to surface disorder. It has been widely applied in biomedicine. Ren et al. first reported hydrogenated black TiO<sub>2</sub> (H-TiO<sub>2</sub>) NPs with near infrared absorption explored as photothermal agent for cancer photothermal therapy to circumvent the obstacle of ultraviolet light excitation[197]. To overcome the low drug loading ability, limited tissue penetration of UV light, and heating effect of 980 nm NIR on normal tissue, Ren et al. designed novel mesoporous silica (mSiO<sub>2</sub>) coated black TiO<sub>2</sub> core-shell nanocomposites are designed and constructed as doxorubicin carriers for

808 nm NIR triggered thermal imaging guided photothermal therapy combined chemotherapy of breast cancer. Properties of the nanocomposites such as micro-morphology, size, drug loading ability and release, targeting performance, and therapy efficiency in vitro and in vivo were evaluated[198]. As well as therapy applications, black TiO<sub>2</sub> was studied for tumor diagnosis. Lin et al. successfully designed crystal-amorphous core-shell-structured TiO<sub>2</sub> NPs, the black TiO<sub>2</sub> NPs exhibited remarkable SERS activity in visible and near-infrared regions, and the EF value can be up to  $4.3 \times 10^5$ . The efficient interfacial PICT can be attributed to the strong synergistic effect of the novel crystal-amorphous core-shell structure of B-TiO<sub>2</sub> NPs. The high-efficiency exciton transition of crystal core provides sufficient photoinduced charges. Furthermore, the interfacial band bending at the crystal-amorphous heterojunction enables effective exciton separation and charge injection, resulting in the enrichment of photoinduced charges in the amorphous shell to facilitate the interfacial PICT between the substrate and target molecules. Low Fermi level and high electronic density of states (DOSs) of the amorphous structure enable strong vibronic coupling in amorphous shell-molecule system. These properties are confirmed by the density function theory (DFT) calculations and Kelvin probe force microscopy (KPFM). In addition, the small band gap, high binding energy, and abundant surface defect states of B-TiO<sub>2</sub> are leveraged to form a stable complex and boost PICT resonance in the substrate-molecule system. Significantly, the remarkable SERS sensitivity

endows B-TiO<sub>2</sub> NPs with the capability of cancer cell diagnosis.

### **1.9 Research gap**

Based on the literature review, larger numbers of technologies have been developed for CTC detection. However, there are some limitations in current technology requiring for improvements. As mentioned above, microfluidic technology could isolate CTCs from blood cells depending on the difference between CTCs and blood cells. The performance of label-dependent methods highly depends on expression level of biomarkers on CTCs and interaction between CTCs and biomarker-coated surface. Besides, excessive binding of CTCs and specific bio-probe might change origin structure of cells which would affect downstream analysis of CTCs and increase detection cost. The label-independent method has the main advantage of isolating CTCs from blood without any expression of tumor-specific markers. However, it is limited by low purity and specificity because of overlap existed in some physical properties between CTCs and blood cells. After isolation, there are still tens of thousands of WBCs remaining, which would disturb the accuracy and sensitivity of CTC detection and require further identification of CTCs. The commonly used way to identify CTCs is fluorescent immunolabeling by characterizing the surface protein expression of CTCs. However, when using multiple fluorophore-conjugated antibodies, the broadness of fluorescence spectrum and the cross-talking of fluorescent tags often confound the results.

Besides, the background noise was magnified in a microfluidic system, which might cause misrecognition of CTCs. SERS method has been widely applied in single cell analysis. However, excessive or unstable noble metal-based SERS biological probes would cause agglomeration and thereby cause hotspot effect leading to false positive. Therefore, it is necessary to develop a novel downstream analysis strategy of CTCs combined with microfluidic method.

### **1.10 Outline of the thesis**

Refer to the research gap, microfluidic method was selected to isolate CTCs and SERS method was used for downstream analysis of CTCs. Three strategies have been adopted for CTC detection in clinical blood samples. In the first strategy, gold-iron oxide composite nanoparticles were selected as SERS substrate. SPION@Au-MBA-rBSA-FA SERS biological probes were reproduced according to the previous work. In this thesis, SPION@Au-MBA-rBSA-FA SERS biological probes were applied into clinical blood sample detection. 32 blood samples from cancer patients and 3 blood samples from healthy people have been detected. In the second strategy, black B-TiO<sub>2</sub> NPs were used as SERS substrate due to its low cost, high spectral stability and reproducibility, strong anti-interference ability, and selective SERS enhancement of target molecules. The B-TiO<sub>2</sub>-AR-PEG-FA biological probe consisted of four layers. The innermost layer was B-TiO<sub>2</sub> nanoparticles with crystal core and amorphous shell structure. The second layer was alizarin red

(AR) molecule which was responsible for providing Raman spectral signal. The third layer was a thin NH<sub>2</sub>-PEG2000-COOH layer which was used to improve the dispersion of biological probes and to provide binding sites of folic acid (FA) and thus increase grafting rate of FA. The outermost layer was FA molecule. FA was used to specifically recognize cancer cells by folate receptor (FR) on cell membrane. The experiment results showed that this B-TiO<sub>2</sub> based SRES biological probe has good specificity and accuracy with obvious Raman signal. It can distinguish folate receptor-expressing cancer cells (MCF-7) from low folate receptor-expressing cells (A549 and Raw264.7). In the third strategy, microfluidic method was added to isolate CTCs before SERS detection. In this strategy, the relatively low specificity and isolation purity of microfilter could be solved by integrating with high-sensitivity SERS spectra detection, while the microfilter could reduce interference of blood background during SERS detection. Besides, SERS-fluorescence dual-modal in situ imaging method proved that this strategy has high specificity of detection with detection limit of 2 cancer cells per milliliter in rabbit blood. Besides, the operation process was simple and high-speed, with detection time less than 1.5 hours. These results illustrates that both of microfluidic isolation and SERS detection could open new paths for liquid biopsy.

The thesis was divided into six chapter to show the details of research. The first chapter introduced cancer background and gave the literature review of CTC

detection. It has reviewed the importance of CTC detection for cancer, CTC properties and clinical applications of CTCs. CTC detection was divided into two parts: isolation and downstream analysis of CTCs. Microfluidic technologies for CTC isolation have been reviewed, which have been classified into label-dependent method, label-independent method, and integrated method. SERS detection method has been considered for downstream analysis of CTCs. Both metal-based and semiconductor-based SERS substrate has been reviewed. gold-iron oxide composite nanoparticles and black titanium have been introduced as SERS substrates. The second chapter described the methodology used in research: synthesis of SPION-PEI@AuNPs-based SERS biological probe and application on CTC detection, synthesis of B-TiO<sub>2</sub>-based SERS biological probe and application on CTC detection, and combination method of microfilter and B-TiO<sub>2</sub>-based SERS biological probe on CTC detection. The methodology also contained cell culture, treatment of blood samples and materials and equipment for research. The third to fifth chapters were the experimental results and discussion. The fourth chapter was the characterization and application of SPION@Au-MBA-rBSA-FA SERS biological probes. SPION-PEI@Au were successfully synthesized according to the previous work of the research group. 32 clinical blood samples of cancer tumor and 3 clinical blood samples of healthy people were detected by SPION@Au-MBA-rBSA-FA SERS biological probes. The fifth chapter showed the experiment results of B-TiO<sub>2</sub>-based SERS biological probe. The

synthesized B-TiO<sub>2</sub> showed good SERS enhancement effect and the LOD of the AR molecule on B-TiO<sub>2</sub> can reach  $5 \times 10^{-8}$  M. The experiment results showed that this B-TiO<sub>2</sub> based SRES biological probe has good specificity and detection accuracy with obvious Raman signal. It can distinguish folate receptor-expressing cancer cells (MCF-7) from low folate receptor-expressing cells (A549 and Raw264.7). In the sixth chapter, microfluidic method was added to isolate CTCs before SERS detection. In this strategy, the relatively low specificity and isolation purity of microfilter has been solved by integrating with high-sensitivity SERS spectra detection, while the microfilter could reduce the interference of blood background to SERS detection. Besides, SERS-fluorescence dual-modal in situ imaging method proved that this strategy has high specificity of detection with detection limit of 2 cancer cells per milliliter in rabbit blood. Besides, the operation process was simple and high-speed, with detection time less than 1.5 hours. The sixth chapter contained conclusion of this research and perspective of microfluidic method and SERS detection method.

## **Chapter 2 Methodologies**

### **2.1 Introduction**

This chapter has described the methodology of three research. Materials and equipment used for each research have been introduced. The first research was about synthesis of SPION-PEI@AuNPs-based SERS biological probe and application on CTC detection. The specificity in cells and the sensitivity and separation performance in blood of this biological probe have been tested. The traditional way for CTC separation was the combination of density gradient centrifugation and magnetic separation. The second research was about synthesis of B-TiO<sub>2</sub>-based SERS biological probe and application on CTC detection. In this section, the SERS enhancement effect of B-TiO<sub>2</sub> was studied. The stability, specificity, and sensitivity of B-TiO<sub>2</sub> based biological probe was tested in the mixed cell suspension. The third research was about the study of combination method of microfilter and B-TiO<sub>2</sub>-based SERS biological probe on CTC detection. The performance of B-TiO<sub>2</sub> based biological probe has been tested in the second research. In this section, numeric simulation has been performed to compare the flow dynamics of WBC clearance when flowing through the microfilter with different flow rate at range of 0.1–0.9 mL/min using simplified geometry and boundary conditions by ANSYS Fluent software. The purpose of simulation was to find a proper flow rate to avoid plugging of microfilter and cell damaging. Furthermore, sensitivity, specificity, and capture assay of this method have been tested both in mixed cells and blood.

## **2.2 Synthesis of SPION-PEI@AuNPs-based SERS biological probe and application on CTC detection**

### **2.2.1 Materials and equipment**

**Materials:** Ethylene glycol ( $C_2H_6O_2$ ), sodium acetate anhydrous ( $C_2H_3NaO_2$ ), sodium borohydride ( $NaBH_4$ ), folic acid ( $C_{19}H_{19}N_7O_6$ ), albumin from bovine serum (BSA), 1-ethyl-3-[3-(dimethylamino)propyl] carbodiimide hydrochloride (EDC·HCl) as well as N-hydroxysuccinimide (NHS) were ordered from Aladdin Reagent Co. Ltd., Shanghai, China. Iron chloride hexahydrate ( $FeCl_3 \cdot 6H_2O$ ) was purchased from Alfa Aesar. Tetrachloroauric (III) acid tetrahydrate ( $HAuCl_4 \cdot 4H_2O$ ), trisodium citrate dehydrate ( $C_6H_5Na_3O_7 \cdot 2H_2O$ ) and Hoechst were purchased from Sinopharm Chemical Reagent Co. Ltd., Shanghai, China. 4-mercaptobenzoic acid (MBA), polyethylenimine ( $M_w \sim 25000$ ), DMSO and MTT was ordered from Sigma-Aldrich. Lymphocyte isolation was ordered from Slolarbio Life Science Co. Ltd., Beijing, China. Fetal bovine serum (FBS), incomplete DMEM (high glucose) as well as trypsin11 EDTA were ordered from KeyGen BioTech. Anti-CD45 antibody [F10-89-4] (Alexa Fluor® 488) Alexa and Anti-Cytokeratin 8 antibody [EP1628Y] (Alexa Fluor® 647) were purchased from Abcam, Zhejiang, China.

**Equipment:** The photos of the equipment was shown in Figure 3.1. The

nanoparticles were characterized by transmission electron microscopy (TEM, JEOL. 2100, Tokyo, Japan). The Raman spectra were observed on a confocal microprobe Raman system (Renishaw inVia Reflex, Wolton-under-Edge, U.K.). The laser wavelength was fixed at 785 nm. The time of data acquisition was set to 3.0 s, and the laser power was 280 mW. The SERS spectra were observed from liquid samples with homogeneous SERS hotspot. The zeta distribution of the nanoparticles was measured at room temperature by dynamic light scattering (DLS) using a zeta particle size analyzer (Malvern, England).



Figure 2.1: The photos of the equipment A) Transmission electron microscopy (TEM, JEOL. 2100, Tokyo, Japan); B) Confocal microprobe Raman system (Renishaw inVia Reflex, Wolton-under-Edge, U.K.); C) Zeta particle size analyzer (Malvern, England).

### **2.2.2 Synthesis of SPION-PEI@AuNPs-based SERS biological probe**

#### **Preparation of SPION-PEI**

First, 0.68g  $\text{FeCl}_3 \cdot 6\text{H}_2\text{O}$  was weighed by electronic balance and dispersed into 20 mL Ethylene Glycol by ultrasonic vibration method. Second, 1.8g NaAc was added into the above mixed solution. The solution was mixed uniformly

by magnetic stirring device. Then, 0.75 g PEI was added into the previous solution. After stirring and heating at 60 °C for 20 minutes, the mixed solution was transferred to reaction kettle and heated at 220 °C for 2 hours by baking oven. After reaction and cooling to room temperature, the reaction product was washed several times by deionized water and alcohol and dispersed in 100 mL deionized water. After centrifugation at 1000 rpm for 5 minutes, the supernatant was collected and reserved at 4 °C.

### **Preparation of AuNPs**

50 mL of 1 mM HAuCl<sub>4</sub> aqueous solution was heated at 165 °C with magnetic stirring. After boiling, 2.256 mL of 1.0% Na<sub>3</sub>Ct aqueous solution was added into the boiling solution rapidly. After the color of solution changing to purplish red, the solution was further heated for 3 minutes and then cooling at room temperature. After cooling, the AuNPs dispersion was reserved at 4 °C.

### **Preparation of SPION-PEI@AuNPs**

First, 900 μL of SPION-PEI was added dropwise into 3 mL AuNPs solution. Next, the mixed solution was transferred to shaking table and oscillated at 200 rpm for 20 minutes at room temperature. After that, the obtained product was washed repeatedly with deionized water by magnet separation. The final SPION-PEI@AuNPs were dispersed in 4 mL deionized water and kept at 4 °C fridge.

### **Preparation of rBSA-FA**

First, 50 mg FA was weighed and dissolved in 50 mL PBS solution (10mM, pH 7.4). After complete dissolution, 40 mg EDC and 24 mg NHS were added into the primary solution stirring at room temperature for 8 hours. After that, the activated FA was achieved. Second, 0.378 g NaBH<sub>4</sub> and 0.4 g BSA were dissolved in 10 mL and 20 mL deionized water respectively. 260 μL NaBH<sub>4</sub> was added into 20 mL BSA solution and stirred for 1 hour to reduce BSA. After that, 5 mL reduced BSA (rBSA) was added into 50 mL activated FA and stirred for 8 hours. The obtained solution was added into ultrafiltration centrifuge tube and centrifuged at 6000 rpm for 30 minutes. The obtained rBSA-FA was dispersed at deionized water and saved at -20°C fridge.

### **Preparation of SPION-PEI@AuNPs-4MBA-rBSA-FA**

The synthesis process of SPION-PEI@AuNPs-4MBA-rBSA-FA was shown in Figure 2.2. 0.000616g MBA was weighed and dissolved in 2 mL ethanol. The above MBA solution was diluted to  $2 \times 10^{-5}$  M. 4 mL MBA solution was added dropwise into 4mL SPION-PEI@AuNPs solution. The primary solution was transferred to shaking table and shock at 200 rpm for 5 minutes at room temperature. After shaking, the product was magnetic washed by PBS solution several times and centrifugated at 1000 rpm for 5 minutes. After centrifugation, the supernatant was collected for further use.

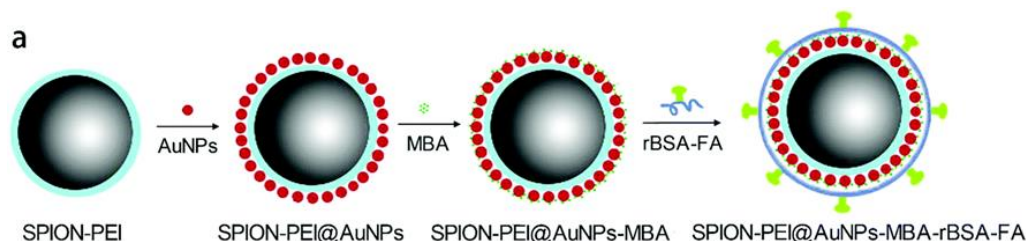


Figure 2.2: Chemistry synthesis process of SERS SPION-PEI@AuNPs-4MBA-rBSA-FA biological probe[199].

### 2.2.3 Cell culture

MCF-7 is a human breast cancer cell line and A549 is a human non-small cell lung carcinoma cell lines, which are bought from Shanghai Institutes for Biological Sciences (SIBS). Hela is a human cervical cancer cell line supported by General Hospital of Eastern Theater Command. All the cells were cultured in complete culture medium (90% DMEM, 10% FBS) under standard cell culture condition (5% CO<sub>2</sub>, 37 °C). For experiments, cells were detached by 0.25% trypsin solution and resuspended in PBS solution.

### 2.2.4 Specificity of SPION-PEI@AuNPs-based SERS biological probe in cells

To verify the SERS performance of SPION-PEI@AuNPs-based SERS biological probe on the cell membranes and the ability to specifically recognize the FR on the cancer cell membranes, two cancer cell lines of MCF-7 and A549 were selected as models and detected by Raman instrument. First, MCF-

7 and A549 were separately incubated with PBS solution, SPION-PEI@AuNPs-MBA-rBSA-FA biological probe and PEI@AuNPs-MBA biological probe for 1 hour and washed by PBS for three times. After that, the Raman instrument was used to observe the optical image and corresponding SERS mapping image of cells, at 785 nm laser.

### **2.2.5 Sensitivity and separation of SPION-PEI@AuNPs-Based SERS biological probe in blood**

Animal experiments in this study were all carried out according to the protocols approved by the animal care and use committee of the Ningbo University. The blood samples were drawn from rabbit ears and then injected into vacutainer tubes, which contained lithium heparin. MCF-7 cell line was spiked into rabbit blood at 0-500 cells/mL concentration. The blood samples were then separated by density gradient centrifugation. 2 mL blood sample was first diluted by adding 2 mL PBS solution. Next, the blood solution was slowly added to 2 mL lymphocyte separation solution. After centrifugation at 1500 rpm for 25 minutes, the sample was separated into four layers (from top to bottom: plasma, mononuclear cells, lymphocyte separation solution, red blood cells). The layer of mononuclear cells was collected and washed twice with PBS solution by centrifugation at 1000 rpm for 5 minutes. After washing, 200  $\mu$ L SERS biological probes were added into collected cells and incubated for 1 hour. After incubation, the excess biological probes were cleaned away by

centrifugation at 1000 rpm for 5 minutes. Then, the samples were rinsed thrice with 200  $\mu$ L PBS solution via magnetic separation and measured by confocal Raman microscopy.

### **2.2.6 Application in clinical tumor blood detection**

To explore the clinical utility of SERS biological probe, blood samples from 32 cancer patients and 3 healthy people were detected. The blood samples were then separated by density gradient centrifugation. The pretreatment of blood was same as Section 2.2.5. 2 mL blood sample was first diluted by adding 2 mL PBS solution. After centrifugation, CTCs were collected by SERS biological probe and separated by magnetic separation. Then, the samples were rinsed thrice with 200  $\mu$ L PBS solution and measured by confocal Raman microscopy at 785 nm laser.

## **2.3 Synthesis of B-TiO<sub>2</sub>-based SERS biological probe and application on CTC detection**

### **2.3.1 Materials and equipment**

**Materials:** Titanium(IV) oxide (P25) was purchased from Acros Organics; Sodium borohydride (NaBH<sub>4</sub>), Alizarin red, NH<sub>2</sub>-PEG2000-COOH (95%), Folic acid ( $\geq$ 98%), N-hydroxysuccinimide (NHS), 1-ethyl-3-(3-(dimethylamino)propyl) carbodiimide (EDC), Fluorescein isothiocyanate (FITC), FITC-PEG2000-FA were purchased from Aladdin, Shanghai, China;

Tris-HCl buffer (1.0 M, pH 8.5) was purchased from Macklin, Shanghai, China; Dialysis bag (50kD) was purchased from Yuanye, Shanghai, China; FITC linked polyclonal rabbit antibody to FA was purchased from Cloud Clone Corp, USA; Alexa Fluor® 647 Anti-Cytokeratin 8 antibody (CK8) and Alexa Fluor® 488 Anti-CD45 antibody (CD45) were purchased from Abcam, Shanghai, China; Hoechst was purchased from Sinopharm Chemical Reagent Co., Ltd.

**Equipment:** The photos of the equipment were shown in Figure 3.3. The transmission electron microscopy (TEM) and high-resolution transmission electron microscopy (HRTEM) images of the B-TiO<sub>2</sub> samples were obtained by Talos F200x. The powder X-ray diffraction (XRD) of the B-TiO<sub>2</sub> samples were characterized by the BRUKER D8 ADVANCE DAVINCI diffractometer with Cu K $\alpha$  radiation ( $\lambda = 1.54056 \text{ \AA}$ ). Raman spectra was collected by Renishaw inVia Reflex instrument with 532 nm laser. The fluorescence images were obtained by laser confocal fluorescence microscopy (LEICA, TCS SP5).

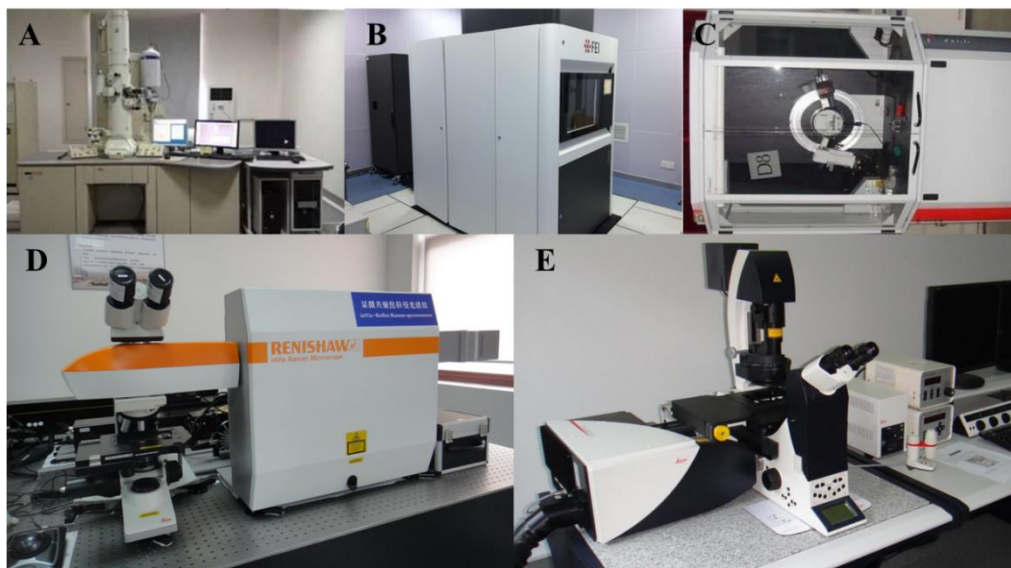


Figure 2.3: The photos of the equipment A) Transmission electron microscopy (TEM, JEOL. 2100, Tokyo, Japan); B) High-resolution transmission electron microscopy (HRTEM, Talos F200x); C) X-ray diffraction (XRD, D8 ADVANCE); D) Confocal microprobe Raman system (Renishaw inVia Reflex, Wolton-under-Edge, U.K.); E) Biological laser confocal fluorescence microscopy (LEICA, TCS SP5).

### 2.3.2 Synthesis of B-TiO<sub>2</sub>-based SERS biological probe

#### Fabrication of B-TiO<sub>2</sub> NPs

B-TiO<sub>2</sub> was fabricated according to the literature [200]. At room temperature with dry condition, the mixture of 1.5 g P25 and 1.5 g NaBH<sub>4</sub> was ground for 30 minutes. Then the mixture was transferred to porcelain boat and placed into tube furnace. The heating process started from room temperature to 350 °C at a heating rate of 10 °C per minute and kept at 350 °C for 4 hours with protection of argon. After natural cooling, the obtained product was washed by water and

ethanol three times and dried at 70 °C. Finally, B-TiO<sub>2</sub> NPs was obtained.

### Synthesis of SERS biological probe

The SERS biological probe consisted of four parts as shown in Figure 3.4, a crystal-amorphous core-shell B-TiO<sub>2</sub> as a core structure, Raman reporter AR molecule absorbed on B-TiO<sub>2</sub>, a thin NH<sub>2</sub>-PEG2000-COOH layer to protect B-TiO<sub>2</sub>-AR and to improve the dispersion of biological probe, and FA to specifically recognize folate receptor on cancer cell membrane. First, 5 mL AR solution (10<sup>-2</sup>M) was mixed with 5 mL 1 mg/mL B-TiO<sub>2</sub> by stirring for 4 hours and centrifugating 3 times at 10000 rpm. AR molecule was absorbed onto B-TiO<sub>2</sub> by chemical bonding[201].

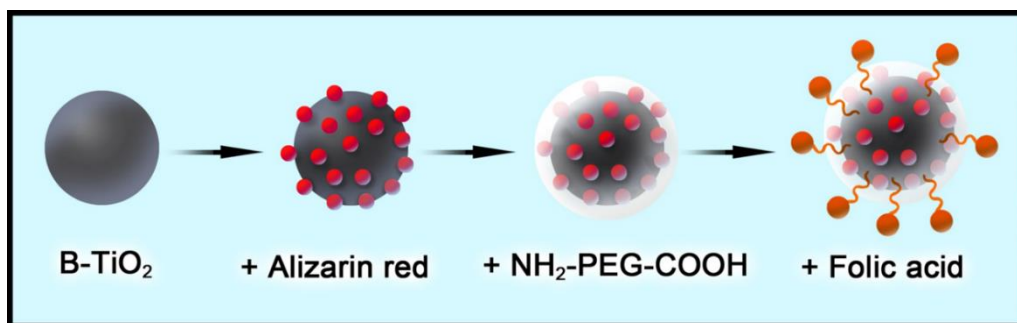


Figure 2.4: Chemistry synthesis process of B-TiO<sub>2</sub> based biological probe

The obtained B-TiO<sub>2</sub>-AR was dispersed in 50 mL 10 mM Tris-HCl buffer (pH 8.5). Then, B-TiO<sub>2</sub> -AR-PEG was obtained by adding 10 mg NH<sub>2</sub>-PEG2000-COOH into the above solution, stirring for 4 hours and centrifugated 3 times at 10000 rpm.

FA was first activated by NHS and EDC in phosphate buffer saline (PBS, pH 7.4). First, 50 mg FA was fully dissolved in 50 mL PBS. Then, 40 mg EDC and 24 mg NHS were added into FA solution stirring for 4 hours at room temperature. After that, the activated FA was mixed with B-TiO<sub>2</sub>-AR-PEG solution stirring for 12 hours at room temperature. B-TiO<sub>2</sub>-AR-PEG was modified with FA by the amide interaction between the carboxyl group of FA and amino group of NH<sub>2</sub>-PEG2000-COOH. Finally, the B-TiO<sub>2</sub>-AR-PEG-FA was collected and washed by dialysis bag (50 kD) for 36 hours to remove the excess FA. The obtained B-TiO<sub>2</sub>-AR-PEG-FA biological probe was dispersed into PBS solution and saved in 4 °C fridge.

### **2.3.3 Cell culture**

MCF-7 is a human breast cancer cell line. A549 is a human non-small cell lung carcinoma cell line. Raw264.7 is a mouse monocyte macrophage leukemia cell line. These three cell lines are bought from Shanghai Institutes for Biological Sciences (SIBS). All the cells were cultured in complete culture medium (90% DMEM, 10% FBS) under standard cell culture condition (5% CO<sub>2</sub>, 37 °C). For experiments, cells were detached by 0.25% trypsin solution and resuspended in PBS solution.

### **2.3.4 FR expression screening of MCF-7, A549 and Raw264.7 cell lines**

The three cell lines were incubated in a 6-well plate with same cell concentration. Each cell line was divided into two wells. The same amount of FITC-PEG2000-FA was added into one well of each cell line respectively and incubated for 30 mins. Then the cells were washed by PBS solution and analyzed by flow cytometry.

### **2.3.5 FA modification of SERS biological probe**

To verify the FA modification, two methods were utilized. For the first one, the conjugation efficiency of FA on the SERS biological probe was calculated by a previous mass balance method[202]. After the activated FA mixed with B-TiO<sub>2</sub>-AR-PEG stirring for 12 hours, the resulting B-TiO<sub>2</sub>-AR-PEG-FA was obtained by centrifugation at 10000 rpm for 10 minutes. The supernatant was collected, and the residual FA content was determined using the calibration curve of FA standard solutions by measuring the UV-vis absorption. For the second one, a FITC linked polyclonal rabbit antibody to FA was used to simulate the FA receptors on the cell membranes. It was incubated with FA modified SERS biological probe and non-FA modified SERS biological probe for 3 hours, separately. Then, after washing by PBS buffer for three times, the FA modified SERS biological probe and non-FA modified SERS biological probe were observed by fluorescence microscopy gel image system.

### **2.3.6 Specificity and sensitivity of B-TiO<sub>2</sub>-based SERS biological probe in**

### **the mixed cells**

To verify the SERS performance of B-TiO<sub>2</sub> SERS biological probe on the cell membranes and the ability to specifically recognize the FR on the cancer cell membranes, two cancer cell lines of MCF-7 and A549 were selected as models and detected by Raman instrument. First, MCF-7 and A549 were separately incubated with PBS solution, B-TiO<sub>2</sub>-AR-PEG-FA biological probe and B-TiO<sub>2</sub>-AR-PEG biological probe for 1 hour and washed by PBS for three times. After that, the Raman instrument was used to observe the optical image and corresponding SERS mapping image of cells. Second, after incubated with B-TiO<sub>2</sub>-AR-PEG-FA biological probe, MCF-7 and A549 were stained by FITC and Hoechst and observed by confocal fluorescence microscopy. Besides, AR can produce its characteristic fluorescence with its excitation and emission wavelength at 530 nm and 560 nm, respectively.

To verify the ability of B-TiO<sub>2</sub>-AR-PEG-FA biological probe to remove interference from FR negative cells, two cell lines of MCF-7 and Raw264.7 were mixed and incubated with B-TiO<sub>2</sub>-AR-PEG-FA biological probe for 1 hour and washed by PBS for three times. After that, the mixed cells were stained with Hoechst (blue, MCF-7 positive, Raw264.7 positive), CK8 (red, MCF-7 positive, Raw264.7 negative) and observed by confocal fluorescence microscopy.

To test the sensitivity of biological probe, 200  $\mu\text{L}$  B-TiO<sub>2</sub>-AR-PEG-FA biological probe was mixed with 1.0 mL cell suspension of MCF-7 with concentration of 1-100 cells per milliliter. After incubation for 1 hour, the excess biological probes were cleaned away by centrifugation at 1000 rpm for 5 minutes. The precipitate was collected and dispersed evenly in 200  $\mu\text{L}$  PBS solution for the measurement of confocal Raman microscopy.

## **2.4 Combination method of microfilter and B-TiO<sub>2</sub>-based SERS biological probe on CTC detection**

### **2.4.1 Materials and equipment**

**Materials:** Titanium(IV) oxide (P25) was purchased from Acros Organics; Sodium borohydride (NaBH<sub>4</sub>), Alizarin red, NH<sub>2</sub>-PEG2000-COOH (95%), Folic acid ( $\geq 98\%$ ), N-hydroxysuccinimide (NHS), 1-ethyl-3-(3-(dimethylamino)propyl) carbodiimide (EDC), Fluorescein isothiocyanate (FITC), FITC-PEG2000-FA were purchased from Aladdin, Shanghai, China; Tris-HCl buffer (1.0 M, pH 8.5) was purchased from Macklin, Shanghai, China; Dialysis bag (50kD) was purchased from Yuanye, Shanghai, China; FITC linked polyclonal rabbit antibody to FA was purchased from Cloud Clone Corp, USA; Alexa Fluor® 647 Anti-Cytokeratin 8 antibody (CK8) and Alexa Fluor® 488 Anti-CD45 antibody (CD45) were purchased from Abcam, Shanghai, China; Hoechst was purchased from Sinopharm Chemical Reagent Co., Ltd.; Microfilter, PL01 was purchased from Anfang Biotechnology, Guangzhou,

China.

**Equipment:** The photos of equipment were shown in Figure 3.3. The transmission electron microscopy (TEM) and high-resolution transmission electron microscopy (HRTEM) images of the B-TiO<sub>2</sub> samples were obtained by Talos F200x. The powder X-ray diffraction (XRD) of the B-TiO<sub>2</sub> samples were characterized by the BRUKER D8 ADVANCE DAVINCI diffractometer with Cu K $\alpha$  radiation ( $\lambda = 1.54056 \text{ \AA}$ ). Raman spectra was collected by Renishaw inVia Reflex instrument with 532 nm laser. The fluorescence images were obtained by laser confocal fluorescence microscopy (LEICA, TCS SP5).

#### **2.4.2 Cell culture**

MCF-7 is a human breast cancer cell line. A549 is a human non-small cell lung carcinoma cell line. Raw264.7 is a mouse monocyte macrophage leukemia cell line. These three cell lines are bought from Shanghai Institutes for Biological Sciences (SIBS). All the cells were cultured in complete culture medium (90% DMEM, 10% FBS) under standard cell culture condition (5% CO<sub>2</sub>, 37 °C). For experiments, cells were detached by 0.25% trypsin solution and resuspended in PBS solution.

#### **2.4.3 Simulation of optimum capture flow rate in microfilter**

Numeric simulation was performed to compare the flow dynamics of WBC

clearance when flowing through the microfilter with different flow rate at range of 0.1–0.9 mL/min using simplified geometry and boundary conditions by ANSYS Fluent software. The purpose of simulation was to find a proper flow rate to avoid plugging of microfilter and cell damaging.

### **Governing equation**

First, a 2D numerical model was developed to investigate the WBC clearance when flowing through a hole with depth of 30  $\mu\text{m}$ , top diameter of 6.5  $\mu\text{m}$  and bottom diameter of 16  $\mu\text{m}$  in the microfilter. The photo of microfilter was shown in Figure 2.5. Only one hole was considered for the sake of saving computational cost.

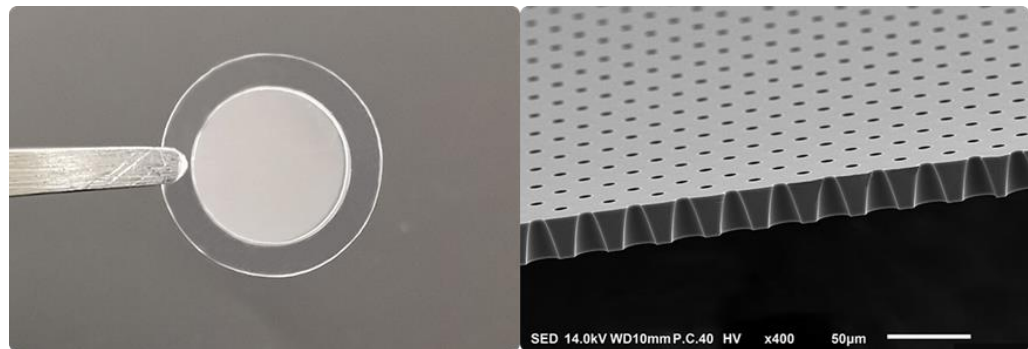


Figure 2.5: Optical image of microfilter.

The volume of fluid (VOF) model in Ansys Fluent 15.0 was used to study the effects of different blood flow rates on the shape and structure of WBCs. In the VOF model, the volume fraction  $\alpha$  can be obtained from the continuity equations (1) and (2)

$$\frac{\partial \alpha_d}{\partial t} + \vec{u} \cdot \nabla \alpha_d = 0 \quad (1)$$

$$\frac{\partial \alpha_c}{\partial t} + \vec{u} \cdot \nabla \alpha_c = 0 \quad (2)$$

where the subscript c represents the continuous phase (blood), and the subscript d represents the dispersed phase (WBCs). The sum of the volume fractions of the two-phase fluid in each computational cell is 1, i.e.,  $\alpha_d + \alpha_c = 1$ ,  $t$  is the flow time,  $\vec{u}$  is the flow velocity which can be obtained from continuity equation and Navier-Stokes equation

$$\nabla \cdot \vec{u} = 0 \quad (3)$$

$$\frac{\partial \rho \vec{u}}{\partial t} + \nabla(\rho \vec{u} \cdot \vec{u}) = -\nabla p + \nabla \cdot [\mu(\nabla \vec{u} + \nabla \vec{u}^T)] + \rho \vec{g} + \vec{F}_s \quad (4)$$

where  $p$  and  $\vec{F}_s$  are the pressure, and surface tension, respectively. In each computational cell, the density  $\rho$  and dynamic viscosity  $\mu$  are calculated by Eq. (5) and (6)

$$\rho = \alpha_c \rho_c + \alpha_d \rho_d \quad (5)$$

$$\mu = \alpha_c \mu_c + \alpha_d \mu_d \quad (6)$$

The surface tension  $\vec{F}_s$  is obtained by the continuous phase surface tension model, as shown in Eq. (7)

$$\vec{F}_s = \frac{\rho}{\frac{1}{2}(\rho_c + \rho_d)} \sigma \kappa \nabla \alpha \quad (7)$$

where  $\sigma$  is the surface tension coefficient,  $\kappa$  is the interface curvature and

$\kappa = \nabla \cdot \hat{n}$ ,  $\hat{n}$  is the surface unit normal calculated by  $\hat{n} = \frac{\vec{n}}{|\vec{n}|}$ , and  $\vec{n} = \nabla \alpha$ .

Wall adhesion is considered by defining a contact angle  $\theta_w$  at the channel wall, and the surface normal at the reference cell next to the wall is calculated by

equation (8)

$$\hat{n} = \hat{n}_w \cos \theta_w + \hat{t}_w \sin \theta_w \quad (8)$$

Where  $\hat{n}_w$  and  $\hat{t}_w$  are the unit vectors normal and tangential to the wall, respectively. The geometric parameters and material properties in the VOF simulation are shown in Table 2.1 and Table 2.2, respectively. The PRESTO! Interpolation scheme was employed to compute the pressure equation. The convective and diffusion terms were discretized using second-order upwind and central difference schemes, respectively. The momentum equation adopted the second-order upwind scheme, and the volume fraction was solved by Geo Reconstruct method.

Table 2.1: Geometry of microchannel

| Upper aperture    | Lower aperture   | Depth of hole    | Distance from inlet to upper pore | Distance from outlet to lower pore |
|-------------------|------------------|------------------|-----------------------------------|------------------------------------|
| 6.5 $\mu\text{m}$ | 16 $\mu\text{m}$ | 30 $\mu\text{m}$ | 30 $\mu\text{m}$                  | 20 $\mu\text{m}$                   |

Table 2.2: Physical parameters of leukocytes and blood [203]

|       | Density ( $\text{kg}\cdot\text{m}^{-3}$ ) | Viscosity ( $\text{pa}\cdot\text{s}$ ) | Interfacial tension ( $\text{N}\cdot\text{m}^{-1}$ ) | Contact angle ( $^\circ$ ) |
|-------|---|--|--|----------------------------|
| Blood | 1055.5                                    | 0.03                                   | 0.027  | 135                        |
| WBCs  | 1080.0                                    | 13                                     |  |                            |

In the previous simulation, the WBCs are considered as liquid, however the real WBCs are surrounded by a thin membrane. To capture the interaction

physics during the contact between the cell membrane and the solid boundary of the hole in the microfilter, i.e., the wall of the micropore as shown in Figure 2.6, the simulation was also conducted with the effect of carrier flow simplified as an axial pressure at the top. Since the inner structure of the cell was neglected, a homogeneous pressure was applied on the inner boundary of the cell. The solid mechanics calculation was performed for the thin membrane of the cell with a thickness of 0.5  $\mu\text{m}$ , which has contact with the wall of the micropore. This simulation was conducted using a 3D model by solid mechanics governed by,

$$\nabla \cdot (FS)^T + F_V = 0 \quad (9)$$

Where  $F = I + \nabla u$ .  $S$  is the 2<sup>nd</sup> Piola-Kirchhoff stress; thus,  $FS$  is the 1<sup>st</sup> Piola-Kirchhoff stress;  $F_V$  represents the term of volume force. The contact pressure from the source of contact pair is,

$$T_n = \text{if} (g_n \leq 0, -p_n g_n, 0) \quad (10)$$

where  $p_n = \frac{E_{char}}{h_{min}}$  is the contact pressure penalty factor,  $E_{char}$  is the characteristic stiffness,  $g_n$  is the gap distance. The tangential force  $T_t$  is computed as

$$T_t = \min \left( \frac{T_{t,crit}}{|T_{t,trial}|}, 1 \right) T_{t,trial} \quad (11)$$

where  $T_{t,trial} = -p_t S$ ,  $T_{t,crit} = \min(\mu T_n + T_{cohe}, T_{t,max})$  is the critical value of tangential force,  $T_{cohe}$  is the cohesion force;  $p_t$  is the penalty factor identified as the spring constant,  $\mu$  is the friction coefficient defined as

$$\mu = \begin{cases} \mu_d + (\mu_s - \mu_d) \exp(-\alpha_{def} |v_s|) \\ \mu_s \end{cases} \quad (12)$$

where  $\mu_d$  is the dynamic friction coefficient,  $\mu_s$  is the static friction coefficient,  $v_s$  is the slip velocity, and  $\alpha_{def}$  is a decay coefficient. The upper equation is the equation of dynamic friction, while the lower represents otherwise.

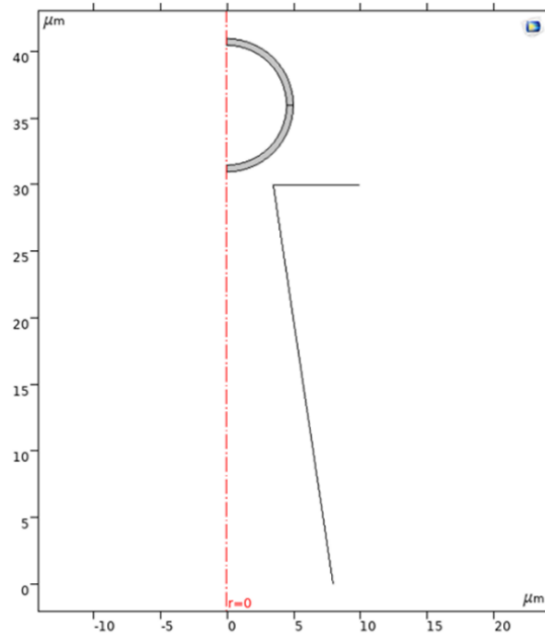


Figure 2.6: The schematic of the WBC flowing through a hole of the microfilter.

#### **2.4.4 Sensitivity, specificity, and capture assay of microfilter combined SERS spectral detection method in mixed cells**

To test the sensitivity and capture assay of this method in mixed cells, the cell suspension solution of MCF-7, A549, raw264.7 and MCF-7 mixed with raw264.7, were added into microfilter device at 1-100 cells/mL concentration.

The concentration of cell suspension solution before and after microfiltration was counted by cell counter. The isolation experiment was performed at a

constant pulling speed (0.4 mL/min) controlled by a micro syringe pump. After that, the B-TiO<sub>2</sub> SERS biological probe was added into microfluidic device and incubated with isolated cells for 1 hour. Then, the microfilter was washed carefully by PBS solution. After that, the microfilter was illuminated by 532 nm laser of Raman instrument. The SRES detection results were verified by fluorescence microscope.

#### **2.4.5 Sensitivity, specificity, and capture assay of microfilter combined SERS spectral detection method in blood**

To test the sensitivity and capture assay of this method in the blood, MCF-7 cell line was spiked into rabbit blood at 1-100 cells/mL concentration. The MCF-7 spiked blood was diluted by PBS solution with volume ratio of 1:2 and added into microfilter device. The concentration of cell suspension before and after microfiltration was counted by cell counter. The isolation experiment was performed at a constant pulling speed (0.4 mL/min) controlled by a micro syringe pump. After that, the B-TiO<sub>2</sub> SERS biological probe was added into microfluidic device and incubated with isolated cells for 1 hour. Then, the microfilter was washed carefully by PBS solution. After that, the microfilter was illuminated by 532 nm laser of Raman instrument. The SRES detection results were verified by fluorescence microscope.

#### **2.4.6 Application in clinical tumor blood detection**

To explore the clinical utility of SERS biological probe, blood samples from 6 breast cancer patients and 2 healthy donors were detected. The blood sample was diluted by PBS solution with volume ratio of 1:2 before microfiltration. The diluted blood sample was added into microfluidic device. The isolation experiment was performed at a constant pulling speed (0.4 mL/min) controlled with a micro syringe pump. After that, the B-TiO<sub>2</sub> SERS biological probe was added into microfluidic device and incubated with isolated cells for 1 hour. After washed by PBS solution, the microfilter was illuminated by 532 nm laser of Raman instrument. The SERS spectral was gathered to analyze the detection result.

#### **2.5 Conclusion**

This chapter has introduced methodology used for research. MCF-7, A549 and Raw264.7 cell lines were used for experiment. The performance of both SPION-PEI@Au based SERS biological probe and B-TiO<sub>2</sub> based SERS biological probe have been tested. 32 blood samples from cancer patients and 3 blood samples from healthy people were detected by PION-PEI@Au based SERS biological probe. The sensitivity, specificity, and capture assay of microfilter combined SERS spectral detection method in mixed cells and blood have also been studied respectively. The combined method has also been applied in clinical blood sample detection. The corresponding experimental

results would be shown in Chapter 3 to 5.

## **Chapter 3 Synthesis of SPION-PEI@AuNPs-based SERS biological probe and application on CTC detection**

### **3.1 Introduction**

Circulating tumor cells (CTCs) are tumor cells shedding from the primary or metastatic tumor and entering the peripheral blood circulation system. CTCs have incubation period in the blood. Some of CTCs would translate to other tissue and form new tumors[204, 205]. Therefore, CTCs detection have important significance for early diagnosis, prognosis evaluation, therapeutic efficacy, and method selection of cancer treatment. However, the number of CTCs in the blood is extremely small, with only 1-10 CTCs per milliliter, among 1 million white blood cells (WBCs) and 1 billion red blood cells (RBCs)[48]. Because of small amounts of CTCs, there is no effective means to detect CTCs at present. Therefore, developing an ultra-sensitive method for CTC detection is quite necessary.

SERS method is an ultra-sensitive method which can be used for molecular level detection. There are many studies using SERS method to detect CTCs in peripheral blood. In previous work, an improved SERS-active magnetic nanoparticles for CTC detection and analysis has been designed [199]. As shown in Figure 3.1, superparamagnetic iron oxide nanoparticles (SPION) with poly(ethyleneimine) (PEI) on the surface (SPION-PEI), was assembled with AuNPs and then linked with Raman reporter molecule MBA and rBSA-FA

sequentially. CTCs could be enriched by SERS biological probe using a magnet and detected by Raman instrument. The SPION-PEI@AuNPs-MBA-rBSA-FA SERS biological probes realized the integration of CTC separation and detection.

This chapter focuses on the clinical application of SPION-PEI@AuNPs-MBA-rBSA-FA SERS biological probes. The specificity and separation performance of SPION-PEI@AuNPs SERS biological probe has been replicated. After that, the SPION-PEI@AuNPs SERS biological probe has been applied to detect several blood samples from cancer patients. The successful CTC detection in clinical cancer patient bloods demonstrated that SERS detection was worth to be further developed and a promising tool for diagnosis and treatment of cancer.

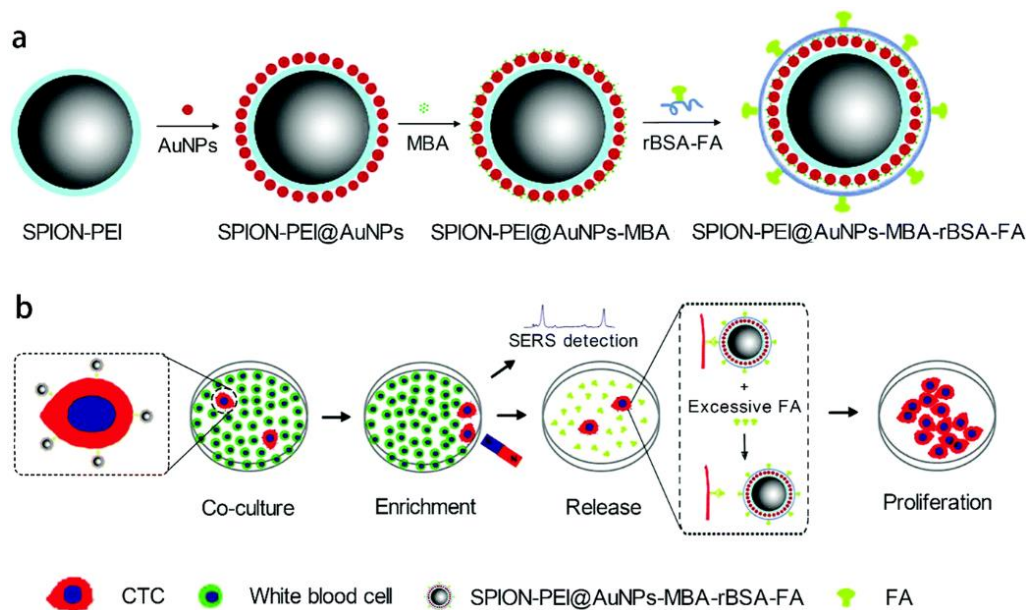


Figure 3.1: Design of magnetic SERS biological probe and separation mechanism. a) Design of the magnetic SERS biological probe: SPION-PEI@AuNPs-MBA-rBSA-FA; b) Mechanism of the SERS nanoagent for CTC analysis.

### 3.2 Characterization of SPION-PEI@AuNPs-based SERS biological probe

The SPION-PEI@AuNPs SERS biological probe was composed according to synthetic steps from Figure 3.1a. The SPION-PEI was prepared by solvothermal synthesis method and AuNPs was prepared by sodium citrate reduction of chloroauric acids. Figure 3.2 shows the morphological features of SPION-PEI, AuNPs, SPION-PEI@AuNPs and SPION-PEI@AuNPs-MBA-rBSA-FA. The TEM images showed that the size of AuNPs was 30-40 nm, and the size of SPION-PEI was 200-300 nm (Figure 3.2a and 3.2b). Figure 3.2c showed that SPION-PEI@AuNPs has Core-satellite structures with size of 250-350 nm. After functionalized by rBSA-FA, there was a layer of film on the

nanoparticles as shown in Figure 3.2d. The Zeta potential of AuNPs and SPION-PEI were -47.3 mV and +27.7 mV, respectively (Figure 3.3). AuNPs with negative charge were self-assembled on the SPION-PEI by electrostatic attraction. After electrostatic attraction, the Zeta potential of SPION-PEI@AuNPs was changed to -33.1 mV. The strong repulsive force made SPION-PEI@AuNPs of good dispersibility in water. The SERS spectral of SPION-PEI@AuNPs, SPION-PEI@AuNPs-MBA and SPION-PEI@AuNPs-MBA-rBSA-FA were shown in Figure 3.4. Because the layer of rBSA was relatively thin, the SERS intensity of SPION-PEI@AuNPs-MBA-rBSA-FA showed almost no weakening after covered by rBSA-FA and has good stability. The depth scanning results of SPION-PEI@AuNPs-MBA-rBSA-FA showed that this SERS biological probe has good stability and uniformity in the solution.

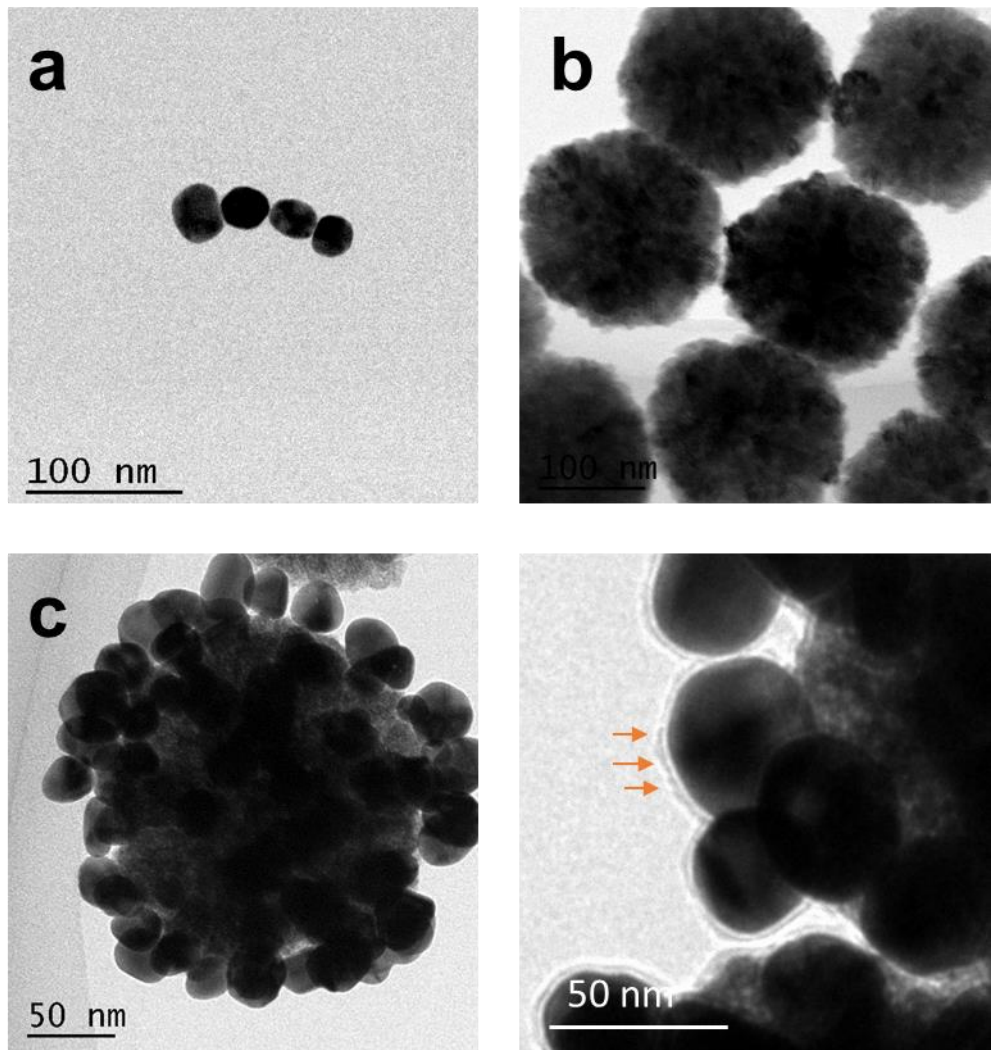


Figure 3.2: TEM images of a) AuNPs, b) SPION-PEI, c) SPION-PEI@ AuNPs, d) the layer of rBSA-FA.

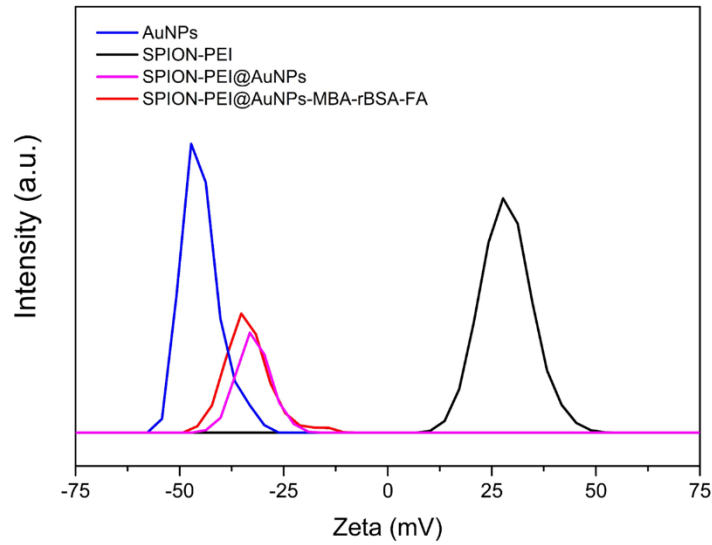


Figure 3.3: Zeta potential distribution of AuNPs, SPION-PEI, SPION-PEI@AuNPs, and SPION-PEI@AuNPs-MBA-rBSA-FA.

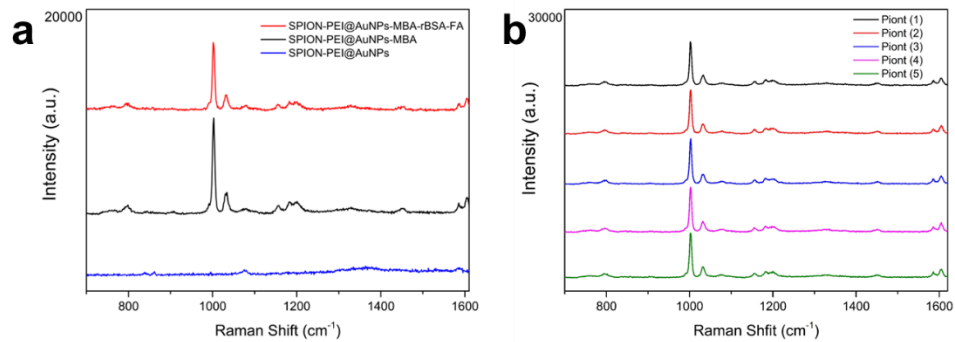


Figure 3.4: a) SERS spectral of SPION-PEI, SPION-PEI@AuNPs-MBA and SPION-PEI@AuNPs-MBA-rBSA-FA; b) SERS spectral of SPION-PEI@AuNPs-MBA-rBSA-FA from randomized 5 points by depth scanning, depth (1-5) -100, -200, -300, -400, -500  $\mu\text{m}$ . Laser wavelength: 785 nm; lens: 50  $\times$  objective.

### 3.3 Specificity of SPION-PEI@AuNPs-based SERS biological probe in cells

To test the specificity of SPION-PEI@AuNPs-based SERS biological probe, MCF-7 cells and A549 cells were incubated with PBS solution, SPION-PEI@AuNPs-MBA and SPION-PEI@AuNPs-MBA-rBSA-FA, respectively. Figure 3.5 indicated that after functionalized by rBSA-FA, SERS biological probes could target FR positive cells. Because A549 cells were FR negative cells, the FA molecule on the SERS biological probe cannot target A549 cells. Besides, SERS biological probe without FA modification cannot target folate receptor on the cell membrane. On the other hand, it also proved that the SERS biological probe has been successfully modified by FA molecule. As shown in Figure 3.5, there were appreciable SPION-PEI@AuNPs-MBA-rBSA-FA biological probe on the MCF-7 cells while there was few SPION-PEI@AuNPs-MBA-rBSA-FA biological probe on the A549 cells. Figure 4.6a showed the SERS spectral of MCF-7 cells and A549 cells after incubated with SPION-PEI@AuNPs-MBA-rBSA-FA. Besides, the stability of SPION-PEI@AuNPs-MBA-rBSA-FA have been tested by the SERS imaging of single MCF-7 cell and A549 cell as shown in Figure 3.6a. As shown in Figure 3.6b, MCF-7 cells have peak signal at  $1076\text{ cm}^{-1}$  while there was no peak signal for A549 cells. Besides, peak intensity at  $1076\text{ cm}^{-1}$  was increased when there were MCF-7 cells. Therefore, the Raman peak at  $1076\text{ cm}^{-1}$  was utilized for mapping biological probe in the cell surface. The red area showed obvious

SERS intensity at  $1076\text{ cm}^{-1}$  and the dark area showed no SERS intensity at  $1076\text{ cm}^{-1}$ . These results showed good specificity and stability of SPION-PEI@AuNPs-MBA-rBSA-FA to FR positive cells, which could profit CTC detection in the clinical blood samples. In addition to the specificity, separation performance has also been repeated. Figure 3.7 showed separated MCF-7 cells.

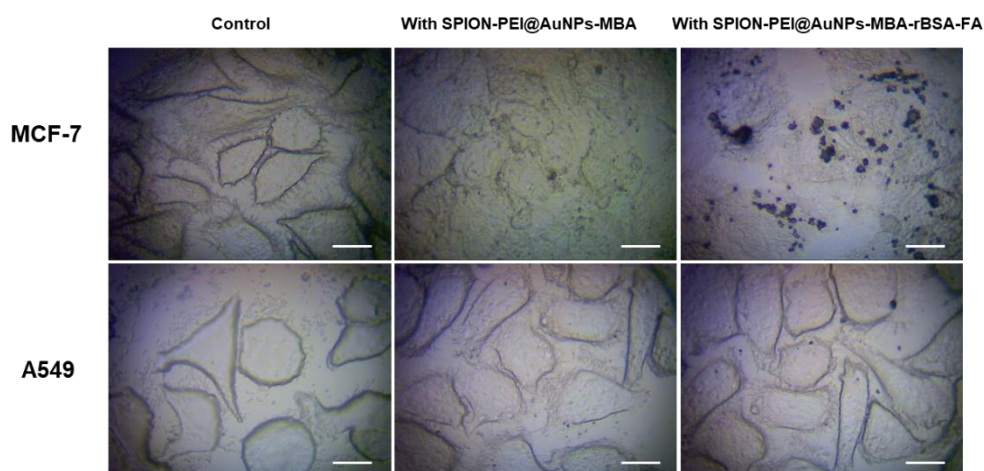


Figure 3.5: Optical images of MCF-7 and A549 after incubated with PBS solution, SPION-PEI@AuNPs-MBA SERS biological probe and SPION-PEI@AuNPs-MBA-rBSA-FA SERS biological probe. Scale bar:  $20\text{ }\mu\text{m}$ .

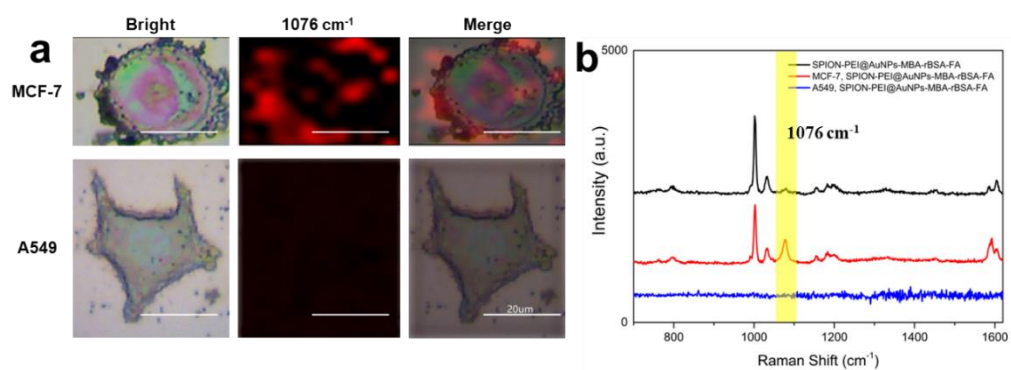


Figure 3.6: a) SERS imaging of MCF-7 and A549 cell at bright, 1076  $\text{cm}^{-1}$  intensity peak and merge background. Scale bar: 20  $\mu\text{m}$ . b) SERS spectral of MCF-7 and A549.

### 3.4 Sensitivity and separation of SPION-PEI@AuNPs-based SERS biological probe in blood

To study the sensitivity of SPION-PEI@AuNPs-based SERS biological probe for CTC detection, different proportions of MCF-7 cells were added into health rabbit blood to imitate peripheral blood environment of cancer patients. Concentration gradient dilution method can accurately control the number of cancer cells added to rabbit blood by diluting cell suspension to concentration of 500, 250, 100, 50, 10, and 5 cells per milliliter. As shown in Figure 3.7, when there were 5 MCF-7 cells added into rabbit blood, MCF-7 cells could be detected and separated.

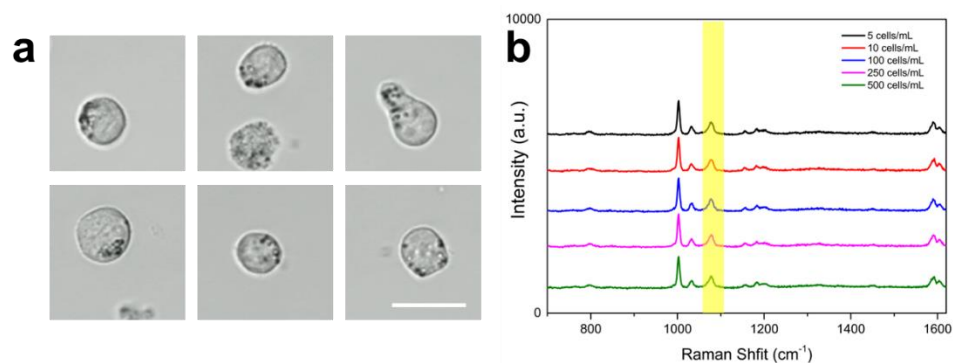


Figure 3.7: a) Optical image of separated MCF-7 cells from 5-500 cells/mL mixed cell suspension, Scale bar: 20  $\mu\text{m}$ ; b) Raman spectral of separated cells.

### 3.5 Application of SPION-PEI@AuNPs-based SERS biological probe in the clinical blood samples

SPION-PEI@AuNPs-based SERS biological probe has been proved to have good detection efficiency and veracity. It has been applied to CTC detection of clinical blood samples. To test the performance of SPION-PEI@AuNPs-based SERS biological probe in clinical blood detection, 32 blood samples from tumor patients and 3 blood samples from healthy people have been detected. Figure 3.8 showed detection results of healthy people blood samples. It showed that there was no peak enhancement at  $1076\text{ cm}^{-1}$ . Figure 3.9 showed SERS detection results of 32 blood samples. Compared to healthy blood results, there were obvious peak enhancement at  $1076\text{ cm}^{-1}$  in almost spectral. However, there were still 5 tumor blood samples detected without  $1076\text{ cm}^{-1}$  peak as shown in red frame, which could be defined as false negative results. Besides, the Raman spectral was unstable due to complex blood background. There were many undesired peaks appeared which would disturb determination of

results. Therefore, the stability of SERS biological probe in blood should be improved and it is better to remove the complex background before SERS detection so that the accuracy of results could be improved.

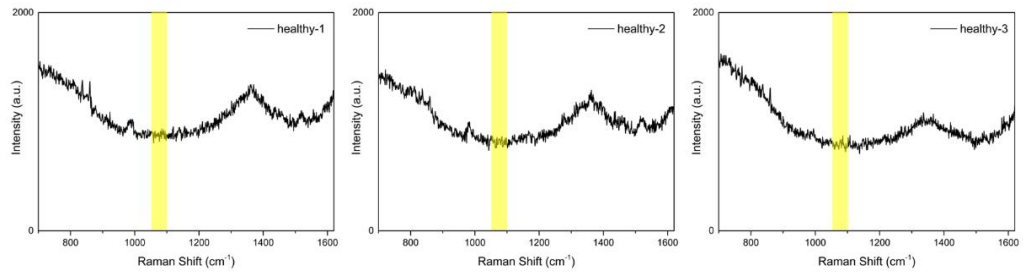


Figure 3.8: SERS detection results of blood from healthy people.

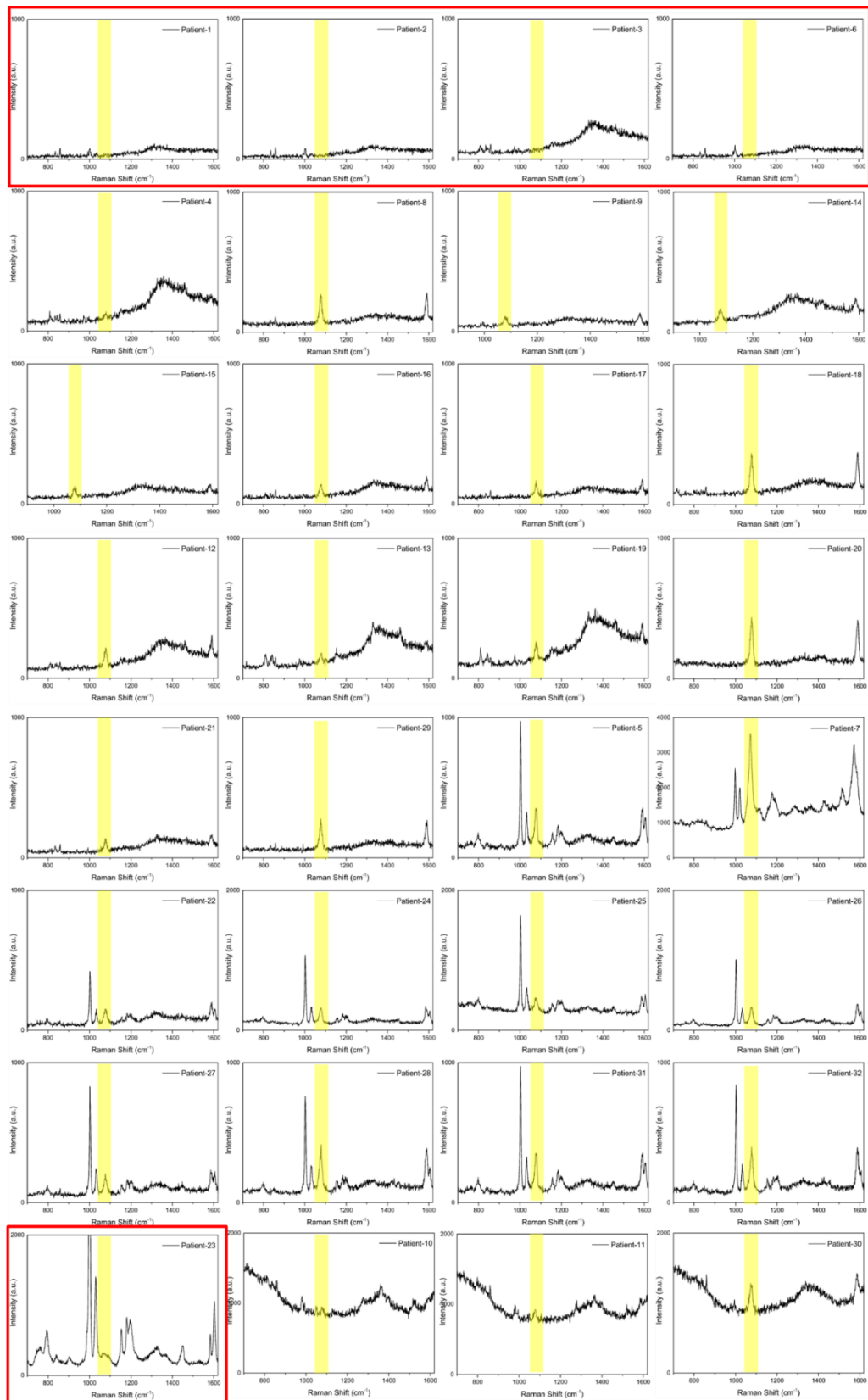


Figure 3.9: SERS detection results of 32 tumor blood samples.

### **3.6 Chapter conclusion**

In summary, SPION-PEI@AuNPs-MBA-rBSA-FA SERS biological probe was successfully reproduced and applied for CTC detection. The SERS-active magnetic nanoparticles were demonstrated to have good specificity and sensitivity to MCF-7 cells. The LOD of CTC detection was measured to be 5 cell per mL. 32 cancer blood samples and 3 blood samples from healthy people were tested. Although the results showed good specificity and separation efficacy, there are still some limitations to be overcome. For examples, density gradient centrifugation as blood pretreatment method may cause loss of targeted cells and redundant SERS biological probes could not be effectively removed, which will cause false negative results and false positive results, respectively. Besides, hot-spot effect between noble nanoparticles might also disturb judgment of results.

## **Chapter 4 Synthesis of B-TiO<sub>2</sub>-based SERS biological probe and application on CTC detection**

### **4.1 Introduction**

In the third chapter, gold-iron oxide composite nanoparticles were used as SERS substrate for CTC detection. Although it has strong SERS intensity, the hot spot efficacy might cause false positive results. Besides, the toxicity to living organisms and nonselective SERS enhancement of targeted molecules limit their application in CTC detection[117, 206]. It has been reported that low-cost semiconductor nanomaterials can also exhibit high SERS performance with advantages of high spectral stability and reproducibility, strong anti-interference ability, and selective SERS enhancement of target molecules[117]. Lin et al. firstly investigated the crystal-amorphous core-shell heterojunction boosted photoinduced charge transfer (PICT) process for the enhancement of black TiO<sub>2</sub> (B-TiO<sub>2</sub>)-molecule system and applied it to the detection of cancer cells[118]. The PICT process is formed between the substrate and the target molecules[130]. The strong vibration coupling in a semiconductor molecule system can effectively increase the molecular polarizability and amplify the Raman scattering cross section[125]. The amorphous structure of TiO<sub>2</sub> improved the PICT efficiency, yield an ultrahigh SERS enhancement factor (EF) and, achieve higher performance of semiconductor-based SERS substrates[207]. Therefore, semiconductor-based SERS substrate shows great potential in CTC analysis.

In this chapter, black TiO<sub>2</sub> was used as SERS substrate for CTC detection to reduce hot spot efficacy. FA-functionalized SERS biological probe has been designed to distinguish CTCs from the remaining WBCs by targeting the FA biomarkers on the CTC membranes. The SERS biological probe was composed by a crystal-amorphous core-shell B-TiO<sub>2</sub> SERS substrate, Raman reporter alizarin red (AR) molecule, a thin NH<sub>2</sub>-PEG2000-COOH (PEG) layer to improve the dispersion of biological probe, and FA to specifically recognize folate receptor (FR) on cancer cell membrane (Figure 2.4). Besides, abundant amino group of the PEG layer can provide sufficient binding sites for FA coupling, which is benefit for improving the detection specificity and accuracy of B-TiO<sub>2</sub> based biological probe. SERS-fluorescence bimodal imaging method verified high detection specificity of this strategy. In addition, SERS results demonstrated that FR positive MCF-7 cancer cells could be captured efficiently with reliability and specificity compared to FR negative cancer cells (A549 and Raw264.7 cells).

#### **4.2 Characterization of B-TiO<sub>2</sub>-Based SERS biological probe**

B-TiO<sub>2</sub> NPs have been successfully fabricated. As shown in Figure 4.1, the color of B-TiO<sub>2</sub> was black while the color of P25 was white. The Low-resolution transmission electron microscopy (TEM) and the High-resolution transmission electron microscopy (HRTEM) were used to identify the

microstructure and morphology of B-TiO<sub>2</sub> NPs. The TEM image showed the particle size of B-TiO<sub>2</sub> NPs was ~25 nm (Figure 4.2a). The HRTEM image showed a crystal-amorphous core-shell structure of B-TiO<sub>2</sub> NPs (Figure 4.2b). As shown in Figure 4.3, there was an obvious oxygen-deficient amorphous shell with 2-3 nm thickness on the surface of crystalline core. The feature of amorphous shell and crystal core structure was further confirmed by the corresponding fast Fourier transform (FFT) image. The diffuse ring for the shell structure and the points pattern for the core structure were consistent with the HRTEM characterization. The lattice plane distance of the crystalline core was 0.35 nm, corresponding to the (101) crystal planes of anatase TiO<sub>2</sub>. Meanwhile, X-ray diffraction (XRD) showed that both P25 and B-TiO<sub>2</sub> have the major characteristic diffraction peaks of anatase TiO<sub>2</sub> at 25.4° (101) (Figure 4.4). The XRD image also characterized the crystalline structure of P25 NPs before and after reduction. It showed that the crystalline degree was reduced after the reduction because of the formation of an oxygen-deficient amorphous layer. Besides, the increased half width of the Raman peaks for the P25 at 145, 196, 400, 517, and 642 cm<sup>-1</sup> frequencies also indicated the decreased crystallinity in B-TiO<sub>2</sub> NPs (Figure 4.5). At the same concentration of AR, B-TiO<sub>2</sub> has much better SERS performance than P25 (Figure 4.6).

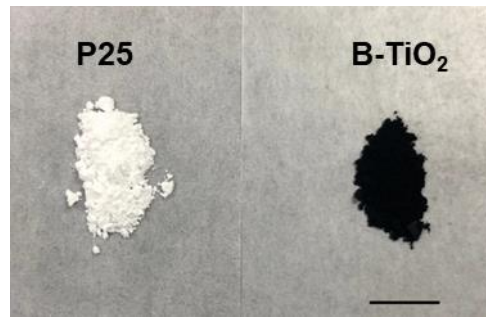


Figure 4.1: Optical photo of P25 and B-TiO<sub>2</sub>, scale bar: 2 cm.

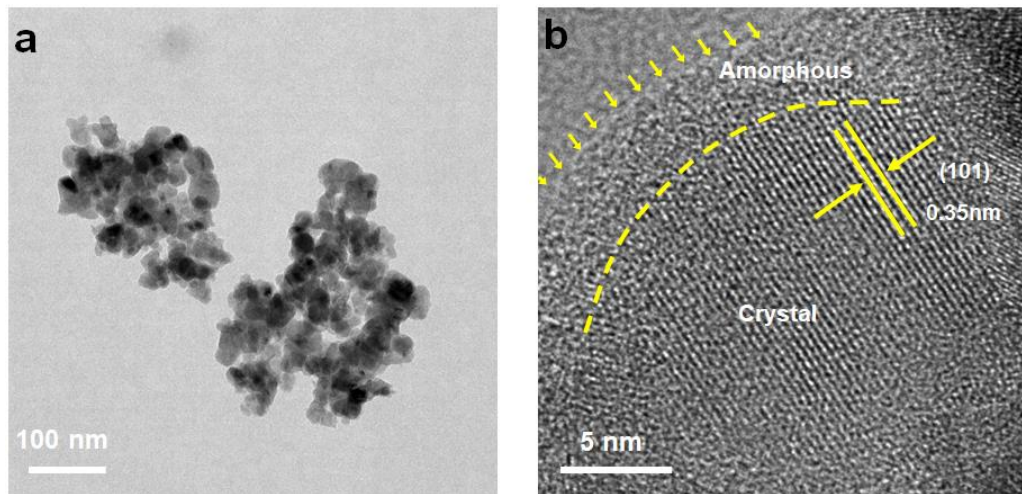


Figure 4.2: a) TEM image of B-TiO<sub>2</sub>; b) HRTEM image of B-TiO<sub>2</sub>.

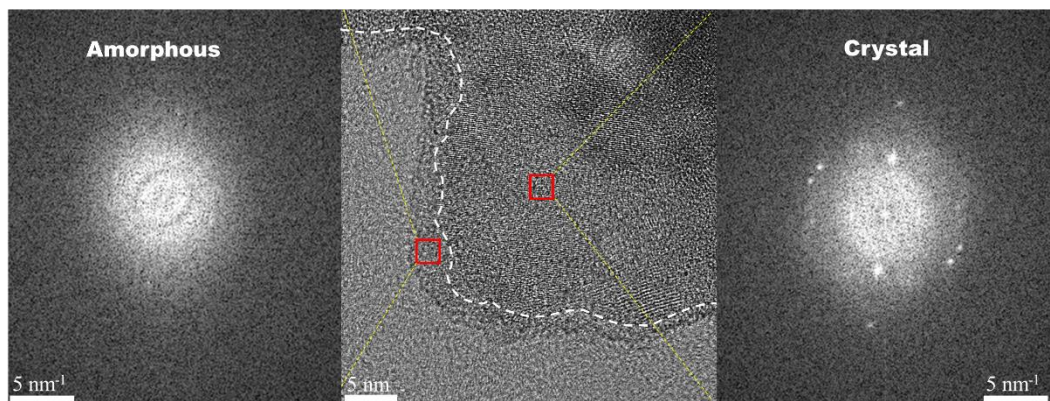


Figure 4.3: FFT image of B-TiO<sub>2</sub>.

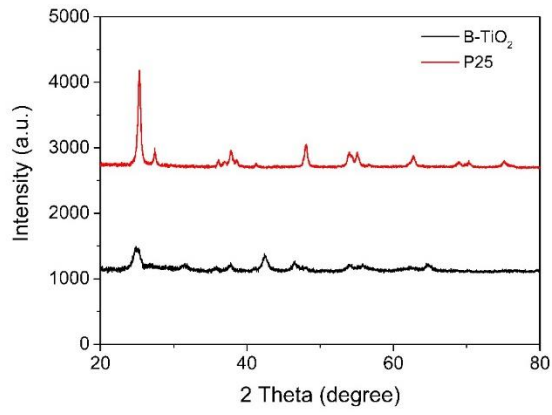


Figure 4.4: X-ray diffraction of P25 and B-TiO<sub>2</sub> NPs.

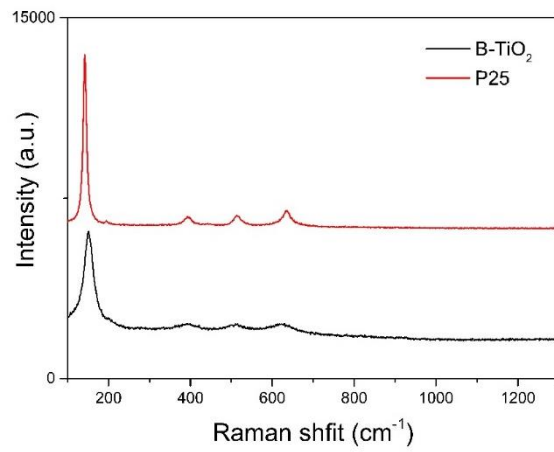


Figure 4.5: Raman characterization of P25 and B-TiO<sub>2</sub> NPs, respectively.

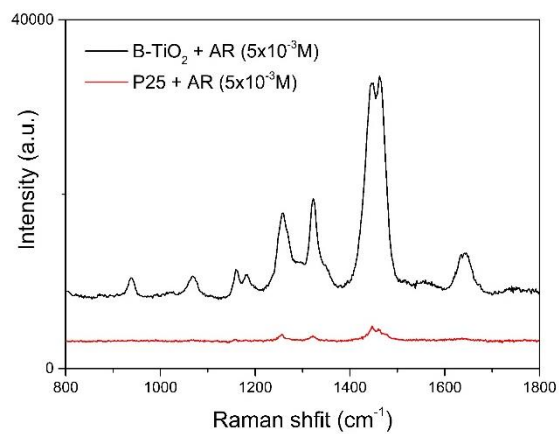


Figure 4.6: SERS spectra of AR adsorbed on the B-TiO<sub>2</sub> NPs and P25 at  $5 \times 10^{-3}$

M.

To investigate the SERS performance of B-TiO<sub>2</sub>, SERS spectra of AR molecules adsorbed on the B-TiO<sub>2</sub> NPs at different concentrations ( $5 \times 10^{-3}$ - $5 \times 10^{-8}$  M) was measured at 532 nm (Figure 4.7). Figure 4.7 showed the Raman spectra difference between AR and AR absorbed on B-TiO<sub>2</sub>. Before AR absorbed on B-TiO<sub>2</sub>, AR has weak Raman spectral. After AR absorbed on B-TiO<sub>2</sub>, the Raman spectral of AR has been strongly enhanced, which indicated that AR has been absorbed on B-TiO<sub>2</sub>. When the concentration of AR is reduced to  $5 \times 10^{-8}$  M, the vibration peak could still be distinguished, indicating that the LOD of the AR molecule on B-TiO<sub>2</sub> can reach  $5 \times 10^{-8}$  M. Compared to some semiconductors as shown in Table 1.5, the SERS performance of B-TiO<sub>2</sub> was significantly great. The concentration of AR used to fabricate SERS biological probe was  $5 \times 10^{-3}$  M. To show the binding of AR on B-TiO<sub>2</sub>, the conjugation efficiency of AR absorbed on B-TiO<sub>2</sub> was calculated by mass balance method. First, after the centrifugation of B-TiO<sub>2</sub>-AR mixture, the supernatant was collected, and the residual AR content was determined using the calibration curve of AR standard solutions by measuring the UV-vis absorption peak at 422 nm (Figure 4.8a and b). To determine the residual AR content more accurately, the supernatant was diluted 3 times before measuring. The conjugation efficiency (CE) of AR on B-TiO<sub>2</sub> was calculated as follows:

$$CE_{AR} = \frac{\text{weight of initial AR} - \text{weight of residual AR}}{\text{weight of (B-TiO}_2\text{-AR)}} \times 100\% \quad (13)$$

Therefore, the CE of AR in B-TiO<sub>2</sub> was 15.1%, which means the amount of AR

is 15.1 mg per 100 mg B-TiO<sub>2</sub>-AR.

To improve the dispersion of B-TiO<sub>2</sub>-AR biological probe and avoid nonspecific adsorption, NH<sub>2</sub>-PEG2000-COOH was used to enwrap B-TiO<sub>2</sub>-AR. The TEM image of B-TiO<sub>2</sub>-AR-PEG showed that there was a thin PEG layer on the particles (Figure 4.9). The thickness of PEG layer was about 4-5 nm.

FA was modified to the SERS biological probe by the amide interaction between the carboxyl group of FA and amino group of NH<sub>2</sub>-PEG2000-COOH. The conjugation efficiency of FA on the SERS biological probe was 2.1% calculated by mass balance method. After the activated FA mixed with B-TiO<sub>2</sub>-AR-PEG stirring for 12 hours, the resulting B-TiO<sub>2</sub>-AR-PEG-FA was obtained by centrifugation at 10000 rpm for 10 minutes. the supernatant was collected, and the residual FA content was determined using the calibration curve of FA standard solutions by measuring the UV-vis absorption peak at 350 nm (Figure 4.10). The conjugation efficiency (CE) of FA on B-TiO<sub>2</sub>-AR-PEG-FA was calculated as follows:

$$CE_{FA} = \frac{\text{weight of initial FA} - \text{weight of residual AR}}{\text{weight of (B-TiO}_2\text{-AR-PEG-FA)}} \quad (14)$$

To further confirm the FA modification, B-TiO<sub>2</sub>-AR-PEG biological probe and B-TiO<sub>2</sub>-AR-PEG-FA biological probe were incubated with FITC linked polyclonal rabbit antibody to FA, respectively. The fluorescence intensity of B-TiO<sub>2</sub>-AR-PEG-FA biological probe (Figure 4.11a) was obviously stronger than

B-TiO<sub>2</sub>-AR-PEG biological probe (Figure 4.11b). The SERS intensity of B-TiO<sub>2</sub>-AR-PEG-FA biological probe was measured as shown in Figure 4.12a. Although the intensity was reduced due to PEG layer, it still has strong signal for satisfying peripheral blood tumor cell detection. The spectra stability of B-TiO<sub>2</sub>-AR-PEG-FA biological probe was also verified in Figure 4.12b, which is in favor of CTC detection in complex peripheral blood environment.

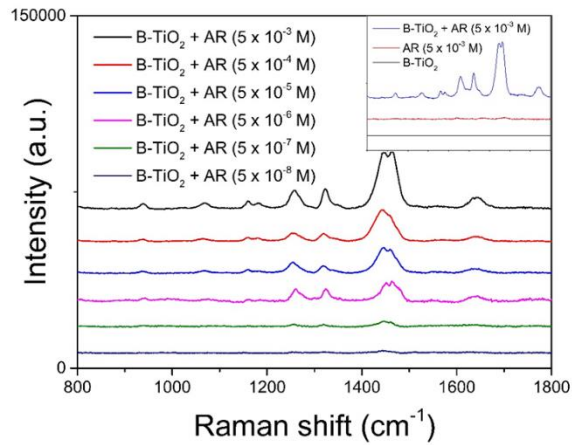


Figure 4.7: SERS spectra of AR, B-TiO<sub>2</sub> and B-TiO<sub>2</sub>-AR NPs at different concentrations ( $5 \times 10^{-3}$ - $5 \times 10^{-8}$  M).

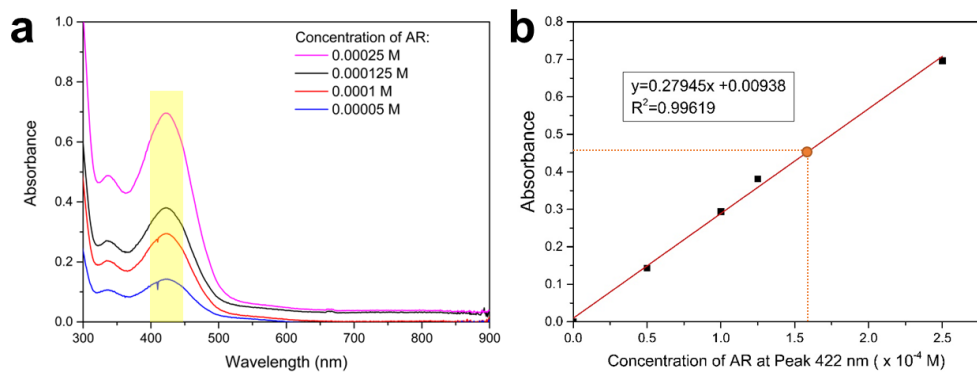


Figure 4.8: a) UV-vis spectra of AR solution. b) Calibration curve of AR standard solutions at peak 422 nm.

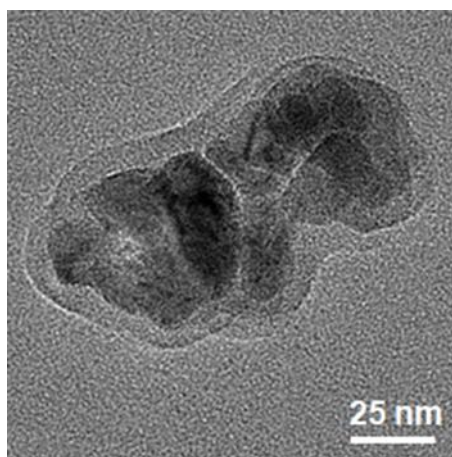


Figure 4.9: TEM image of B-TiO<sub>2</sub>-AR-PEG.

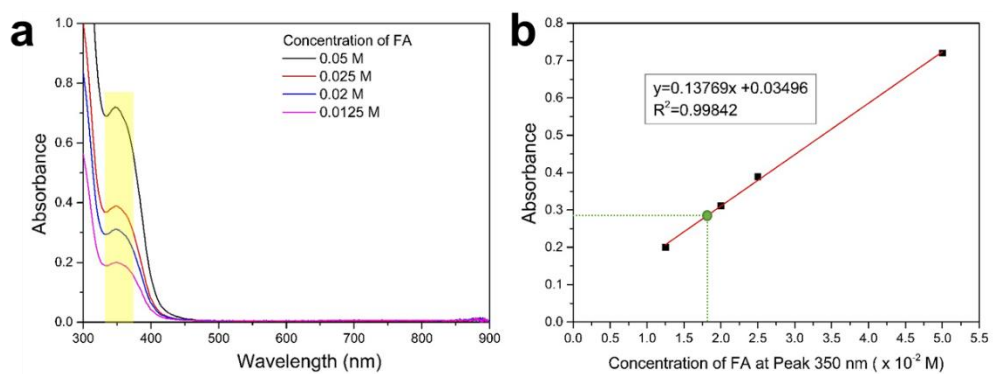


Figure 4.10: a) UV-vis spectra of FA solution. b) Calibration curve of FA standard solutions at 350 nm.

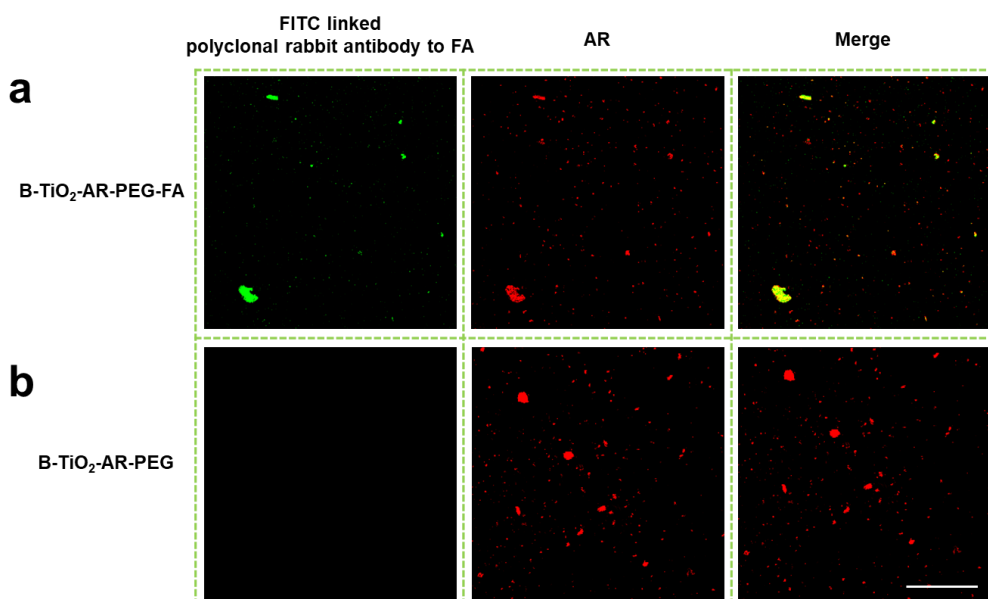


Figure 4.11: Fluorescent images of FITC linked polyclonal rabbit antibody to FA. a) FA modified SERS biological probe. b) non-FA modified SERS biological probe. Scale bar: 50 $\mu$ m.

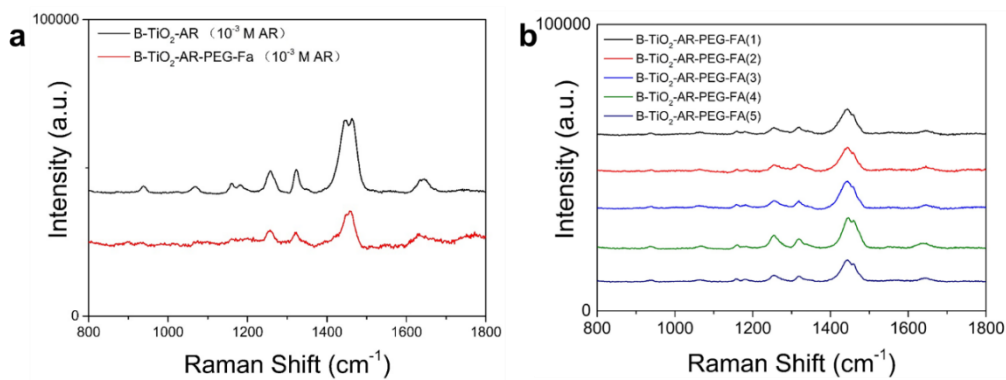


Figure 4.12: a) SERS spectra B-TiO<sub>2</sub>-AR-PEG-FA compared to B-TiO<sub>2</sub>-AR; b) The SERS spectra of SERS biological probe at 5 points.

### 4.3 FR expression screening of MCF-7, A549 and Raw264.7 cell lines

Three cell lines of MCF-7, A549 and Raw264.7 were used to verify the performance of this SERS biological probe. First, the function of FR in the

three types of cell lines was verified by incubating cells with FITC-PEG2000-FA and flow cytometry measurement was carried out. As shown in Figure 4.13, MCF-7 had higher affinity for FITC-PEG2000-FA, while A549 and Raw264.7 showed extremely low affinity. It was demonstrated that MCF-7 was FR positive cell while A549 and Raw264.7 were FR negative cells.

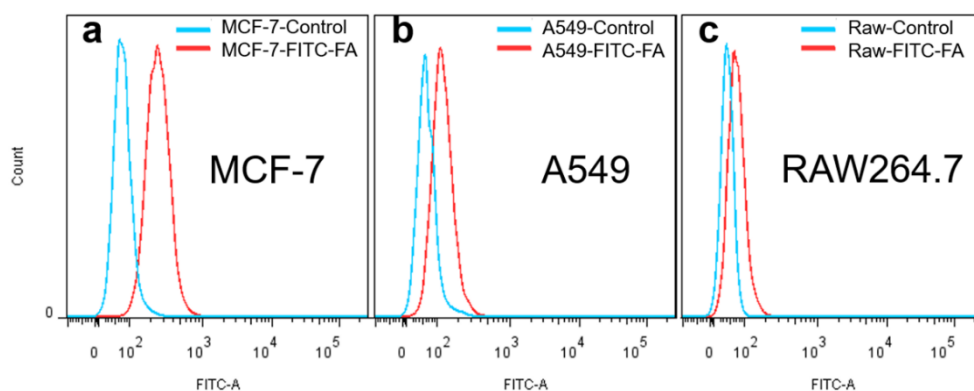


Figure 4.13: Flow cytometry analyses of the function of FR in a) MCF-7, b) A549, c) Raw264.7.

#### 4.4 Specificity and stability of B-TiO<sub>2</sub>-based SERS biological probe in the mixed cells

After incubated with B-TiO<sub>2</sub>-AR-PEG biological probe and B-TiO<sub>2</sub>-AR-PEG-FA biological probe, there were obvious differences between MCF-7 cells and A549 cells (Figure 4.14). For MCF-7 cells, there were B-TiO<sub>2</sub>-AR-PEG-FA biological probes on the cells while there was few B-TiO<sub>2</sub>-AR-PEG biological probe on the cells. For A549 cells, both of B-TiO<sub>2</sub>-AR-PEG biological probe and B-TiO<sub>2</sub>-AR-PEG-FA biological probe were not observed on the cells. To

illustrate detection specificity of B-TiO<sub>2</sub>-AR-PEG-FA biological probe, MCF-7 and A549 cells were also stained by FITC and Hoechst, respectively, as shown in Figure 4.15. MCF-7 cells exhibit red fluorescence on the cell membrane, while A549 cells with almost no red fluorescence on the cell membrane, where the red fluorescence was come from AR molecule absorbed on the SERS biological probe.

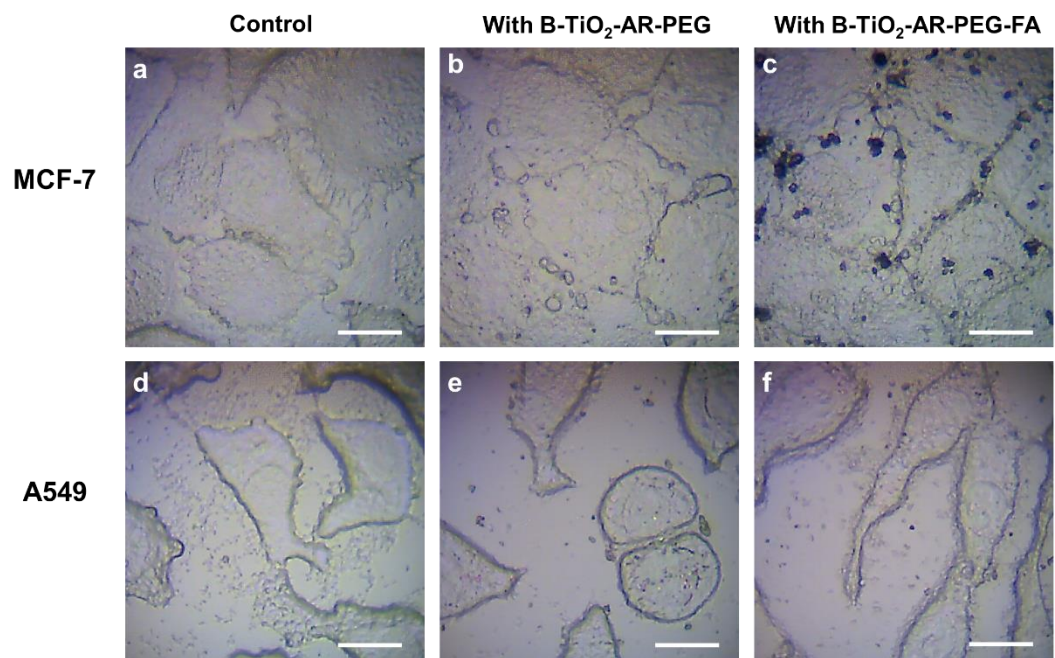


Figure 4.14: Optical images of MCF-7 and A549 after incubated with PBS solution, B-TiO<sub>2</sub>-AR-PEG SERS biological probe and B-TiO<sub>2</sub>-AR-PEG-FA SERS biological probe. Scale bar: 20  $\mu$ m.

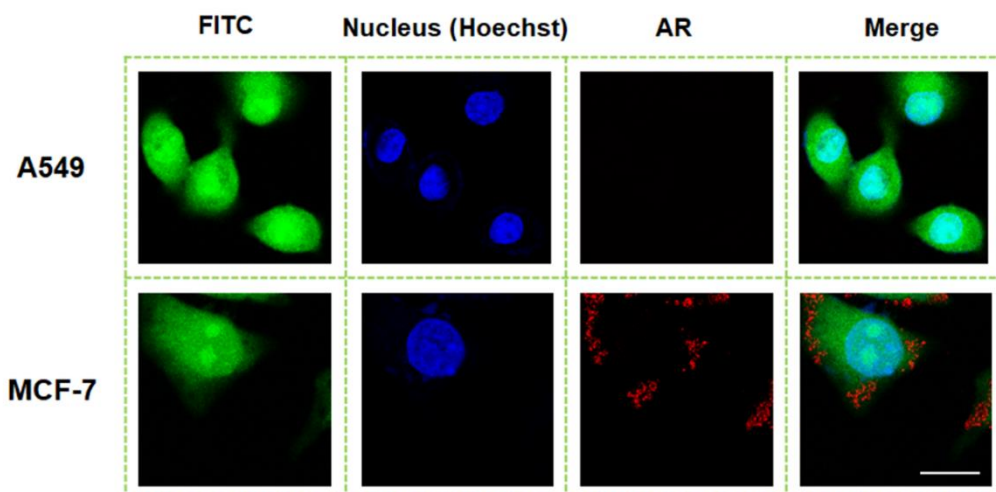


Figure 4.15: Fluorescent images of A549 and MCF-7 incubated with SERS biological probe. Scale bar: 20  $\mu\text{m}$ .

Besides, the SERS mapping images of MCF-7 and A549 cells after incubated with FA modified SERS biological probe were shown in Figure 4.16a. The typical Raman scattering peak of AR molecule at  $1449\text{ cm}^{-1}$  was more significantly enhanced than that at  $1257\text{ cm}^{-1}$ ,  $1326\text{ cm}^{-1}$  exhibited in Figure 4.16b, so the Raman peak at  $1449\text{ cm}^{-1}$  was utilized for mapping biological probe in the cell. Three Raman spectra collected from MCF-7 and A549 respectively, were shown in Figure 4.16b. To make sure the repeatability and reliability of results in Figure 4.16b, other 10 measurements for MCF-7 and A549 were provided, respectively as shown in Figure 4.17. The Error Bars in figures and relative standard deviations (RSD) calculated for the SERS intensity at peak  $1449\text{ cm}^{-1}$  demonstrated the good repeatability of the method. There was no SERS signal observed on A549 cells while MCF-7 had obvious SERS signal on the surface. This result demonstrated that FA modified SERS

biological probe can effectively target cancer cells with FR expression.

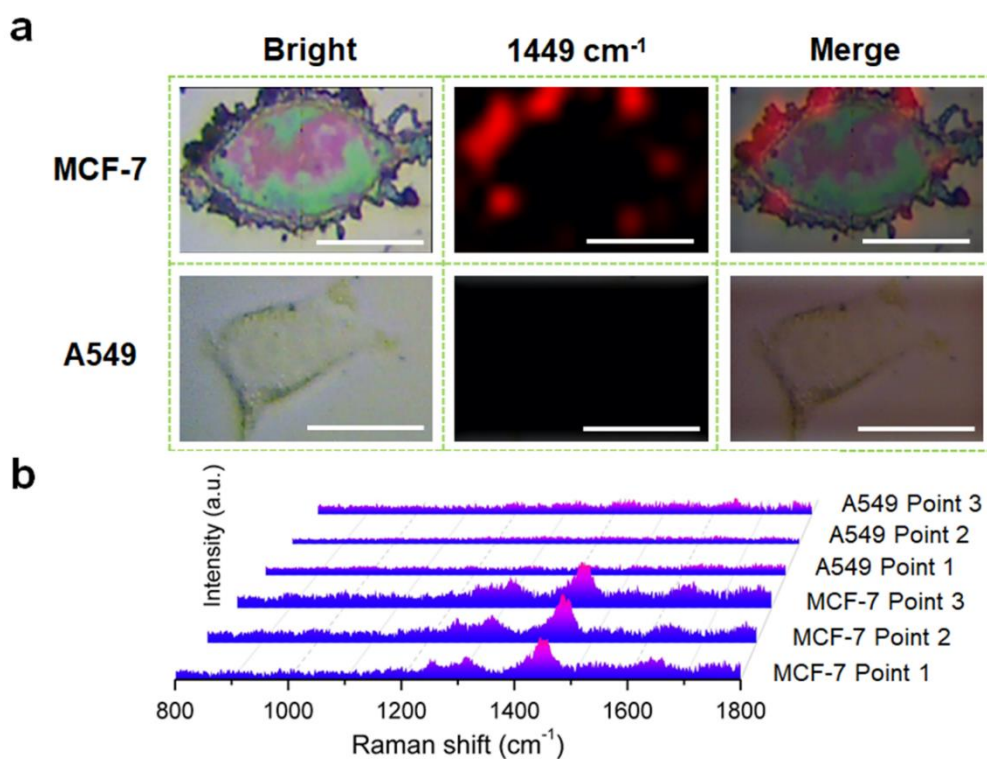


Figure 4.16: a) Optical image and SERS mapping image of MCF-7, and A549 cancer cell at 1449 cm<sup>-1</sup>. Scale bar: 20 μm. b) SERS spectral of SERS biological probe with MCF-7, and A549 cancer cell collected from 3 points, respectively.

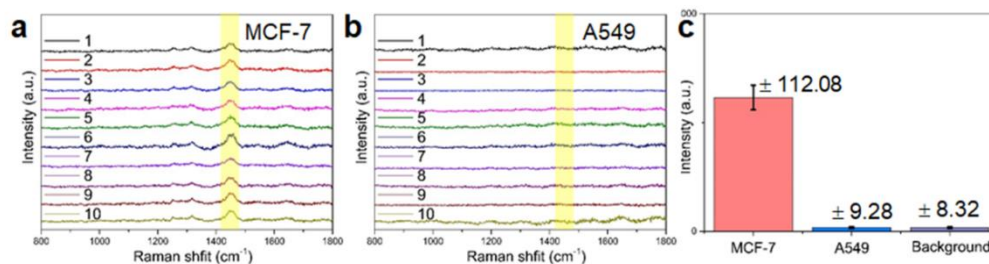


Figure 4.17: a) SERS spectral of SERS biological probe with MCF-7 collected from 10 points. b) SERS spectral of SERS biological probe with A549 collected from 10 points. c) SERS intensity of SERS biological probe with MCF-7 and A549 at peak  $1449\text{ cm}^{-1}$ .

To verify the anti-interference ability of B-TiO<sub>2</sub>-AR-PEG-FA biological probe from FR negative cells, MCF-7 and Raw264.7 cell lines were mixed and incubated with B-TiO<sub>2</sub>-AR-PEG-FA biological probe for 1 hour and washed by PBS for three times. After stained by CK8 (MCF-7 positive, Raw264.7 negative) and Hoechst (MCF-7 positive, Raw264.7 positive), MCF-7 has red fluorescence on cell membrane, blue fluorescence on nucleus and green fluorescence from AR, while Raw264.7 only has blue fluorescence on nucleus (Figure 4.18). To distinguish the fluorescence from AR and Alexa Fluor 647, the fluorescence of AR was set as green and fluorescence Alexa Fluor 647 was set as red. B-TiO<sub>2</sub>-AR-PEG-FA SERS biological probes were obviously observed in MCF-7 cell membrane, while Raw264.7 with only few SERS biological probes. This result showed that B-TiO<sub>2</sub>-AR-PEG-FA SERS biological probe exhibited good anti-interference ability for distinguish MEC-7 cells from the FR negative Raw264.7 cell.

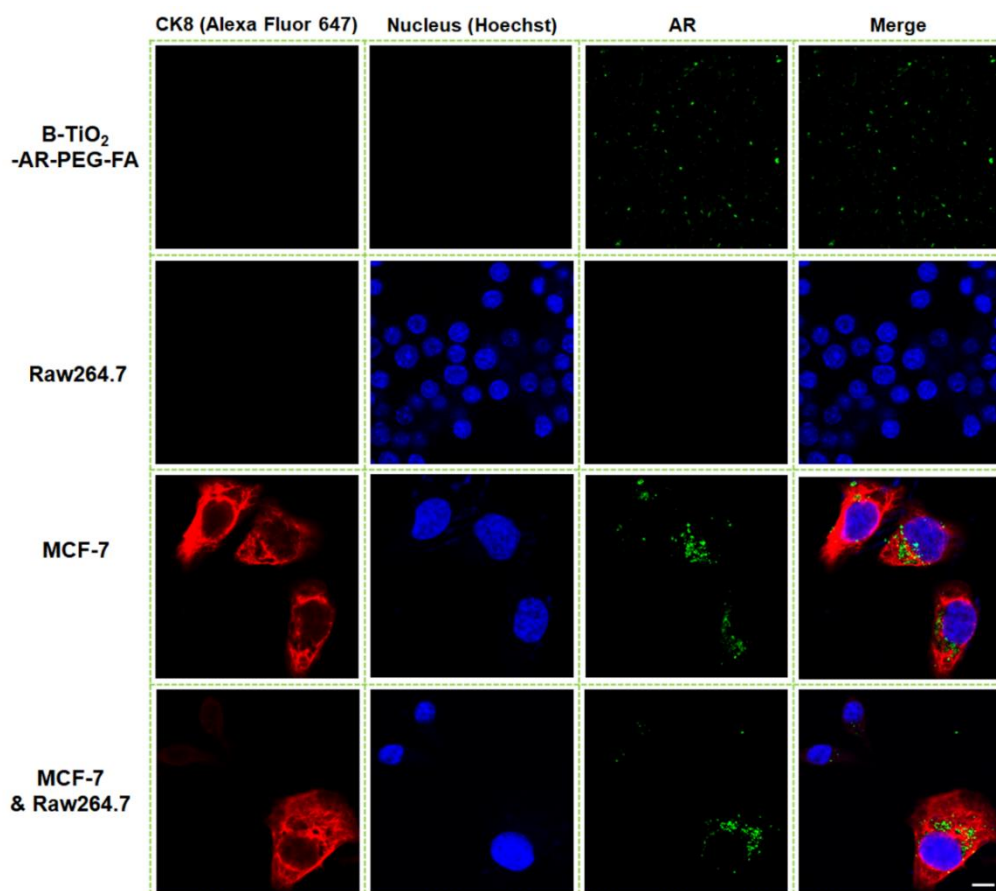


Figure 4.18: Fluorescent images of MCF-7 and Raw264.7 incubated with SERS biological probe. Scale bar: 10  $\mu$ m.

#### 4.5 Chapter conclusion

In summary, B-TiO<sub>2</sub>-AR-PEG-FA SERS bio-probes were successfully fabricated. Demonstrated by three cell lines of MCF-7 (FR positive), A549 and Raw264.7 (FR negative), SERS biological probes of B-TiO<sub>2</sub>-AR-PEG-FA could distinguish FR positive CTCs from FR negative cells by targeting FR on CTC membranes. Besides, through SERS-Fluorescence bimodal imaging method, B-TiO<sub>2</sub>-based SERS biological probe has also been verified with high

detection specificity and accuracy. However, the detection results were moderately inaccurate without isolation of CTCs, which should be improved in the future work.

## **Chapter 5 Combination method of microfilter and B-TiO<sub>2</sub>-based SERS biological probe on CTC detection**

### **5.1 Introduction**

In the fourth chapter, B-TiO<sub>2</sub> based SERS biological probe could successfully distinguish FR positive CTCs from FR negative cells by targeting FR on CTC membranes in the mixed cells. To improve the detection accuracy and applied it into clinical blood samples, microfluidic method was combined for blood pretreatment.

Microfluidics has been widely used in CTC detection based on the different biological properties and physical properties of CTCs compared with the counterpart of blood cells[208-210]. Microfiltration is one of label-free microfluidic methods which only depends on the size and deformability difference. It comes to the foreground in recent years benefiting from the ability of isolating both epithelial and mesenchymal phenotypes, which are more appropriate for analyses of tumor heterogeneity, and tumor drug resistance[208]. Although microfiltration can isolate CTCs with high capture efficiency and simplicity for operation within a few minutes[211, 212], there are still tens of thousands of WBCs remaining, which would disturb the accuracy and sensitivity of CTC detection. The traditional way to identify CTCs is fluorescent immunolabeling by characterizing the surface protein expression of CTCs. However, when using multiple fluorophore-conjugated

antibodies, the broadness of fluorescence spectrum and the cross-talking of fluorescent tags often confound the results[213]. Besides, the background noise was magnified in a microfluidic system, which might cause misrecognition of CTCs[214]. Therefore, it is necessary to develop a novel downstream analysis strategy of CTCs combined with microfluidic method.

In this chapter, the combination of SERS method and microfluidic method could advance both advantages of these two methods as well as overcome their own limitation. A novel strategy for in-situ isolating and detecting CTCs at single-cell resolution via combining microfilter CTC isolation method and SERS biological probe detection method was developed, as shown in Figure 5.1. First, the microfilter efficiently isolated CTCs from peripheral blood based on the size and deformability difference between CTCs and blood cells. Then, a FA-functionalized SERS biological probe has been designed to distinguish CTCs from the remaining WBCs by targeting the FA biomarkers on the CTC membranes. SERS-fluorescence bimodal imaging method verified high detection specificity of this strategy, and the limit of detection (LOD) of CTCs in rabbit blood can reach to 2 cells/mL. In addition, SERS results demonstrated that FR positive MCF-7 cancer cells could be captured efficiently with reliability and specificity compared to FR negative cancer cells (A549 and Raw264.7 cells). The whole processes were simple and efficient, which reduced detection time within 1.5 hours. Importantly, blood samples from

cancer patients have also been successfully detected based on the microfiltration isolation and B-TiO<sub>2</sub>-AR-PEG-FA SERS biological probe detection method.

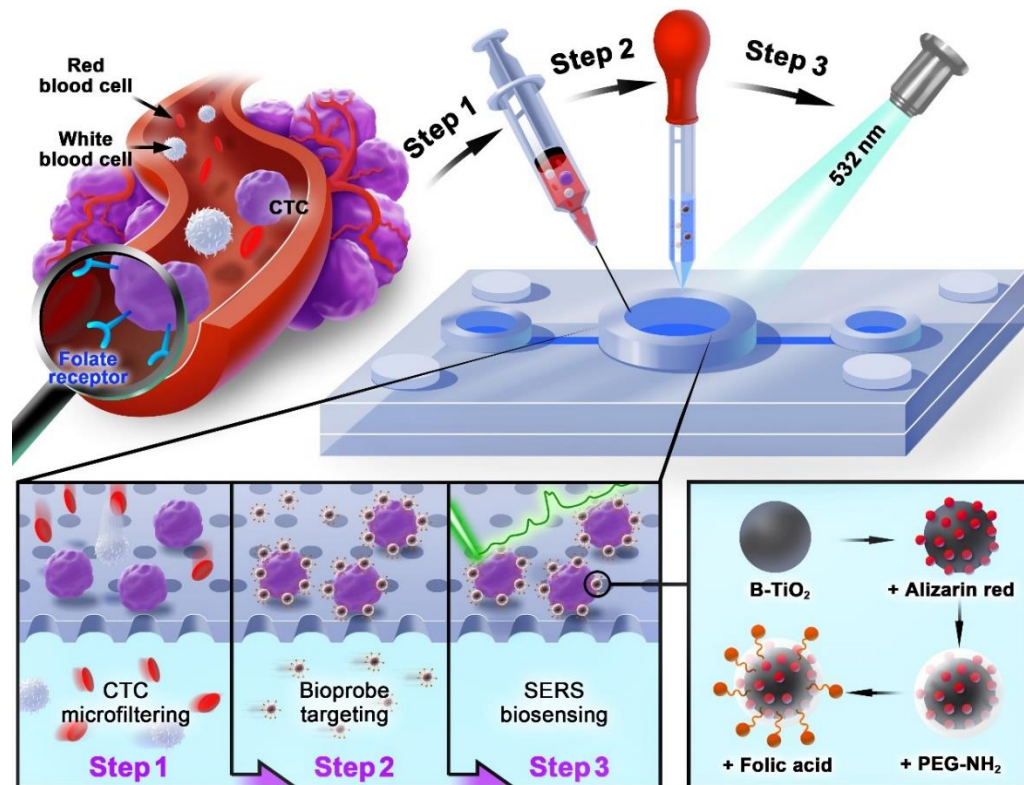


Figure 5.1: Scheme of CTC detection process.

## 5.2 Simulation of optimum capture flow rate in microfilter

The pathway of WBC passing through the micropore has been simulated as shown in Figure 5.2. The blue part represented blood and the red part represented WBCs. When the flow rate was 0.1 mL/min, WBC cannot pass through the micropore (Figure 5.2a). When the flow rate reached to 0.2 mL/min and 0.3 mL/min, WBC can pass through the micropore but might be retained within the micropore with tendency of sticking to the micropore wall

(Figure 5.2b and Figure 5.2c). When the flow rate was 0.4 mL/min, the cell can pass through the micropore with a complete structure and intact shape (Figure 5.2d). When the flow rate was 0.5 mL/min and 0.7 mL/min, the structure of WBC was slightly affected by flow condition after passing through the micropore (Figure 5.2e and Figure 5.2g). When the flow rate was 0.6 mL/min, the shape of WBC was slightly deformed (Figure 5.2f). When the flow rate was 0.8 mL/min, the cell was deformed significantly after passing through the micropore (Figure 5.2h), while the cell was completely damaged when the flow rate was 0.9 mL/min (Figure 5.2i). Therefore, the microfilter has the best WBC clearance performance when the flow rate was 0.4 mL/min.

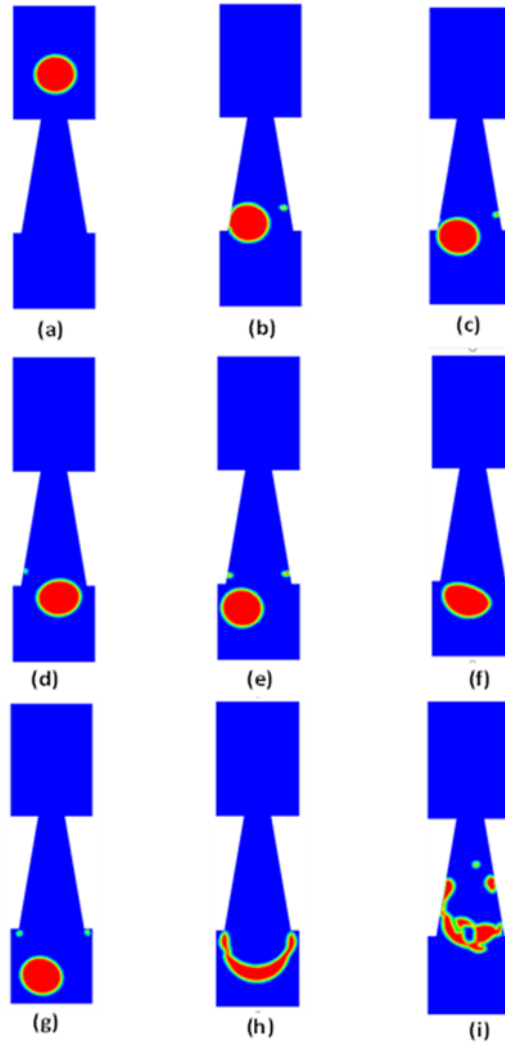


Figure 5.2: The effects of different blood flow rates on WBCs flowing through the pore of the microfilter. The blue part represents blood and the red part represents WBCs. a)  $u=0.1\text{mL}/\text{min}$ , b)  $u=0.2\text{mL}/\text{min}$ , c)  $u=0.4\text{mL}/\text{min}$ , d)  $u=0.4\text{mL}/\text{min}$ , e)  $u=0.5\text{ mL}/\text{min}$ , f)  $u= 0.6\text{mL}/\text{min}$ , g)  $u=0.7\text{ mL}/\text{min}$ , h)  $u=0.8\text{ mL}/\text{min}$ , i)  $u=0.9\text{ mL}/\text{min}$ .

Figure 5.3 shows the variations of volume in blue and contact pressure in red during the period when a WBC flows through the micropore. According to the red curve, the force applied on cell from the source side appears with axial

displacement from 2  $\mu\text{m}$  to 7.5  $\mu\text{m}$  approximately when there are interactions between the sides of contact pair. In this simulation, the contact of channel and cell is dealt with by setting a penalty function, which cause the deformation of cell described by the volume change shown by the blue curve. The stress on the cell shell from the inner structure is taken into consideration by setting a global equation to restrict the volume of cell to the initial volume. Therefore, the two peaks of volume variation correspond to the local maxima of contact pressure. It should be noted that the trends of the curves are not synchronous, but with a temporal difference since the value of the state variable is adapted in a way that the associated global equation is satisfied. Figure 5.4 shows the variations of volume and contact pressure during the period when a CTC flows through the micropore. As shown in Figure 5.4, the hysteresis of contact pressure is greater than that of WBC shown in Figure 5.3, which might be due to the volume of a CTC is larger than that of a WBC and the reaction of internal pressure is not so sensitive as CTC.

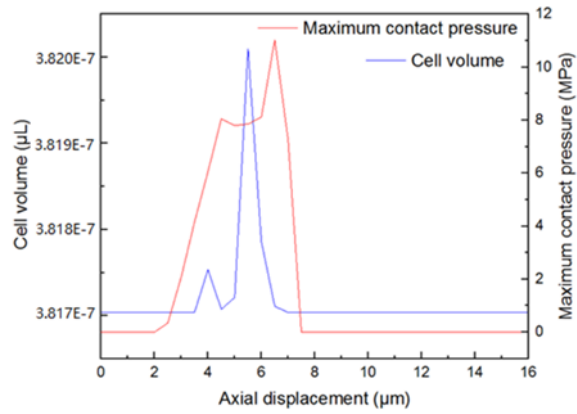


Figure 5.3: The variations in cell volume and maximum contact pressure with regards to the axial displacement of a WBC flowing through a micropore in the microfilter.

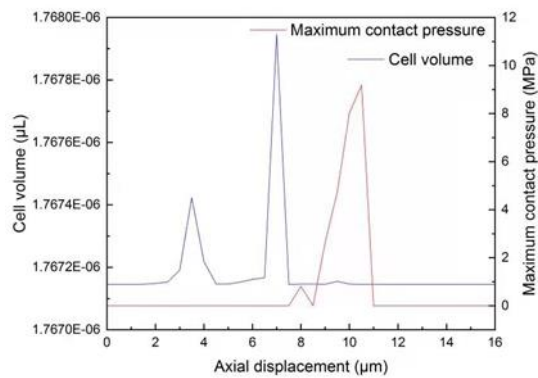


Figure 5.4: The variations in cell volume and maximum contact pressure with regards to the axial displacement of a CTC flowing through a micropore in the microfilter.

### 5.3 Sensitivity, specificity, and capture assay of microfilter combined SERS spectral detection method in blood

To explore the clinical utility of microfilter combined with SERS spectral method, clinical tumor blood model was built to carry out cancer cell capture

and detection studies. The clinical tumor blood model was prepared by mixing 1-100 cells/mL MCF-7 cancer cells into rabbit blood. The WBC clearance could reach 96% by counting the cell concentration before and after filtering. The LOD of this strategy in rabbit blood was 2 cells/mL as shown in Figure 5.5b. Figure 5.5a demonstrated the schematic diagram of the CTC detection process via microfilter and SERS biological probe, which was composed of CTC microfiltering, biological probe targeting, and SERS detection. The SERS spectral of 9 MCF-7 cells after isolation and targeted by SERS biological probe was shown in Figure 5.5d, and SERS signal of the cancer cells exhibited relatively high uniform, illustrating efficient SERS detection of CTC in peripheral blood sample based on effective microfluidic separation technology. Then, the captured cancer cells were further verified by CK8 and Hoechst (Figure 5.5c), Fluorescent image results indicated that the accuracy of this strategy, which showed that microfilter combined with SERS spectral strategy has huge application potential in clinical application.

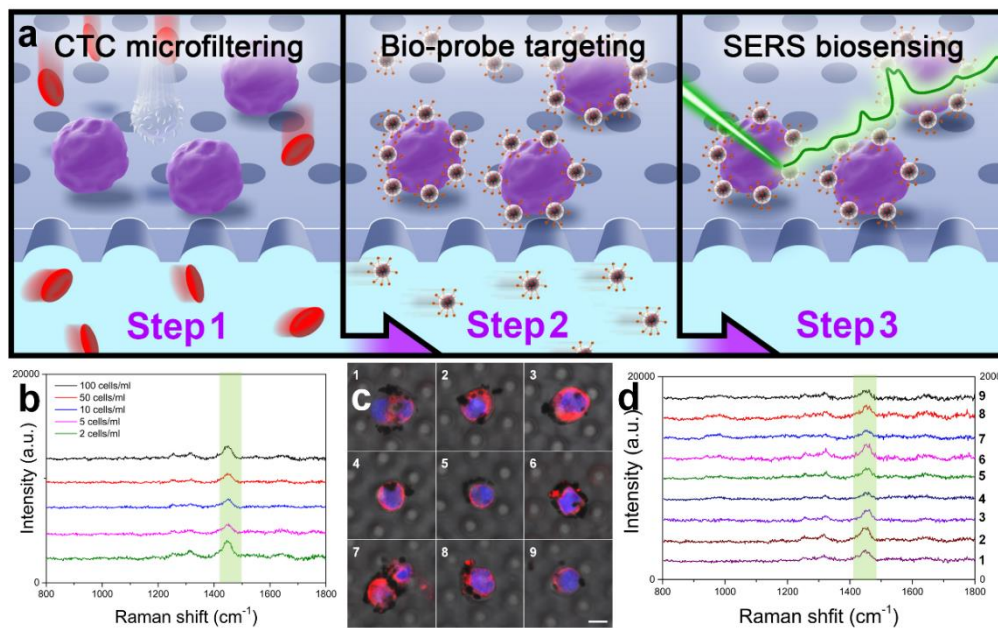


Figure 5.5: a) Schematic illustration of CTC detection steps. b) LOD of CTC based on the method of combining microfilter and SERS method. c) Fluorescent images of captured cells. Scale bar: 10  $\mu\text{m}$ . d) SERS spectral of the captured cancer cells. Laser wavelength: 532 nm; power: 0.12 mW; lens: 50 $\times$  objective.

#### 5.4 Application in clinical tumor blood detection

The strategy of microfluidic isolation process and B-TiO<sub>2</sub>-AR-PEG-FA SERS biological probe has been successfully leveraged to detect clinical peripheral blood samples from six breast cancer patients and two health people. The SERS spectra signal acquired from six blood samples of breast cancer patients were unambiguous and reproducible (Figure 5.6), while there was no SERS signal observed in two health people (Figure 5.7). The SERS spectra Cancer patient blood samples and health people blood samples were carefully

confirmed by collecting 3 different laser points on the cell examined under a microscope. Besides, the time of completing the whole strategy was less than 1.5 hours. The results illustrated that the CTCs from clinical breast cancer patients can be accurately distinguished via microfilter combined SERS spectral detection method. This novel cell isolation and detection method could be served as an efficient platform utilized in cancer early screening and diagnosis, as well as postoperative evaluation, making great contributions to precision medicine.

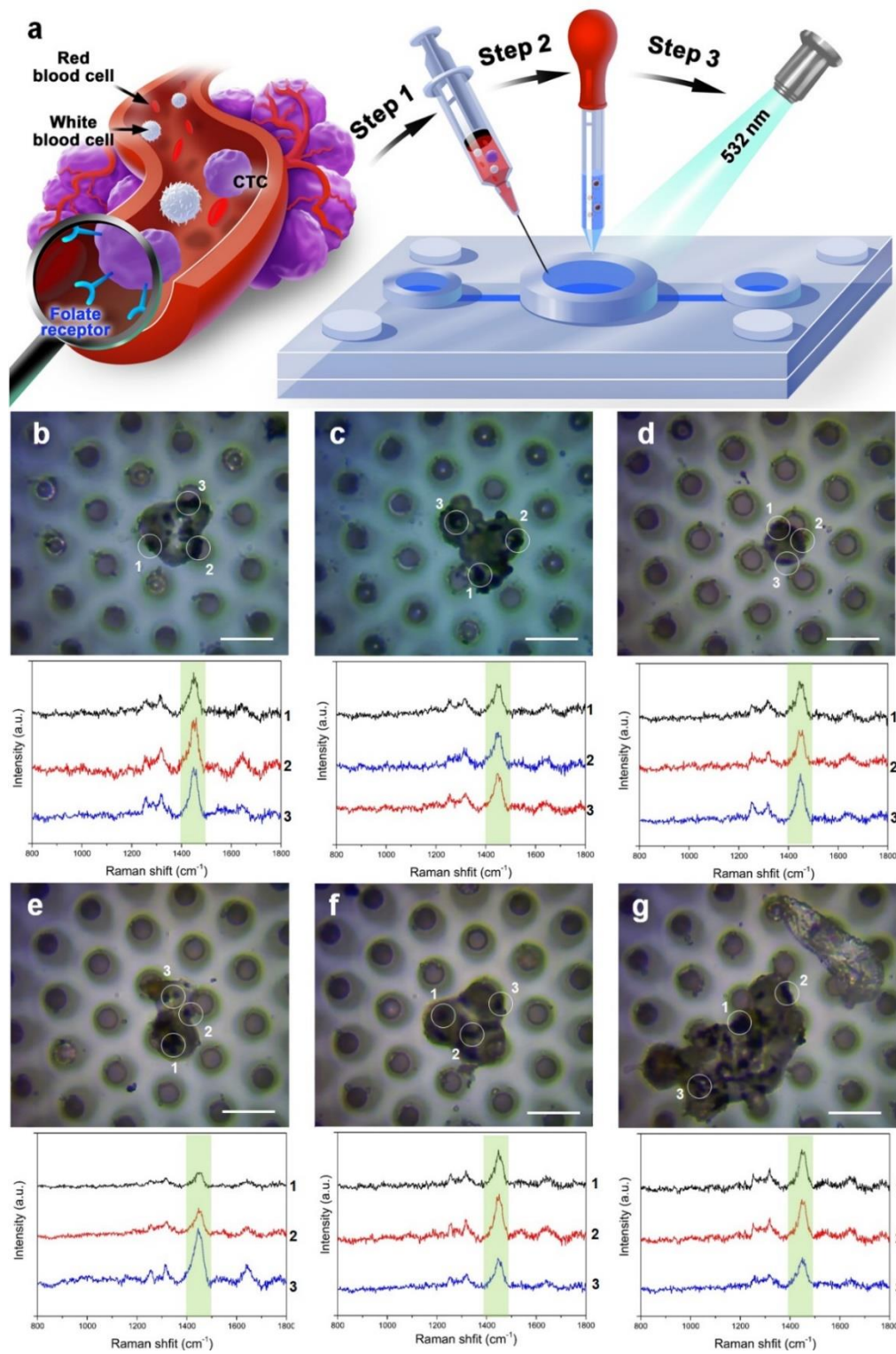


Figure 5.6: Schematic illustration of CTC detection based on microfilter and SERS spectra. (b-g) Optical image and SERS spectral of the captured cancer cells from six breast cancer patients. Scale bar: 20  $\mu\text{m}$ . Laser wavelength: 532 nm; power: 0.12 mW; lens: 50 $\times$  objective.

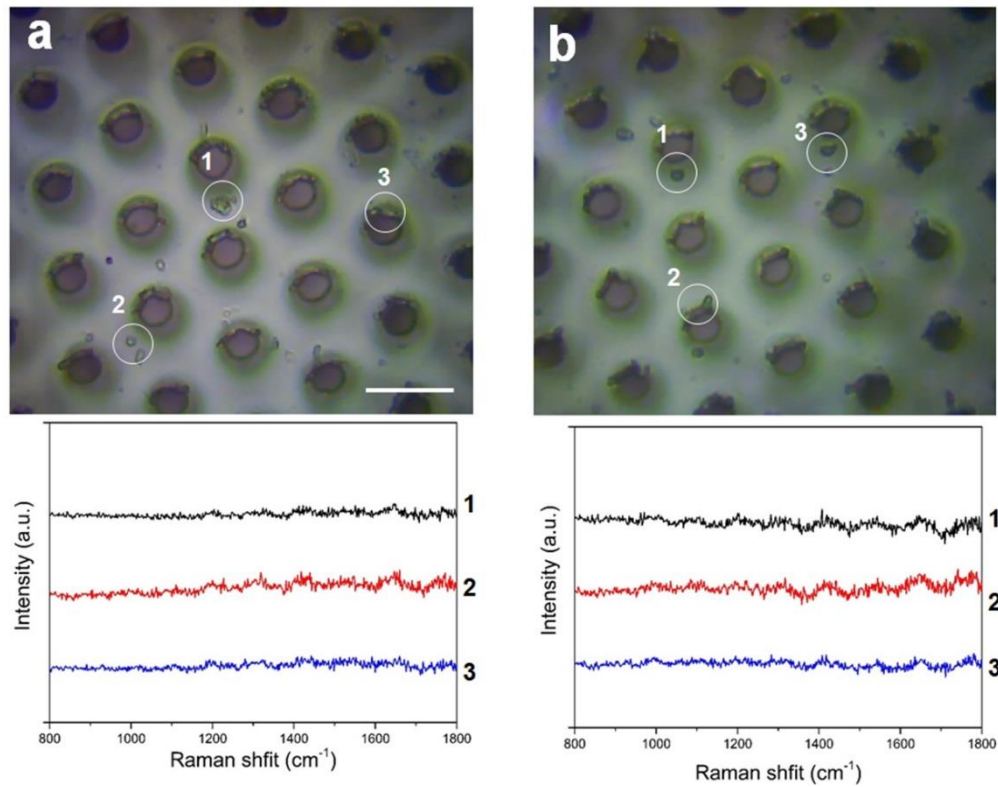


Figure 5.7: Optical image and SERS spectral of captured cells from healthy people. Scale bar: 20  $\mu\text{m}$ . Laser wavelength: 532 nm; power: 0.12 mW; lens: 50 $\times$  objective.

### 5.5 Chapter conclusion

In summary, an integrated CTC detection strategy based on microfilter, and SERS detection method was successfully developed for in-situ isolating and recognizing CTCs at single-cell resolution. For CTC isolation, it could reach to 96% WBC clearance by adjusting pulling speed in microfilter and reduce the complexity of blood environment. The low purity and specificity of microfilter were also solved by combining high-sensitivity SERS spectra detection in this

study. Demonstrated by three cell lines of MCF-7 (FR positive), A549 and Raw264.7 (FR negative), SERS biological probes of B-TiO<sub>2</sub>-AR-PEG-FA could distinguish FR positive CTCs from peripheral blood cells efficiently by targeting FR on CTC membranes and ruling out false positive interference of WBCs with reliability and specificity. Besides, through SERS-Fluorescence bimodal imaging method, B-TiO<sub>2</sub>-based SERS biological probe has also been verified with high detection specificity and accuracy. Compared to the traditional fluorescent immunolabeling method, SERS biological probe can distinguish cancer cells from blood cells with high intensity and sensitivity avoiding the influence of background noise. Besides, the use of microfilter improved the efficacy of CTC isolation compared to the traditional density gradient centrifugation method. Benefiting by these advantages, the combination of SERS method and microfilter enhanced the detection efficiency and veracity, which reduced the detection time within 1.5 hours and make the LOD of detection reach to 2 cells/mL. Though the SERS biological probe in this paper was only suitable for FR positive CTCs, it still has great practical values because most of cancer cells are FR overexpressed. These features also facilitated successful CTC detection in several clinical cancer patient bloods which illustrates that the integration of microfluidic isolation and SERS detection was worth to be further developed and a promising tool for diagnosis and treatment of cancer.

## **Chapter 6 Conclusion and future perspective**

### **6.1 Conclusion**

In summary, three strategies have been successfully carried for CTC detection in clinical blood samples. In the first strategy, gold-iron oxide composite nanoparticles were selected as SERS substrate. SPION@Au-MBA-rBSA-FA SERS biological probes were reproduced according to the previous work. In this thesis, SPION@Au-MBA-rBSA-FA SERS biological probes were applied into clinical blood sample detection. 32 blood samples from cancer patients and 3 blood samples from healthy people were detected. Although the results showed good specificity and separation efficacy, there are still some limitations to be overcome. For examples, density gradient centrifugation as blood pretreatment method may cause loss of targeted cells and redundant SERS biological probes could not be effectively removed, which will cause false negative results and false positive results, respectively. Besides, hot-spot effect between noble nanoparticles might also disturb judgment of results. In the second strategy, black B-TiO<sub>2</sub> NPs were used as SERS substrate due to its high spectral stability and reproducibility, strong anti-interference ability, and selective SERS enhancement of target molecules. The B-TiO<sub>2</sub>-AR-PEG-FA biological probe was composed by a crystal-amorphous core-shell B-TiO<sub>2</sub> SERS substrate, Raman reporter alizarin red (AR) molecule, a thin NH<sub>2</sub>-PEG2000-COOH (PEG) layer to improve the dispersion of biological probe, and FA to specifically recognize folate receptor (FR) on cancer cell membrane.

Besides, abundant amino group of the PEG layer can provide sufficient binding sites for FA coupling, which is benefit for improving the detection specificity and accuracy of B-TiO<sub>2</sub> based biological probe. It could accurately target FR positive MCF-7 cancer cells from FR negative cancer cells (A549 and Raw264.7 cells). In the third strategy, microfluidic method was added to isolate CTCs before SERS detection. In this strategy, the low purity and specificity of microfilter could be solved by combining high-sensitivity SERS spectra detection, while the microfilter could reduce interference of blood background during SERS detection. Besides, SERS-fluorescence bimodal imaging method verified high detection specificity of this strategy, and the limit of detection (LOD) of CTCs in rabbit blood can reach to 2 cells/mL. Compared to pretreatment of blood by density gradient centrifugation, the whole processes of combined method was simple and efficient, which reduced detection time within 1.5 hours. Compared to the first strategy, there was less undesired peak in Raman spectral, which made results easier to be determined and with more accuracy. These results illustrates that both of microfluidic isolation and SERS detection could open new paths for liquid biopsy.

## **6.2 Future perspective**

With the rapid development of material science and processing technology, microfluidics has obtained breakthrough progress. Researchers are no longer satisfied with chemical reactions on the microfluidic chip, but also testing

various analytes with microfluidics. In recent years, optical and spectroscopic technology has been developed as a high-sensitive, rapid, efficient, and non-destructive detection and imaging method, in which SERS has become one of the most commonly used spectral methods. SERS method has been widely applied in biosensor.

The combination of SERS method and microfluidic method has become a new research trend. SERS method can be used to detect ultra-low concentration samples within microfluidic channel while the multi-channel design of microfluidic chip can facilitate multivariate SERS detection. SERS method can provide excellent analysis method for microflow platform. Besides, the SERS substrate made by microfluidics can solve the limitations of irregular fluctuation of SERS signal in solutions, and thus greatly improving the repeatability and reliability of detection. The combination of SERS and microfluidic chips has provided many new opportunities for the development of both technologies, and their complementarity has also solved their respective problems, laying a solid foundation for multifunctional SERS Lab-on-Chip systems. There is also a promising of the opportunity in biological, chemical detection, medical diagnosis, and other fields.

Although the microfluidic SERS detection chip has made remarkable research progress, the detection specificity and repeatability, the improvement of chip

multi-functionality and integration are the development directions and research emphases in the future, in particular of the direct detection of actual clinical biological samples. The real clinical samples, such as patient blood, are very complex, containing rich proteins, DNA, and other elements. These biomacromolecules may possess non-specific noise signals during SERS detection, which may result in false positive or false negative results and seriously affect the reliability of detection results. Therefore, for real samples, the specificity of microfluidic SERS detection chip is particularly important. Generally, the specificity of microfluidic SERS detection chip can be solved from two aspects. First, the biological functional modification of SERS substrate or probe can be optimized to improve the selectivity and accuracy of substrate or probe in recognizing the analyte; second, the number of functional units of analyte screening can be increased, such as physical size screening or chemical ligand recognition screening, to eliminate non-specific interference of other substances as much as possible. If microfluidic SERS detection chip can detect real complex biological samples with high accuracy, it will greatly promote clinical diagnosis and treatment. In addition, low-cost automatic microfluidic SERS detection chip is also one of the key objectives. The focus of research is to reduce the production cost of the chip keeping the perfect sensing and analysis functions. Low-cost microfluidic SERS chip has very important social value and practical significance for biochemical detection, such as disease survey and environmental monitoring, in underdeveloped areas.

Besides, multi-dimensional analysis of CTCs has been a newly emerging research area, instead of restricting to the detection of single gene or protein. As mentioned above, CTCs are heterogeneous in phenotype. Different cellular subpopulations may exist in individual tumors and some of them have shown to be responsible for initiating cancer metastasis and accelerating cancer development. Additionally, during cancer progression and medication, the phenotypic status of CTCs could dynamically evolve. Therefore, it is of great importance to monitor the phenotypic distribution of CTCs at the resolution of individual cells rather than acquiring an average information, which could be more adaptable to predict disease progression and therapeutic efficiency. In addition, the heterogeneity of CTCs is also reflected among different cancer-bearing patients. For example, breast cancer has at least three subtypes categorized according to the cancer cell molecular profiles. Each of these subtypes has their specific strategies for treatment and different risks of disease progression. To some extent, the knowledge of phenotype status in cancer cells could determine the therapy and therapeutic outcomes. Consequently, technologies for profiling and categorizing CTCs on the basis of the phenotypic information at single-cell resolution are in great demand.

In the future, SERS and microfluidic chip technology will be further developed. For example, the integration of laser, spectrometer and other devices on the chip will play a greater role, making a great contribution to the improvement of

on-site real-time detection technology, benefiting the development of life health science, biomedicine and other aspects. It can be envisioned that with the continuous improvement of functions and performance, integrated and automated SERS Lab-on-Chip method will inevitably become a very important technology in the field of biosensor detection for cancer diagnostics related biomedical applications.

## References

1. Sung, H., et al., *Global Cancer Statistics 2020: GLOBOCAN Estimates of Incidence and Mortality Worldwide for 36 Cancers in 185 Countries*. CA: A Cancer Journal for Clinicians, 2021. **71**(3): p. 209-249.
2. Shulman, L.N., et al., *Breast Cancer in Developing Countries: Opportunities for Improved Survival*. Journal of Oncology, 2010. **2010**: p. 595167.
3. Stockton, D., et al., *Retrospective study of reasons for improved survival in patients with breast cancer in East Anglia: earlier diagnosis or better treatment?* BMJ, 1997. **314**(7079): p. 472.
4. Pontén, J., et al., *Strategies for global control of cervical cancer*. International Journal of Cancer, 1995. **60**(1): p. 1-26.
5. Richards, M.A., et al., *Influence of delay on survival in patients with breast cancer: a systematic review*. The Lancet, 1999. **353**(9159): p. 1119-1126.
6. Yu, L., et al., *Advances of lab-on-a-chip in isolation, detection and post-processing of circulating tumour cells*. Lab on a Chip, 2013. **13**(16): p. 3163-3182.
7. Lin, H.K., et al., *Portable Filter-Based Microdevice for Detection and Characterization of Circulating Tumor Cells*. Clinical Cancer Research, 2010. **16**(20): p. 5011-5018.
8. Yu, M., et al., *Circulating tumor cells: approaches to isolation and characterization*. Journal of Cell Biology, 2011. **192**(3): p. 373-382.
9. Girotti, M.R., et al., *Application of Sequencing, Liquid Biopsies, and Patient-Derived Xenografts for Personalized Medicine in Melanoma*. Cancer Discovery, 2016. **6**(3): p. 286-299.
10. Quail, D.F. and J.A. Joyce, *Microenvironmental regulation of tumor progression and metastasis*. Nature Medicine, 2013. **19**(11): p. 1423-1437.
11. Yun, S., et al., *Design of Magnetically Labeled Cells (Mag-Cells) for in Vivo Control of Stem Cell Migration and Differentiation*. Nano Letters, 2018. **18**(2): p. 838-845.
12. Meng, S., et al., *Circulating Tumor Cells in Patients with Breast Cancer Dormancy*. Clinical Cancer Research, 2004. **10**(24): p. 8152-8162.
13. Liu, H., et al., *The biological and clinical importance of epithelial–mesenchymal transition in circulating tumor cells*. Journal of Cancer Research and Clinical Oncology, 2015. **141**(2): p. 189-201.
14. Gong, C., et al., *Potentiated DNA Damage Response in Circulating Breast Tumor Cells Confers Resistance to Chemotherapy\**. Journal of Biological Chemistry, 2015. **290**(24): p. 14811-14825.
15. Onstenk, W., et al., *Towards a personalized breast cancer treatment approach guided by circulating tumor cell (CTC) characteristics*. Cancer Treatment Reviews, 2013. **39**(7): p. 691-700.
16. Gourdin, T. and G. Sonpavde, *Utility of cell-free nucleic acid and circulating tumor cell analyses in prostate cancer*. Asian Journal of Andrology, 2018. **20**(3): p. 230-237.
17. Cho, H., et al., *Microfluidic technologies for circulating tumor cell isolation*. Analyst, 2018. **143**(13): p. 2936-2970.

18. Shapiro, H.M., et al., *Combined blood cell counting and classification with fluorochrome stains and flow instrumentation*. Journal of Histochemistry & Cytochemistry, 1976. **24**(1): p. 396-401.
19. Park, S., et al., *Morphological Differences between Circulating Tumor Cells from Prostate Cancer Patients and Cultured Prostate Cancer Cells*. Plos One, 2014. **9**(1): p. e85264.
20. Stott, S.L., et al., *Isolation of circulating tumor cells using a microvortex-generating herringbone-chip*. Proceedings of the National Academy of Sciences, 2010. **107**(43): p. 18392-18397.
21. Ozkumur, E., et al., *Inertial Focusing for Tumor Antigen Dependent and Independent Sorting of Rare Circulating Tumor Cells*. Science Translational Medicine, 2013. **5**(179): p. 179ra47
22. Gertler, R., et al. *Detection of Circulating Tumor Cells in Blood Using an Optimized Density Gradient Centrifugation*. Molecular Staging Of Cancer 2003. **162**: p. 149-155.
23. Shao, C., et al., *Detection of Live Circulating Tumor Cells by a Class of Near-Infrared Heptamethine Carbocyanine Dyes in Patients with Localized and Metastatic Prostate Cancer*. Plos One, 2014. **9**(2): p. e88967.
24. Ligthart, S.T., et al., *Circulating Tumor Cells Count and Morphological Features in Breast, Colorectal and Prostate Cancer*. Plos One, 2013. **8**(6): p. e67148.
25. Vona, G., et al., *Isolation by Size of Epithelial Tumor Cells: A New Method for the Immunomorphological and Molecular Characterization of Circulating Tumor Cells*. The American Journal of Pathology, 2000. **156**(1): p. 57-63.
26. Zheng, S., et al., *Membrane microfilter device for selective capture, electrolysis and genomic analysis of human circulating tumor cells*. Journal of Chromatography A, 2007. **1162**(2): p. 154-161.
27. Tang, Y.D., et al., *Microfluidic device with integrated microfilter of conical-shaped holes for high efficiency and high purity capture of circulating tumor cells*. Scientific Reports, 2014. **4**: p 6052.
28. Sobiepanek, A., et al., *AFM and QCM-D as tools for the distinction of melanoma cells with a different metastatic potential*. Biosensors and Bioelectronics, 2017. **93**: p. 274-281.
29. Hochmuth, R.M., *Micropipette aspiration of living cells*. Journal of Biomechanics, 2000. **33**(1): p. 15-22.
30. Guck, J., et al., *The Optical Stretcher: A Novel Laser Tool to Micromanipulate Cells*. Biophysical Journal, 2001. **81**(2): p. 767-784.
31. Otto, O., et al., *Real-time deformability cytometry: on-the-fly cell mechanical phenotyping*. Nature Methods, 2015. **12**(3): p. 199-202.
32. Xu, W.W., et al., *Cell Stiffness Is a Biomarker of the Metastatic Potential of Ovarian Cancer Cells*. Plos One, 2012. **7**(10): p. 12.
33. Lee, Y.J., D. Patel, and S. Park, *Local Rheology of Human Neutrophils Investigated Using Atomic Force Microscopy*. International Journal of Biological Sciences, 2011. **7**(1): p. 102-111.
34. Watanabe, T., et al., *Higher Cell Stiffness Indicating Lower Metastatic Potential in*

- B16 Melanoma Cell Variants and in (-) Epigallocatechin Gallate-Treated Cells.* Journal of Cancer Research and Clinical Oncology, 2012. **138**(5): p. 859-866.
35. Chowdhury, H.H., S. Grilc, And R. Zorec, *Correlated ATP-Induced Changes in Membrane Area and Membrane Conductance in Single Rat Adipocytes.* Annals of the New York Academy of Sciences, 2005. **1048**(1): p. 281-286.
  36. Han, A., L. Yang, and A.B. Frazier, *Quantification of the Heterogeneity in Breast Cancer Cell Lines Using Whole-Cell Impedance Spectroscopy.* Clinical Cancer Research, 2007. **13**(1): p. 139-143.
  37. Dobrzyńska, I., E. Skrzydlewska, and Z.A. Figaszewski, *Changes in Electric Properties of Human Breast Cancer Cells.* The Journal of Membrane Biology, 2013. **246**(2): p. 161-166.
  38. Kang, Y.B. and K. Pantel, *Tumor Cell Dissemination: Emerging Biological Insights from Animal Models and Cancer Patients.* CANCER CELL, 2013. **23**(5): p. 573-581.
  39. Tanaka, F., et al., *Circulating Tumor Cell as a Diagnostic Marker in Primary Lung Cancer.* Clinical Cancer Research, 2009. **15**(22): p. 6980-6986.
  40. Pantel, K., et al., *Circulating Epithelial Cells in Patients with Benign Colon Diseases.* Clinical Chemistry, 2012. **58**(5): p. 936-940.
  41. Allard, W.J., et al., *Tumor Cells Circulate in the Peripheral Blood of All Major Carcinomas but not in Healthy Subjects or Patients With Nonmalignant Diseases.* Clinical Cancer Research, 2004. **10**(20): p. 6897-6904.
  42. Ilie, M., et al., *Current challenges for detection of circulating tumor cells and cell-free circulating nucleic acids, and their characterization in non-small cell lung carcinoma patients. What is the best blood substrate for personalized medicine?* Annals of Translational Medicine, 2014. **2**(11): p. 3.
  43. Cristofanilli, M., et al., *Circulating Tumor Cells, Disease Progression, and Survival in Metastatic Breast Cancer.* New England Journal of Medicine, 2004. **351**(8): p. 781-791.
  44. Cohen, S.J., et al., *Relationship of Circulating Tumor Cells to Tumor Response, Progression-Free Survival, and Overall Survival in Patients With Metastatic Colorectal Cancer.* Journal of Clinical Oncology, 2008. **26**(19): p. 3213-3221.
  45. de Bono, J.S., et al., *Circulating Tumor Cells Predict Survival Benefit from Treatment in Metastatic Castration-Resistant Prostate Cancer.* Clinical Cancer Research, 2008. **14**(19): p. 6302-6309.
  46. Goldkorn, A., et al., *Circulating tumor cell telomerase activity as a prognostic marker for overall survival in SWOG 0421: A phase III metastatic castration resistant prostate cancer trial.* International Journal of Cancer, 2015. **136**(8): p. 1856-1862.
  47. Budd, G.T., et al., *Circulating Tumor Cells versus Imaging—Predicting Overall Survival in Metastatic Breast Cancer.* Clinical Cancer Research, 2006. **12**(21): p. 6403-6409.
  48. Paterlini-Brechot, P. and N.L. Benali, *Circulating tumor cells (CTC) detection: Clinical impact and future directions.* Cancer Letters, 2007. **253**(2): p. 180-204.
  49. Luan, C.X., et al., *Folic Acid-Functionalized Hybrid Photonic Barcodes for Capture and Release of Circulating Tumor Cells.* Acs Applied Materials & Interfaces, 2018.

- 10**(25): p. 21206-21212.
50. Shen, Z.Y., A.G. Wu, and X.Y. Chen, *Current detection technologies for circulating tumor cells*. Chemical Society Reviews, 2017. **46**(8): p. 2038-2056.
  51. Jansson, S., et al., *Prognostic impact of circulating tumor cell apoptosis and clusters in serial blood samples from patients with metastatic breast cancer in a prospective observational cohort*. BMC Cancer, 2016. **16**(1): p. 433.
  52. Langer-Safer, P.R., M. Levine, and D.C. Ward, *Immunological method for mapping genes on Drosophila polytene chromosomes*. Proceedings of the National Academy of Sciences, 1982. **79**(14): p. 4381-4385.
  53. Dinish, U.S., et al., *Actively Targeted In Vivo Multiplex Detection of Intrinsic Cancer Biomarkers Using Biocompatible SERS Nanotags*. Scientific Reports, 2014. **4**: p 4075.
  54. Zare, R.N. and S. Kim, *Microfluidic Platforms for Single-Cell Analysis*. Annual Review of Biomedical Engineering, 2010. **12**(1): p. 187-201.
  55. Hajba, L. and A. Guttman, *Circulating tumor-cell detection and capture using microfluidic devices*. TrAC Trends in Analytical Chemistry, 2014. **59**: p. 9-16.
  56. Lu, Y.-T., et al., *NanoVelcro Chip for CTC enumeration in prostate cancer patients*. Methods, 2013. **64**(2): p. 144-152.
  57. Nagrath, S., et al., *Isolation of rare circulating tumour cells in cancer patients by microchip technology*. Nature, 2007. **450**(7173): p. 1235-1239.
  58. Wang, S., et al., *Highly Efficient Capture of Circulating Tumor Cells by Using Nanostructured Silicon Substrates with Integrated Chaotic Micromixers*. Angewandte Chemie International Edition, 2011. **50**(13): p. 3084-3088.
  59. Lin, M., et al., *Nanostructure Embedded Microchips for Detection, Isolation, and Characterization of Circulating Tumor Cells*. Accounts of Chemical Research, 2014. **47**(10): p. 2941-2950.
  60. Hou, S., et al., *Polymer Nanofiber-Embedded Microchips for Detection, Isolation, and Molecular Analysis of Single Circulating Melanoma Cells*. Angewandte Chemie International Edition, 2013. **52**(12): p. 3379-3383.
  61. Li, W., et al., *3D Graphene Oxide-Polymer Hydrogel: Near-Infrared Light-Triggered Active Scaffold for Reversible Cell Capture and On-Demand Release*. Advanced Materials, 2013. **25**(46): p. 6737-6743.
  62. Shin, D.-S., et al., *Photodegradable Hydrogels for Capture, Detection, and Release of Live Cells*. Angewandte Chemie International Edition, 2014. **53**(31): p. 8221-8224.
  63. Camci-Unal, G., et al., *Surface-modified hyaluronic acid hydrogels to capture endothelial progenitor cells*. Soft Matter, 2010. **6**(20): p. 5120-5126.
  64. Lv, S.-W., et al., *Near-Infrared Light-Responsive Hydrogel for Specific Recognition and Photothermal Site-Release of Circulating Tumor Cells*. ACS Nano, 2016. **10**(6): p. 6201-6210.
  65. Saliba, A.-E., et al., *Microfluidic sorting and multimodal typing of cancer cells in self-assembled magnetic arrays*. Proceedings of the National Academy of Sciences, 2010. **107**(33): p. 14524-14529.
  66. Kwak, B., et al., *Selective isolation of magnetic nanoparticle-mediated*

- heterogeneity subpopulation of circulating tumor cells using magnetic gradient based microfluidic system.* Biosensors and Bioelectronics, 2017. **88**: p. 153-158.
67. Santhosh, P.B. and N.P. Ulrich, *Multifunctional superparamagnetic iron oxide nanoparticles: Promising tools in cancer theranostics.* Cancer Letters, 2013. **336**(1): p. 8-17.
  68. Sato, K., *Microdevice in Cellular Pathology: Microfluidic Platforms for Fluorescence *in situ* Hybridization and Analysis of Circulating Tumor Cells.* Analytical Sciences, 2015. **31**(9): p. 867-873.
  69. Devadhasan, J.P. and S. Kim, *An ultrasensitive method of real time pH monitoring with complementary metal oxide semiconductor image sensor.* Analytica Chimica Acta, 2015. **858**: p. 55-59.
  70. Navin, N., et al., *Tumour evolution inferred by single-cell sequencing.* Nature, 2011. **472**(7341): p. 90-94.
  71. Zhao, M., et al., *An Automated High-Throughput Counting Method for Screening Circulating Tumor Cells in Peripheral Blood.* Analytical Chemistry, 2013. **85**(4): p. 2465-2471.
  72. Song, Y., et al., *Enrichment and single-cell analysis of circulating tumor cells.* Chemical Science, 2017. **8**(3): p. 1736-1751.
  73. Harouaka, R.A., et al., *Flexible Micro Spring Array Device for High-Throughput Enrichment of Viable Circulating Tumor Cells.* Clinical Chemistry, 2014. **60**(2): p. 323-333.
  74. Louterback, K., et al., *Deterministic separation of cancer cells from blood at 10 mL/min.* AIP Advances, 2012. **2**(4): p. 042107.
  75. Bhagat, A.A.S., S.S. Kuntaegowdanahalli, and I. Papautsky, *Continuous particle separation in spiral microchannels using dean flows and differential migration.* Lab on a Chip, 2008. **8**(11): p. 1906-1914.
  76. Warkiani, M.E., et al., *An ultra-high-throughput spiral microfluidic biochip for the enrichment of circulating tumor cells.* Analyst, 2014. **139**(13): p. 3245-3255.
  77. Warkiani, M.E., et al., *Ultra-fast, label-free isolation of circulating tumor cells from blood using spiral microfluidics.* Nature Protocols, 2016. **11**(1): p. 134-148.
  78. Renier, C., et al., *Label-free isolation of prostate circulating tumor cells using Vortex microfluidic technology.* npj Precision Oncology, 2017. **1**(1): p. 15.
  79. Sollier, E., et al., *Size-selective collection of circulating tumor cells using Vortex technology.* Lab on a Chip, 2014. **14**(1): p. 63-77.
  80. Chiu, T.-K., et al., *Application of optically-induced-dielectrophoresis in microfluidic system for purification of circulating tumour cells for gene expression analysis- Cancer cell line model.* Scientific Reports, 2016. **6**(1): p. 32851.
  81. Alazzam, A., B. Mathew, and F. Alhammadi, *Novel microfluidic device for the continuous separation of cancer cells using dielectrophoresis.* Journal of Separation Science, 2017. **40**(5): p. 1193-1200.
  82. Petersson, F., et al., *Continuous separation of lipid particles from erythrocytes by means of laminar flow and acoustic standing wave forces.* Lab on a Chip, 2005. **5**(1): p. 20-22.

83. Li, P., et al., *Acoustic separation of circulating tumor cells*. Proceedings of the National Academy of Sciences, 2015. **112**(16): p. 4970-4975.
84. Augustsson, P., et al., *Microfluidic, Label-Free Enrichment of Prostate Cancer Cells in Blood Based on Acoustophoresis*. Analytical Chemistry, 2012. **84**(18): p. 7954-7962.
85. Wu, M., et al., *Circulating Tumor Cell Phenotyping via High-Throughput Acoustic Separation*. Small, 2020. **16**(34): p. 2004438.
86. Lin, B.K., et al., *Highly selective biomechanical separation of cancer cells from leukocytes using microfluidic ratchets and hydrodynamic concentrator*. Biomicrofluidics, 2013. **7**(3): p. 034114.
87. Song, Y., et al., *Inside Cover: Bioinspired Engineering of a Multivalent Aptamer-Functionalized Nanointerface to Enhance the Capture and Release of Circulating Tumor Cells (Angew. Chem. Int. Ed. 8/2019)*. Angewandte Chemie International Edition, 2019. **58**(8): p. 2158-2158.
88. Ahmed, M.G., et al., *Isolation, Detection, and Antigen-Based Profiling of Circulating Tumor Cells Using a Size-Dictated Immunocapture Chip*. Angewandte Chemie International Edition, 2017. **56**(36): p. 10681-10685.
89. Jack, R.M., et al., *Ultra-Specific Isolation of Circulating Tumor Cells Enables Rare-Cell RNA Profiling*. Advanced Science, 2016. **3**(9): p. 1600063.
90. Kang, Y.-T., et al., *Epithelial and mesenchymal circulating tumor cell isolation and discrimination using dual-immunopatterned device with newly-developed anti-63B6 and anti-EpCAM*. Sensors and Actuators B: Chemical, 2018. **260**: p. 320-330.
91. Fleischmann, M., P.J. Hendra, and A.J. McQuillan, *Raman spectra of pyridine adsorbed at a silver electrode*. Chemical Physics Letters, 1974. **26**(2): p. 163-166.
92. Schlücker, S., *Surface-Enhanced Raman Spectroscopy: Concepts and Chemical Applications*. Angewandte Chemie International Edition, 2014. **53**(19): p. 4756-4795.
93. Stiles, P.L., et al., *Surface-Enhanced Raman Spectroscopy*. Annual Review of Analytical Chemistry, 2008. **1**(1): p. 601-626.
94. Camden, J.P., et al., *Probing the Structure of Single-Molecule Surface-Enhanced Raman Scattering Hot Spots*. Journal of the American Chemical Society, 2008. **130**(38): p. 12616-12617.
95. Jensen, L., C.M. Aikens, and G.C. Schatz, *Electronic structure methods for studying surface-enhanced Raman scattering*. Chemical Society Reviews, 2008. **37**(5): p. 1061-1073.
96. Morton, S.M. and L. Jensen, *Understanding The Molecule-Surface Chemical Coupling in SERS*. Journal of the American Chemical Society, 2009. **131**(11): p. 4090-4098.
97. Stewart, A., S. Murray, and S.E.J. Bell, *Simple preparation of positively charged silver nanoparticles for detection of anions by surface-enhanced Raman spectroscopy*. Analyst, 2015. **140**(9): p. 2988-2994.
98. Boltasseva, A. and H.A. Atwater, *Low-Loss Plasmonic Metamaterials*. Science, 2011. **331**(6015): p. 290-291.

99. Kosuda, K.M., et al., *4.06 - Nanostructures and Surface-Enhanced Raman Spectroscopy*☆, in *Comprehensive Nanoscience and Nanotechnology (Second Edition)*, D.L. Andrews, R.H. Lipson, and T. Nann, Editors. 2016, Academic Press: Oxford. p. 117-152.
100. Pei, Y., et al., *Highly sensitive SERS-based immunoassay with simultaneous utilization of self-assembled substrates of gold nanostars and aggregates of gold nanostars*. *Journal of Materials Chemistry B*, 2013. **1**(32): p. 3992-3998.
101. Lee, J., et al., *Tailoring surface plasmons of high-density gold nanostar assemblies on metal films for surface-enhanced Raman spectroscopy*. *Nanoscale*, 2014. **6**(1): p. 616-623.
102. Xie, J., et al., *The Synthesis of SERS-Active Gold Nanoflower Tags for In Vivo Applications*. *ACS Nano*, 2008. **2**(12): p. 2473-2480.
103. Yi, S., et al., *One-step synthesis of dendritic gold nanoflowers with high surface-enhanced Raman scattering (SERS) properties*. *RSC Advances*, 2013. **3**(26): p. 10139-10144.
104. von Maltzahn, G., et al., *SERS-Coded Gold Nanorods as a Multifunctional Platform for Densely Multiplexed Near-Infrared Imaging and Photothermal Heating*. *Advanced Materials*, 2009. **21**(31): p. 3175-3180.
105. Huang, X., et al., *Cancer Cells Assemble and Align Gold Nanorods Conjugated to Antibodies to Produce Highly Enhanced, Sharp, and Polarized Surface Raman Spectra: A Potential Cancer Diagnostic Marker*. *Nano Letters*, 2007. **7**(6): p. 1591-1597.
106. Scarabelli, L., et al., *Monodisperse Gold Nanotriangles: Size Control, Large-Scale Self-Assembly, and Performance in Surface-Enhanced Raman Scattering*. *ACS Nano*, 2014. **8**(6): p. 5833-5842.
107. Geng, X., et al., *Protein-aided formation of triangular silver nanoprisms with enhanced SERS performance*. *Journal of Materials Chemistry B*, 2016. **4**(23): p. 4182-4190.
108. Sherry, L.J., et al., *Localized Surface Plasmon Resonance Spectroscopy of Single Silver Nanocubes*. *Nano Letters*, 2005. **5**(10): p. 2034-2038.
109. Rycenga, M., et al., *Generation of Hot Spots with Silver Nanocubes for Single-Molecule Detection by Surface-Enhanced Raman Scattering*. *Angewandte Chemie International Edition*, 2011. **50**(24): p. 5473-5477.
110. Bich Quyen, T.T., et al., *Novel Ag/Au/Pt trimetallic nanocages used with surface-enhanced Raman scattering for trace fluorescent dye detection*. *Journal of Materials Chemistry B*, 2014. **2**(34): p. 5550-5557.
111. Rycenga, M., et al., *Probing the surface-enhanced Raman scattering properties of Au-Ag nanocages at two different excitation wavelengths*. *Physical Chemistry Chemical Physics*, 2009. **11**(28): p. 5903-5908.
112. Song, C.Y., et al., *Facile synthesis of hydrangea flower-like hierarchical gold nanostructures with tunable surface topographies for single-particle surface-enhanced Raman scattering*. *Nanoscale*, 2015. **7**(40): p. 17004-17011.
113. Wustholz, K.L., et al., *Structure-Activity Relationships in Gold Nanoparticle Dimers and Trimers for Surface-Enhanced Raman Spectroscopy*. *Journal of the*

- American Chemical Society, 2010. **132**(31): p. 10903-10910.
114. Lombardi, J.R. and R.L. Birke, *A Unified View of Surface-Enhanced Raman Scattering*. Accounts of Chemical Research, 2009. **42**(6): p. 734-742.
115. Wang, Y., et al., *Direct observation of surface-enhanced Raman scattering in ZnO nanocrystals*. Journal of Raman Spectroscopy, 2009. **40**(8): p. 1072-1077.
116. Ji, W., et al., *Enhanced Raman Scattering by ZnO Superstructures: Synergistic Effect of Charge Transfer and Mie Resonances*. Angewandte Chemie International Edition, 2019. **58**(41): p. 14452-14456.
117. Alessandri, I., *Enhancing Raman Scattering without Plasmons: Unprecedented Sensitivity Achieved by TiO<sub>2</sub> Shell-Based Resonators*. Journal of the American Chemical Society, 2013. **135**(15): p. 5541-5544.
118. Lin, J., et al., *Ultrasensitive SERS Detection by Defect Engineering on Single Cu<sub>2</sub>O Superstructure Particle*. Advanced Materials, 2017. **29**(5): p. 1604797.
119. Cong, S., et al., *Noble metal-comparable SERS enhancement from semiconducting metal oxides by making oxygen vacancies*. Nature Communications, 2015. **6**(1): p. 7800.
120. Li, A., et al., *Surface-Enhanced Raman Spectroscopy on Amorphous Semiconducting Rhodium Sulfide Microbowl Substrates*. iScience, 2018. **10**: p. 1-10.
121. Zhang, Q., et al., *A metallic molybdenum dioxide with high stability for surface enhanced Raman spectroscopy*. Nature Communications, 2017. **8**(1): p. 14903.
122. Jiang, L., et al., *Highly Reproducible Surface-Enhanced Raman Spectra on Semiconductor SnO<sub>2</sub> Octahedral Nanoparticles*. ChemPhysChem, 2012. **13**(17): p. 3932-3936.
123. Shan, Y., et al., *Niobium pentoxide: a promising surface-enhanced Raman scattering active semiconductor substrate*. npj Computational Materials, 2017. **3**(1): p. 11.
124. Yang, L., et al., *A Novel Ultra-Sensitive Semiconductor SERS Substrate Boosted by the Coupled Resonance Effect*. Advanced Science, 2019. **6**(12): p. 1900310.
125. Yang, L., et al., *Green and Sensitive Flexible Semiconductor SERS Substrates: Hydrogenated Black TiO<sub>2</sub> Nanowires*. ACS Applied Nano Materials, 2018. **1**(9): p. 4516-4527.
126. Lombardi, J.R. and R.L. Birke, *Theory of Surface-Enhanced Raman Scattering in Semiconductors*. The Journal of Physical Chemistry C, 2014. **118**(20): p. 11120-11130.
127. Alessandri, I. and J.R. Lombardi, *Enhanced Raman Scattering with Dielectrics*. Chemical Reviews, 2016. **116**(24): p. 14921-14981.
128. Han, X.X., et al., *Semiconductor-enhanced Raman scattering: active nanomaterials and applications*. Nanoscale, 2017. **9**(15): p. 4847-4861.
129. Wang, X., et al., *Remarkable SERS Activity Observed from Amorphous ZnO Nanocages*. Angewandte Chemie International Edition, 2017. **56**(33): p. 9851-9855.
130. Wang, X., et al., *Two-Dimensional Amorphous TiO<sub>2</sub> Nanosheets Enabling High-Efficiency Photoinduced Charge Transfer for Excellent SERS Activity*. Journal of

- the American Chemical Society, 2019. **141**(14): p. 5856-5862.
131. Lin, J., et al., *Crystal-Amorphous Core-Shell Structure Synergistically Enabling TiO<sub>2</sub> Nanoparticles' Remarkable SERS Sensitivity for Cancer Cell Imaging*. ACS Applied Materials & Interfaces, 2020. **12**(4): p. 4204-4211.
  132. Gao, Y., et al., *Semiconductor SERS of diamond*. Nanoscale, 2018. **10**(33): p. 15788-15792.
  133. Liu, Q., L. Jiang, and L. Guo, *Precursor-Directed Self-Assembly of Porous ZnO Nanosheets as High-Performance Surface-Enhanced Raman Scattering Substrate*. Small, 2014. **10**(1): p. 48-51.
  134. Christie, D., J. Lombardi, and I. Kretzschmar, *Two-Dimensional Array of Silica Particles as a SERS Substrate*. The Journal of Physical Chemistry C, 2014. **118**(17): p. 9114-9118.
  135. Fu, X., et al., *Charge-transfer contributions in surface-enhanced Raman scattering from Ag, Ag<sub>2</sub>S and Ag<sub>2</sub>Se substrates*. Journal of Raman Spectroscopy, 2012. **43**(9): p. 1191-1195.
  136. Zhang, X., et al., *Rapid Detection of an Anthrax Biomarker by Surface-Enhanced Raman Spectroscopy*. Journal of the American Chemical Society, 2005. **127**(12): p. 4484-4489.
  137. Zhang, X., et al., *Ultrastable Substrates for Surface-Enhanced Raman Spectroscopy: Al<sub>2</sub>O<sub>3</sub> Overlayers Fabricated by Atomic Layer Deposition Yield Improved Anthrax Biomarker Detection*. Journal of the American Chemical Society, 2006. **128**(31): p. 10304-10309.
  138. Huang, G.G., et al., *Development of a Heat-Induced Surface-Enhanced Raman Scattering Sensing Method for Rapid Detection of Glutathione in Aqueous Solutions*. Analytical Chemistry, 2009. **81**(14): p. 5881-5888.
  139. Deckert-Gaudig, T., E. Bailo, and V. Deckert, *Tip-enhanced Raman scattering (TERS) of oxidised glutathione on an ultraflat gold nanoplate*. Physical Chemistry Chemical Physics, 2009. **11**(34): p. 7360-7362.
  140. Vitol, E.A., et al., *Surface-Enhanced Raman Spectroscopy as a Tool for Detecting Ca<sup>2+</sup> Mobilizing Second Messengers in Cell Extracts*. Analytical Chemistry, 2010. **82**(16): p. 6770-6774.
  141. Shafer-Peltier, K.E., et al., *Toward a Glucose Biosensor Based on Surface-Enhanced Raman Scattering*. Journal of the American Chemical Society, 2003. **125**(2): p. 588-593.
  142. Shaj, N.C., et al., *Lactate and Sequential Lactate-Glucose Sensing Using Surface-Enhanced Raman Spectroscopy*. Analytical Chemistry, 2007. **79**(18): p. 6927-6932.
  143. Fox, C.B., R.H. Uibel, and J.M. Harris, *Detecting Phase Transitions in Phosphatidylcholine Vesicles by Raman Microscopy and Self-Modeling Curve Resolution*. The Journal of Physical Chemistry B, 2007. **111**(39): p. 11428-11436.
  144. Pal, A., et al., *Synthesis and characterization of SERS gene probe for BRCA-1 (breast cancer)*. Faraday Discussions, 2006. **132**(0): p. 293-301.
  145. Braun, G., et al., *Surface-Enhanced Raman Spectroscopy for DNA Detection by Nanoparticle Assembly onto Smooth Metal Films*. Journal of the American

- Chemical Society, 2007. **129**(20): p. 6378-6379.
146. Bonham, A.J., et al., *Detection of Sequence-Specific Protein-DNA Interactions via Surface Enhanced Resonance Raman Scattering*. Journal of the American Chemical Society, 2007. **129**(47): p. 14572-14573.
147. Doering, W.E., et al., *SERS as a Foundation for Nanoscale, Optically Detected Biological Labels*. Advanced Materials, 2007. **19**(20): p. 3100-3108.
148. Barhoumi, A., et al., *Surface-Enhanced Raman Spectroscopy of DNA*. Journal of the American Chemical Society, 2008. **130**(16): p. 5523-5529.
149. Han, X.X., B. Zhao, and Y. Ozaki, *Surface-enhanced Raman scattering for protein detection*. Analytical and Bioanalytical Chemistry, 2009. **394**(7): p. 1719-1727.
150. Wei, F., et al., *Aromatic Amino Acids Providing Characteristic Motifs in the Raman and SERS Spectroscopy of Peptides*. The Journal of Physical Chemistry B, 2008. **112**(30): p. 9158-9164.
151. Han, X.X., et al., *Highly Sensitive Protein Concentration Assay over a Wide Range via Surface-Enhanced Raman Scattering of Coomassie Brilliant Blue*. Analytical Chemistry, 2010. **82**(11): p. 4325-4328.
152. Stuart, D.A., et al., *In Vivo Glucose Measurement by Surface-Enhanced Raman Spectroscopy*. Analytical Chemistry, 2006. **78**(20): p. 7211-7215.
153. Qian, X., et al., *In vivo tumor targeting and spectroscopic detection with surface-enhanced Raman nanoparticle tags*. Nature Biotechnology, 2008. **26**(1): p. 83-90.
154. Caruso, F., *Nanoengineering of Particle Surfaces*. Advanced Materials, 2001. **13**(1): p. 11-22.
155. Li, X., et al., *Electromagnetic Functionalized And Core-Shell Micro/Nanostructured Polypyrrole Composites*. The Journal of Physical Chemistry B, 2006. **110**(30): p. 14623-14626.
156. Girotti, M.R., et al., *836 - Application of sequencing, liquid biopsies and patient-derived xenografts for personalized medicine in melanoma*. European Journal of Cancer, 2016. **61**: p. S193.
157. Allard, W.J., et al., *Tumor cells circulate in the peripheral blood of all major carcinomas but not in healthy subjects or patients with non-malignant diseases*. Journal of Clinical Oncology, 2004. **22**(14): p. 847S-847S.
158. Kim, J., et al., *Generalized Fabrication of Multifunctional Nanoparticle Assemblies on Silica Spheres*. Angewandte Chemie International Edition, 2006. **45**(29): p. 4789-4793.
159. Sacanna, S. and A.P. Philipse, *Preparation and Properties of Monodisperse Latex Spheres with Controlled Magnetic Moment for Field-Induced Colloidal Crystallization and (Dipolar) Chain Formation*. Langmuir, 2006. **22**(24): p. 10209-10216.
160. Nagao, D., et al., *Synthesis of Highly Monodisperse Particles Composed of a Magnetic Core and Fluorescent Shell*. Langmuir, 2008. **24**(17): p. 9804-9808.
161. Ge, J., et al., *Magnetically induced colloidal assembly into field-responsive photonic structures*. Nanoscale, 2011. **3**(1): p. 177-183.
162. Ge, J., et al., *Magnetochromatic Microspheres: Rotating Photonic Crystals*. Journal of the American Chemical Society, 2009. **131**(43): p. 15687-15694.

163. Lee, G., J. Kim, and J.-h. Lee, *Development of magnetically separable polyaniline nanofibers for enzyme immobilization and recovery*. Enzyme and Microbial Technology, 2008. **42**(6): p. 466-472.
164. Yavuz, M.S., et al., *Gold nanocages covered by smart polymers for controlled release with near-infrared light*. Nature Materials, 2009. **8**(12): p. 935-939.
165. Skrabalak, S.E., et al., *Gold Nanocages for Biomedical Applications*. Advanced Materials, 2007. **19**(20): p. 3177-3184.
166. Hirsch, L.R., et al., *Nanoshell-mediated near-infrared thermal therapy of tumors under magnetic resonance guidance*. Proceedings of the National Academy of Sciences, 2003. **100**(23): p. 13549-13554.
167. Adler, D.C., et al., *Photothermal detection of gold nanoparticles using phase-sensitive optical coherence tomography*. Optics Express, 2008. **16**(7): p. 4376-4393.
168. Ming, T., et al., *Growth of Tetrahedral Gold Nanocrystals with High-Index Facets*. Journal of the American Chemical Society, 2009. **131**(45): p. 16350-16351.
169. Song, H.-M., et al., *Plasmon-Resonant Nanoparticles and Nanostars with Magnetic Cores: Synthesis and Magnetomotive Imaging*. ACS Nano, 2010. **4**(9): p. 5163-5173.
170. Kim, J., et al., *Designed Fabrication of Multifunctional Magnetic Gold Nanoshells and Their Application to Magnetic Resonance Imaging and Photothermal Therapy*. Angewandte Chemie International Edition, 2006. **45**(46): p. 7754-7758.
171. Lim, Y.T., et al., *Plasmonic Magnetic Nanostructure for Bimodal Imaging and Photonic-Based Therapy of Cancer Cells*. ChemBioChem, 2007. **8**(18): p. 2204-2209.
172. García, I., et al., *Magnetic Glyconanoparticles as a Versatile Platform for Selective Immunolabeling and Imaging of Cells*. Bioconjugate Chemistry, 2011. **22**(2): p. 264-273.
173. Kirui, D.K., D.A. Rey, and C.A. Batt, *Gold hybrid nanoparticles for targeted phototherapy and cancer imaging*. Nanotechnology, 2010. **21**(10): p. 105105.
174. Bardhan, R., et al., *Nanoshells with Targeted Simultaneous Enhancement of Magnetic and Optical Imaging and Photothermal Therapeutic Response*. Advanced Functional Materials, 2009. **19**(24): p. 3901-3909.
175. Leung, K.C.-F., et al., *Gold and iron oxide hybrid nanocomposite materials*. Chemical Society Reviews, 2012. **41**(5): p. 1911-1928.
176. Goon, I.Y., et al., *Fabrication and Dispersion of Gold-Shell-Protected Magnetite Nanoparticles: Systematic Control Using Polyethyleneimine*. Chemistry of Materials, 2009. **21**(4): p. 673-681.
177. Janib, S.M., A.S. Moses, and J.A. MacKay, *Imaging and drug delivery using theranostic nanoparticles*. Advanced Drug Delivery Reviews, 2010. **62**(11): p. 1052-1063.
178. Kim, D., et al., *Antibiofouling Polymer-Coated Gold Nanoparticles as a Contrast Agent for in Vivo X-ray Computed Tomography Imaging*. Journal of the American Chemical Society, 2007. **129**(24): p. 7661-7665.
179. Xu, C., B. Wang, and S. Sun, *Dumbbell-like Au-Fe<sub>3</sub>O<sub>4</sub> Nanoparticles for Target-*

- Specific Platin Delivery*. Journal of the American Chemical Society, 2009. **131**(12): p. 4216-4217.
180. Bardhan, R., et al., *Fluorescence Enhancement by Au Nanostructures: Nanoshells and Nanorods*. ACS Nano, 2009. **3**(3): p. 744-752.
181. Kim, D.H., et al., *Synthesis of Hybrid Gold/Iron Oxide Nanoparticles in Block Copolymer Micelles for Imaging, Drug Delivery, and Magnetic Hyperthermia*. IEEE Transactions on Magnetics, 2009. **45**(10): p. 4821-4824.
182. Minelli, C., S.B. Lowe, and M.M. Stevens, *Engineering Nanocomposite Materials for Cancer Therapy*. Small, 2010. **6**(21): p. 2336-2357.
183. Thaxton, C.S., D.G. Georganopoulou, and C.A. Mirkin, *Gold nanoparticle probes for the detection of nucleic acid targets*. Clinica Chimica Acta, 2006. **363**(1): p. 120-126.
184. Williams, T.I., et al., *Epithelial Ovarian Cancer: Disease Etiology, Treatment, Detection, and Investigational Gene, Metabolite, and Protein Biomarkers*. Journal of Proteome Research, 2007. **6**(8): p. 2936-2962.
185. Mani, V., et al., *Ultrasensitive Immunosensor for Cancer Biomarker Proteins Using Gold Nanoparticle Film Electrodes and Multienzyme-Particle Amplification*. ACS Nano, 2009. **3**(3): p. 585-594.
186. Qiu, J.-D., et al., *Facile preparation of magnetic core-shell Fe<sub>3</sub>O<sub>4</sub>@Au nanoparticle/myoglobin biofilm for direct electrochemistry*. Biosensors and Bioelectronics, 2010. **25**(6): p. 1447-1453.
187. Wang, C. and J. Irudayaraj, *Multifunctional Magnetic-Optical Nanoparticle Probes for Simultaneous Detection, Separation, and Thermal Ablation of Multiple Pathogens*. Small, 2010. **6**(2): p. 283-289.
188. Hashmi, A.S.K. and G.J. Hutchings, *Gold Catalysis*. Angewandte Chemie International Edition, 2006. **45**(47): p. 7896-7936.
189. Arcadi, A., *Alternative Synthetic Methods through New Developments in Catalysis by Gold*. Chemical Reviews, 2008. **108**(8): p. 3266-3325.
190. Corma, A. and H. Garcia, *Supported gold nanoparticles as catalysts for organic reactions*. Chemical Society Reviews, 2008. **37**(9): p. 2096-2126.
191. Nash, M.A., et al., *Mixed Stimuli-Responsive Magnetic and Gold Nanoparticle System for Rapid Purification, Enrichment, and Detection of Biomarkers*. Bioconjugate Chemistry, 2010. **21**(12): p. 2197-2204.
192. Liu, H.L., et al., *Synthesis of streptavidin-FITC-conjugated core-shell Fe<sub>3</sub>O<sub>4</sub>-Au nanocrystals and their application for the purification of CD4<sup>+</sup> lymphocytes*. Biomaterials, 2008. **29**(29): p. 4003-4011.
193. Yu, C.-J., et al., *Synthesis of poly(diallyldimethylammonium chloride)-coated Fe<sub>3</sub>O<sub>4</sub> nanoparticles for colorimetric sensing of glucose and selective extraction of thiol*. Biosensors and Bioelectronics, 2010. **26**(2): p. 913-917.
194. Lyu, Z., et al., *Synergy of palladium species and hydrogenation for enhanced photocatalytic activity of {001} facets dominant TiO<sub>2</sub> nanosheets*. Journal of Materials Research, 2017. **32**(14): p. 2781-2789.
195. Song, Y., J. Li, and C. Wang, *Modification of porphyrin/dipyridine metal complexes on the surface of TiO<sub>2</sub> nanotubes with enhanced photocatalytic*

- activity for photoreduction of CO<sub>2</sub> into methanol*. Journal of Materials Research, 2018. **33**(17): p. 2612-2620.
196. Chen, X., et al., *Increasing Solar Absorption for Photocatalysis with Black Hydrogenated Titanium Dioxide Nanocrystals*. Science, 2011. **331**(6018): p. 746-750.
197. Ren, W., et al., *A Near Infrared Light Triggered Hydrogenated Black TiO<sub>2</sub> for Cancer Photothermal Therapy*. Advanced Healthcare Materials, 2015. **4**(10): p. 1526-1536.
198. Ren, W., et al., *Black TiO<sub>2</sub> based core-shell nanocomposites as doxorubicin carriers for thermal imaging guided synergistic therapy of breast cancer*. Nanoscale, 2017. **9**(31): p. 11195-11204.
199. Xue, T., et al., *Detection of circulating tumor cells based on improved SERS-active magnetic nanoparticles*. Analytical Methods, 2019. **11**(22): p. 2918-2928.
200. Tan, H.Q., et al., *A facile and versatile method for preparation of colored TiO<sub>2</sub> with enhanced solar-driven photocatalytic activity*. Nanoscale, 2014. **6**(17): p. 10216-10223.
201. Rajh, T., et al., *Surface Restructuring of Nanoparticles: An Efficient for Ligand-Metal Oxide Crosstalk*. The Journal of Physical Chemistry B, 2002. **106**(41): p. 10543-10552.
202. Ma, X.-H., et al., *Biocompatible composite nanoparticles with large longitudinal relaxivity for targeted imaging and early diagnosis of cancer*. Journal of Materials Chemistry B, 2013. **1**(27): p. 3419-3428.
203. Khismatullin, D.B. and G.A. Truskey, *Leukocyte Rolling on P-Selectin: A Three-Dimensional Numerical Study of the Effect of Cytoplasmic Viscosity*. Biophysical Journal, 2012. **102**(8): p. 1757-1766.
204. Webb, J.A. and R. Bardhan, *Emerging advances in nanomedicine with engineered gold nanostructures*. Nanoscale, 2014. **6**(5): p. 2502-2530.
205. Adams, A.A., et al., *Highly efficient circulating tumor cell isolation from whole blood and label-free enumeration using polymer-based microfluidics with an integrated conductivity sensor*. Journal of the American Chemical Society, 2008. **130**(27): p. 8633-8641.
206. Haldavnekar, R., K. Venkatakrishnan, and B. Tan, *Non plasmonic semiconductor quantum SERS probe as a pathway for in vitro cancer detection*. Nature Communications, 2018. **9**.
207. Qi, D.Y., et al., *Improved SERS Sensitivity on Plasmon-Free TiO<sub>2</sub> Photonic Microarray by Enhancing Light-Matter Coupling*. Journal of the American Chemical Society, 2014. **136**(28): p. 9886-9889.
208. Xu, X.W., et al., *Microfluidic applications on circulating tumor cell isolation and biomimicking of cancer metastasis*. Electrophoresis, 2020. **41**(10-11): p. 933-951.
209. Zhang, X.Z., et al., *Public-Health-Driven Microfluidic Technologies: From Separation to Detection*. Micromachines, 2021. **12**(4).
210. Zhang, X.Z., et al., *Numerical simulation of circulating tumor cell separation in a dielectrophoresis based Y-Y shaped microfluidic device*. Separation and Purification Technology, 2021. **255**: p 117343.

211. Alunni-Fabbroni, M. and M.T. Sandri, *Circulating tumour cells in clinical practice: Methods of detection and possible characterization*. *Methods*, 2010. **50**(4): p. 289-297.
212. Hao, S.J., et al., *Size-based separation methods of circulating tumor cells*. *Advanced Drug Delivery Reviews*, 2018. **125**: p. 3-20.
213. Lane, L.A., X.M. Qian, and S.M. Nie, *SERS Nanoparticles in Medicine: From Label-Free Detection to Spectroscopic Tagging*. *Chemical Reviews*, 2015. **115**(19): p. 10489-10529.
214. Sahoo, H., *Fluorescent labeling techniques in biomolecules: a flashback*. *Rsc Advances*, 2012. **2**(18): p. 7017-7029.
215. Song, Y.L., et al., *Bioinspired Engineering of a Multivalent Aptamer-Functionalized Nanointerface to Enhance the Capture and Release of Circulating Tumor Cells*. *Angewandte Chemie-International Edition*, 2019. **58**(8): p. 2236-2240.
216. Wang, C., et al., *Simultaneous isolation and detection of circulating tumor cells with a microfluidic silicon-nanowire-array integrated with magnetic upconversion nanoprobes*. *Biomaterials*, 2015. **54**: p. 55-62.
217. Tang, M., et al., *A chip assisted immunomagnetic separation system for the efficient capture and in situ identification of circulating tumor cells*. *Lab on a Chip*, 2016. **16**(7): p. 1214-1223.
218. Earhart, C.M., et al., *Isolation and mutational analysis of circulating tumor cells from lung cancer patients with magnetic sifters and biochips*. *Lab on a Chip*, 2014. **14**(1): p. 78-88.
219. Yan, S.Q., et al., *Rhizalis (Cactaceae)-like Hierarchical Structure Based Microfluidic Chip for Highly Efficient Isolation of Rare Cancer Cells*. *ACS Applied Materials & Interfaces*, 2016. **8**(49): p. 33457-33463.
220. Che, J., et al., *Classification of large circulating tumor cells isolated with ultra-high throughput microfluidic Vortex technology*. *Oncotarget*, 2016. **7**(11): p. 12748-12760.
221. Warkiani, M.E., et al., *An ultra-high-throughput spiral microfluidic biochip for the enrichment of circulating tumor cells*. *Analyst*, 2014. **139**(13): p. 3245-3255.
222. Khoo, B.L., et al., *Clinical Validation of an Ultra High-Throughput Spiral Microfluidics for the Detection and Enrichment of Viable Circulating Tumor Cells*. *Plos One*, 2014. **9**(7): p. 7.
223. Wang, J.D., et al., *Label-Free Isolation and mRNA Detection of Circulating Tumor Cells from Patients with Metastatic Lung Cancer for Disease Diagnosis and Monitoring Therapeutic Efficacy*. *Analytical Chemistry*, 2015. **87**(23): p. 11893-11900.
224. Kim, T.H., et al., *FAST: Size-Selective, Clog-Free Isolation of Rare Cancer Cells from Whole Blood at a Liquid-Liquid Interface*. *Analytical Chemistry*, 2017. **89**(2): p. 1155-1162.
225. Gao, W.L., et al., *Analysis of circulating tumor cells from lung cancer patients with multiple biomarkers using high-performance size-based microfluidic chip*. *Oncotarget*, 2017. **8**(8): p. 12917-12928.

226. Che, J., et al., *Biophysical isolation and identification of circulating tumor cells*. Lab on a Chip, 2017. **17**(8): p. 1452-1461.
227. Qian, C., et al., *Clinical significance of circulating tumor cells from lung cancer patients using microfluidic chip*. Clinical and Experimental Medicine, 2018. **18**(2): p. 191-202.
228. Dhar, M., et al., *Evaluation of PD-L1 expression on vortex-isolated circulating tumor cells in metastatic lung cancer*. Scientific Reports, 2018. **8**: p. 10.
229. Ozkumur, E., et al., *Inertial Focusing for Tumor Antigen-Dependent and -Independent Sorting of Rare Circulating Tumor Cells*. Science Translational Medicine, 2013. **5**(179): p. 11.
230. Liu, et al., *High throughput capture of circulating tumor cells using an integrated microfluidic system*. Biosensors and Bioelectronics, 2013. **47**: p 113-119.
231. Fachin, F., et al., *Monolithic Chip for High-throughput Blood Cell Depletion to Sort Rare Circulating Tumor Cells*. Scientific Reports, 2017. **7**: p. 11.
232. Lin, B.K., et al., *Highly selective biomechanical separation of cancer cells from leukocytes using microfluidic ratchets and hydrodynamic concentrator*. Biomicrofluidics, 2013. **7**(3): p. 11.
233. Zhao, M.X., et al., *New Generation of Ensemble-Decision Aliquot Ranking Based on Simplified Microfluidic Components for Large-Capacity Trapping of Circulating Tumor Cells*. Analytical Chemistry, 2013. **85**(20): p. 9671-9677.

## Appendix

Table 1: Performance of label-dependent microfluidic methods for CTC isolation

| Cancer type                               | Methods                | Isolation marker | Cancer cell lines | Cancer cell lines                         |                    |            |             | CTCs              |                              |                    | Ref.  |
|---|------------------------|------------------|-------------------|---|--------------------|------------|-------------|-------------------|------------------------------|--------------------|-------|
|   |                        |                  |                   | Recovery                                  | Capture efficiency | Throughput | Viability   | Number of samples | Sensitivity CTCs/ml          | Capture efficiency |       |
| Colorectal cancer; prostatic carcinoma    | Immunocapture          | EpCAM            | PC3               | 74.2-84.4%                                | -                  | 1 ml/h     | 96%         | 13 CRC, 25 PCa    | CRC: 7.2±3.4<br>PCa: 8.3±5.0 | -                  | [215] |
| Lung cancer                               | Immunocapture          | EpCAM            | A549              | ~90%                                      | -                  | 1ml/h      | Up to 93%   | 21                | -                            | -                  | [216] |
| Breast cancer                             | Immunomagnetic capture | EpCAM            | MCF-7             | 95.8%                                     | -                  |            | 93.1 ± 2.6% | 10                | -                            | 94%                | [217] |
| Lung cancer                               | Immunomagnetic capture | EpCAM            | H-1650            | 95.7%                                     | -                  | 5-25ml/h   | -           | 5                 | 31–96 CTCs/ml                | -                  | [218] |
| Breast cancer; non-small-cell lung cancer | Immunocapture          | EpCAM            | MCF-7, NCI-H1650  | 76.5%, 82.7%, 83.7%<br>In 1ml whole blood | 88%                | -          | -           | -                 | -                            | -                  | [219] |
| Breast cancer                             | Hydrogel-based capture | EpCAM            | MCF-7             | 95 ± 4%                                   | 92 ± 6%            | 1ml/h      | 95%         | 13                | 3-12 CTCs /ml                | -                  | [63]  |
| Cervical carcinoma                        | Hydrogel-based capture | Folic Acid       | Hela              | -   | -                  | -          | -           | -                 | -                            | 85%                | [64]  |
| Breast cancer                             | Immunofluorescence     | EpCAM            | Her2              | 94%                                       | -                  | 1ml/30min  | -           | 82                | 90 CTCs /7.5ml               | -                  | [70]  |

Table 2: Performance of label-independent microfluidic methods for CTC isolation

| Cancer type                      | Methods   | Cancer cell lines                         | Cancer cell lines        |         |             |              | CTCs                               |  |                    | Ref.  |
|----------------------------------|-----------|---|--------------------------|---------|-------------|--------------|------------------------------------|--|--------------------|-------|
|                                  |           |   | Recovery                 | Purity  | Throughout  | Viability    | Number of samples                  | Sensitivity (CTCs/ml)  | Purity             |       |
| Lung cancer, Breast cancer       | Vortex    | MCF-7                                     | 84%                      | 80%     | 8 ml/min    | 83.9% ± 4.0% | 22 breast cancer<br>15 lung cancer | Lung cancer 0.5-24.2<br>Breast cancer 0.75-23.25 CTCs/ml   | -                  | [220] |
| Lung cancer, Breast cancer       | DFF       | MCF-7, T24                                | MCF-7: 87.6%<br>T2476.4% | -       | 350 µL/min  | -            | 5 breast cancer<br>5 lung cancer   | 20-135 CTCs/ml   | 1CTC/30-100WBCs    | [221] |
| Lung cancer                      | DFF       | MCF-7<br>NSCLC 1650                       | -                        | -       | 7.5 ml/5min | -            | 58                                 | Lung cancer 82 CTCs/ml<br>Breast cancer 55 CTCs/ml   | -                  | [222] |
| Lung cancer                      | DFF       | A549                                      | 74.4% capture efficiency | -       | 25 mL/h     | -            | 34                                 |  | 90 %detection rate | [223] |
| Breast, stomach, and lung cancer | FAST      | MCF-7, MDA-MB-231, MDA-MB-436, HCC78, AGS | 95.9 ±3.1%               | -       | >3 mL/min   | -            | 142                                | Breast cancer<br>0–540 CTCs/7.5 mL<br>stomach cancer<br>2–485 CTCs/7.5 mL<br>lung cancer<br>0–62 CTCs/7.5 mL | -                  | [224] |
| Lung cancer                      | Filtering | H446, A549, SK-MES-1                      | 90%                      | -       | 15mL/h      | -            | 45                                 | 1.85-68.45 CTCs/mL   | -                  | [225] |
| Lung cancer                      | Vortex    | MCF7                                      | 56%                      | 35.1% ± | -           | -            | 16                                 |  | -                  | [226] |

|             |                   |                          |     |      |   |   |     |  |                                |       |
|-------------|-------------------|--------------------------|-----|------|---|---|-----|--|--------------------------------|-------|
|             |                   |                          |     | 7.3% |   |   |     |  |                                |       |
| Lung cancer | DLD,<br>filtering | Lung cancer cell<br>line | 86% |      | - | - | 200 | I stage<br>5.0 ± 5.121CTCs/mL<br>II stage<br>8.731 ± 6.36CTCs/mL<br>III stage<br>16.81 ± 9.556 CTCs/mL | -                              | [227] |
| Lung cancer | Vortex            | A549, H1703,<br>H3255    | -   | -    | - | - | 22  | 1.32 CTCs/mL   | 48.4% -96.8%<br>detection rate | [228] |

Table 3: Performance of multi-step methods for CTC isolation

| Cancer type                             | Method                         | Isolation marker      | Cancer cell lines  | Cancer cell lines  |        |                              | CTCs                                |  |   | Ref.  |
|---|--------------------------------|-----------------------|--|--------------------|--------|------------------------------|-------------------------------------|--|---|-------|
|   |                                |                       |  | Recovery           | Purity | Throughout                   | Number of samples                   | Sensitivity CTCs/ml                          | Purity  |       |
| Lung, breast, prostate cancer           | DLD and Immunocapture          | EpCAM                 | MCF-7<br>PC3-9   | 90%<br>89.7 ± 4.5% | -      | 576 ml/h                     | 41 prostate patients                | ≥0.5 CTC/m                                   | >3.5-log purification 1500 WBCs/ml of whole blood | [229] |
| Breast cancer                           | DLD and Immunomagnetic capture | EpCAM                 | MCF-7  | 90%                | >40%   | 9.6 mL/min                   | -                                   | -  | -   | [230] |
| Breast, prostate, lung, melanoma cancer | DLD and Immunomagnetic capture | CD16<br>CD45<br>CD66b | H1975, H3122,<br>LNCAP,<br>PC3, PC3-9, VCAP,<br>MB231, MCF-7,<br>SKBR3 | -                  | -      | 15 × 10 <sup>6</sup> cells/s | 38 breast, prostate, lung, melanoma | 84.0%<br>96.4%<br>68.5%<br>63.6% of patients | -   | [231] |
| Bladder cancer                          | PFF and Crossflow              | -                     | UC13   | ~98%               | 89%    | 10 <sup>4</sup> cells /h     | -                                   | -  | -   | [232] |
| Breast cancer                           | Hydrodynamic and Microsieve    | EpCAM                 | MCF-7  | 95%                | -      | 1ml/12.5min                  | 26 pancreatic patients              | 80% of patients                              | -   | [233] |

